Stockholm University

# Master Thesis

Degree Project
in Marine Geology 60 hp

# Arctic Ocean seafloor surface geology based on interpretation of acoustic facies inferred from sub-bottom profiles acquired with icebreaker *Oden*

Vicent Doñate Felip

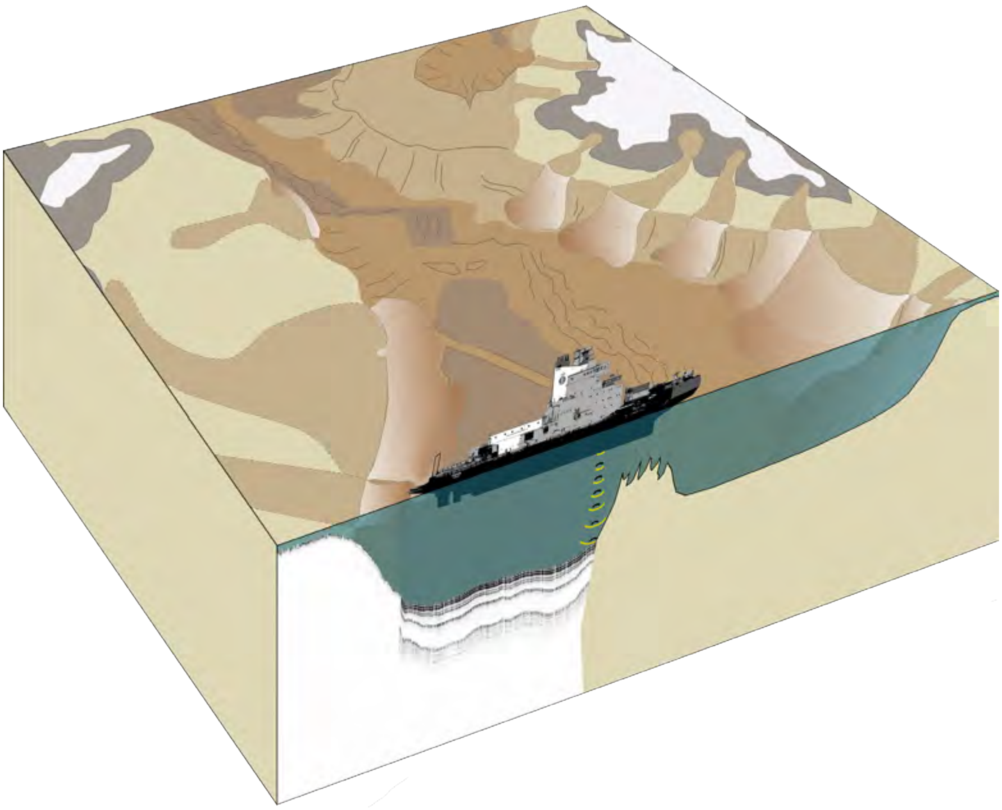

Stockholm 2024

Department of Geological Sciences
Stockholm University
SE-106 91 Stockholm
Sweden

This page is intentionally left blank.

# Abstract

The Arctic Ocean, its connection to the Atlantic Ocean, and the surrounding land and cryosphere play critical roles in regulating the global climate system. This region has undergone an exponential increase in research during the last few decades, leading to the release of four versions of the IBCAO bathymetric grid since then. Nevertheless, the compilation of the seafloor geology and uppermost sediment layers only began in 2015 under the "IBCAO Geology" project led by the Geological Survey of Canada, starting with the creation of a surficial geology map of the Amerasia Basin of the Arctic Ocean. As an expansion of this effort, a surficial geology map of the Eurasia Basin and its connection to the Atlantic was produced in this study. The compilation is based on the interpretation of acoustic facies inferred from sub-bottom profiles acquired with icebreakers, using both systematically collected data and transit data that often go unnoticed. Additional interpretations were made with the support of the IBCAO bathymetric grid in order to explain the processes that shape and shaped the seafloor and sub-bottom. Integrating the IBCAO Geology and IBCAO bathymetric grid thus provides a comprehensive understanding of the Arctic Ocean seafloor and its uppermost sediment layers, serving as a foundation for future research and survey planning.

Keywords: surficial geology map, Arctic Ocean, sub-bottom profiler, sediment dynamics, submarine landforms

## Acknowledgements

This thesis is not only a result of my work, so in this section, I would like to thank all the people who made it possible. First of all, to my supervisors, Martin Jakobsson and Christian Stranne: thank you for all your patience, guidance, support, and feedback during this journey, I really enjoyed it. Secondly, to the people from the Department of Geological Sciences, you make this place feel like home even though I am away from home. Especially to the Geologklubben, it was good fun sharing this time with you. Robert, sharing the apartment with me during this process also means sharing joy and sorrow, thank you for that. I would also like to mention the Baltic Sea Centre's research school, which brought lovely people into my life. Lastly, I virtually travel home to thank my family and friends. Paradoxically, my family made it possible for me to be where I am, even if they are sad each time they see me moving away. I could not be more grateful for your unconditional love and support. And to my friends there, thank you for your time, moments with you make me forget all the problems.

# Contents

# List of Figures

# Abbreviations

| | |
|---|---|
| **AO** | Arctic Ocean |
| **AP** | Arlis Plateau |
| **BAP** | Boreas Abyssal Plain |
| **BB** | Belgica Bank |
| **BITMF** | Bear Island Trough-Mouth Fan |
| **CAP** | Chukchi Abyssal Plain |
| **CB** | Chukchi Borderland |
| **CCGS** | Canadian Coast Guard Ship |
| **CHS** | Canadian Hydrographic Service |
| **CP** | Chukchi Plateau |
| **DBM** | Digital bathymetric model |
| **Df** | Debris flow |
| **EGC** | East Greenland Current |
| **EGR** | East Greenland Ridge |
| **EI** | Ellesmere Island |
| **ENE** | East-northeast |
| **FM** | Frequency-modulated |
| **FS** | Fram Strait |
| **GAP** | Greenland Abyssal Plain |
| **GDF** | Glacigenic debris flow |
| **GEBCO** | General Bathymetric Chart of the Oceans |
| **GR** | Greenland |
| **GSS** | Grenland-Spitsbergen Sill |
| **GZW** | Grounding zone wedge |
| **HALIP** | High Arctic large igneous province |
| **HL** | Hinlopen landslide |
| **HR** | Hovgaard Ridge |
| **IBCAO** | International Bathymetric Chart of the Arctic Ocean |
| **IB** | Icebreaker |
| **IHO** | International Hydrographic Organization |
| **IRD** | Ice-rafted debris |
| **KT** | Kveithola Trough |
| **LIA** | Little Ice Age |
| **LR** | Lomonosov ridge |
| **LT** | Litke Trough |
| **MAP** | Mendeleev Abyssal Plain |
| **MCR** | Mackenzie Continental Rise |
| **MD** | Mackenzie Delta |
| **MFZ** | Molloy Fracture Zone |
| **MH** | Molloy Hole |
| **MIS** | Marine Isotope Stage |
| **MJS** | Morris Jesup Spur |
| **MR** | Molloy Ridge |
| **MSGL** | Mega-scale glacial lineations |
| **MS** | Mosby Seamount |
| **MTD** | Mass Transport Deposit |
| **NAC** | Norwegian Atlantic Current |
| **NAP** | Northwind Abyssal Plain |
| **NBH** | NE basement high |
| **NCC** | Norwegian Coastal Current |
| **NE** | Northeast |
| **NNE** | North-northeast |
| **NNW** | North-northwest |
| **NR** | Northwind Ridge |
| **NT** | Norske Trough |
| **NW** | Northwest |
| **PAP** | Pole Abyssal Plain |
| **PS** | Polarstern Seamount |
| **RV** | Research Vessel |
| **SAP** | Siberia Abyssal Plain |
| **SAT** | St. Anna Trough |
| **SBH** | SE basement high |
| **SBP** | Sub-bottom profiler |
| **SB** | Sophia Basin |
| **SE** | Southeast |
| **SFZ** | Spitsbergen Fracture Zone |
| **SKT** | Store Koldeway Trough |
| **SRC** | Southern Ridge Crest |
| **SSE** | South-southeast |
| **SSW** | South-southwest |
| **STMF** | Storfjorden Trough-Mouth Fan |
| **SvB** | Sverdrup Bank |
| **SV** | Svalbard |
| **SW** | Southwest |
| **SZ** | Severnaya Zemlaya |
| **TWT** | Two-way travel time |
| **UNCLOS** | United Nations Convention on the Law of the Sea |
| **USCGC** | United States Coast Guard Cutter |
| **VR** | Vestnessa Ridge |
| **VT** | Voronov Terrace |
| **WAP** | Wrangel Abyssal Plain |
| **WBH** | W basement high |
| **WI** | Wrangel Island |
| **WSC** | West Spitsbergen Current |
| **WSW** | West-southwest |
| **YP** | Yermak Plateau |

# 1 Introduction

The region where the geographic and magnetic north poles are located is well known as the Arctic. Here, in the most septentrional part of the Earth, the Arctic Ocean (AO), is located as a continuation of the North Atlantic. The AO basin is known to contain large ore deposits (Boschen et al., 2013; Hein et al., 2017), hydrocarbon resources, and natural gas in and beneath gas hydrates (Gautier et al., 2009). Thus, to expand their rights to the seabed and subsoil resources according to the United Nation's Commission on the Law of the Sea (UNCLOS) Arcticle 76, Arctic states have undertaken large geophysical and geological surveys. It is not only the Arctic states surrounding the AO that taken an interest in the region, other states such as Sweden or Germany, have completed many expeditions here for the purpose of science, specifically given that this region plays a key role in a global warming scenario.

AO exploration, specifically involving systematic scientific data acquisition, has been historically challenging due to the harsh conditions and the perennial sea ice. Nansen (1902) realized the first depth measurements in the central deep Arctic Ocean during The Norwegian North Polar Expedition (1893-1896), where the ship Fram drifted with the ice from the New Siberian Islands towards the Fram Strait. The result was the Bathymetrical Chart of North Polar Seas, a map showing the Arctic Ocean as one flat deep basin that extends at the base of the Circum-Arctic shelves. It was not until 1954 that the AO was found to be divided into two basins, when the Soviets shared discoveries from their NORTH-series and the NORTH POLE-series programs (Burkhanov, 1956). The United States started airborne expeditions and ice camps in the early 1950s, which were complemented by submarine exploration beginning 1957 (Weber, 1983). In 1958, the Polar Continental Shelf Project catapulted Canada to the front of the AO research. This organization cooperated with the Dominion Observatory to carry out the First Canadian North Pole Expedition in 1967, which provided invaluable information for planning the Second Canadian North Pole Expedition in 1969 and the Lomonosov Ridge Experiment in 1979 (Macinnis and Weber, 1980; Weber, 1979, 1980, 1983). New maps and charts of the AO were published as data of all these and other expeditions were being compiled. The Canadian Defence Research Board bathymetric chart of the AO compiled in 1956 was the first to show the Alpha Ridge separating the Makarov and the Canada basins (Weber, 1983); Another big step happened in 1975 when the American Geographical Society published the map that Bruce C. Heezen and Marie Tharp compiled based on all available unclassified soundings, including submarine echograms from Beal (1969;Weber, 1983). This map showed all the major features of the AO seabed, although the Gakkel Ridge was portrayed with numerous transform faults to make it look the same way as the Mid-Atlantic Ridge. The fifth Edition of the General Bathymetric Chart of the Oceans (GEBCO) published in 1979 (CHS, 1979) was a more detailed version that prevailed as the authoritative portrayal of the seafloor north of 64º N for more than two decades (Jakobsson et al., 2000).

From the late 1980s, the sea ice extent began a declining trend during summers (e.g. Cavalieri and Parkinson, 2012), successively opening some areas for easier access. Together with that the icebreakers became more capable and geophysical mapping instruments (e.g. multibeam echo sounders) were improved, a substantial increase in the quantity and quality of bathymetric data occurred. The International Bathymetric Chart of the Arctic Ocean (IBCAO) has compiled and integrated all these accumulated depth data in a coherent manner. IBCAO was initiated in 1997 in order to construct a digital database that contains all available bathymetric information north of 64º N (Macnab and Grikurov, 1997). Since then, four IBCAO versions have been released (Jakobsson, Macnab, et al., 2008; Jakobsson et al., 2000, 2012, 2020), with increasing coverage and resolution.

In terms of sub-surficial exploration, a series of tectonic maps were compiled during the 1960s and 1970s based on geological and geophysical data from AO expeditions (e.g. Atlasov, 1967; Egiazarov et al., 1977; Shatsky and Muratov, 1963). Later, Zarkhidze et al. (1991) compiled the Circumpolar map of Quaternary deposits of the Arctic, framed in the Programme of Scientific and Technical Cooperation between Canada and the U.S.S.R. in the Arctic and North. By means of extrapolation of seismic profiles, bathymetry (which has greater coverage) and sediment samples, they present a map showing the age and the source of the sediment deposits north of 64º N (Zarkhidze et al., 1991). More recently, the Atlas of 1:5 M Geological Maps of The Circumpolar Arctic was launched. This ambitious international project started to take shape in 2003 when the Russian Geological Research Institute made a proposal to coordinate international geological research in the AO. This was supported not only by the geological surveys of the Arctic countries but also by the UNESCO Commission for the Geological Map of the World. In 2005 the agreement was signed and the coordinating agencies of each map of the Atlas were assigned: Metallogenic Maps (Nordahl et al., 2016) and Magnetic and Gravity Field Maps (Gaina et al., 2011) coordinated by the Geological Survey of Norway, Geological Map (Harrison et al., 2011) by the Geological Survey of Canada, and Tectonic Map (Petrov et al., 2019) by the Russian Geological Research Institute (Petrov and Smelror, 2007; Petrov et al., 2016; Petrov and Smelror, 2015).

This master's thesis fits under the topic of geological maps by aiming to create a comprehensive surficial geology map that covers part of the Eurasia Basin of the AO, and part of the Fram Strait, Greenland Sea and Norwegian Sea (Fig. 1). The geology of the seafloor and uppermost sediment layers within reach of sub-bottom profilers (SBPs) is in focus. This will contribute to the "IBCAO Geology" project (Boggild et al., 2018; Mosher et al., 2015; van der Krogt, 2018), initiated by Mosher et al. (2015), which has as the goal to produce a seabed geology layer of the AO that compliments the bathymetric compilation IBCAO. To accomplish that, all available sub-bottom profiler data collected by icebreakers are being gathered and interpreted. The geological interpretation of sub-bottom profiles and the digitalization of the map is assisted by multibeam and seismic reflection data, and by geologic coring results where available. These data are first classified depending on the characteristics of the seafloor echo and sub-bottom reflections, following Boggild et al. (2018) acoustic facies classification scheme (see Section 4 for detailed information). Once the polygons of the acoustic facies type are created, they have to be interpreted in terms of the geologic process that dominates the area.

In this thesis, the following hypotheses will be tested: A surficial geology compilation based primarily on sub-bottom profiles serves as a good basis for (i) studies of past and present oceanographic, geologic, and glacial processes; (ii) environmental and geohazard assessments; and (iii) benthic habitat mapping. This hypothesis gives rise to a suite of scientific questions:

1. Is it possible to distinguish between present and past oceanographic and geologic processes solely using acoustic sub-bottom profiles?
2. To what extent can the seafloor morphology be used to spatially extend interpretations of sub-bottom profiles?
3. Does the research area fit with the sub-bottom classification scheme used for the Amerasia Basin?

# 2 The Arctic Ocean

This chapter aims to give a general background of the AO, and given that this study covers part of it, understanding the entire region is important for analysing the data more rigorously. Furthermore, this is a continuation of the IBCAO Geology project (Boggild et al., 2018; Mosher et al., 2015; van der Krogt, 2018) which already mapped other parts of the AO, and here I adapt their classification scheme and general geological interpretations given to each acoustic facies type based on the areas they mapped. This means that comparisons between facies from distinctly different AO provinces will be made.

In the sections of this chapter I will go through how the AO seafloor looks like from different geoscientific-perspectives. The tectonics behind the seafloor geology will be addressed as well as hypotheses about dynamics of ice masses during the Quaternary and their traces left in the seabed, and how the sediment and water masses move in the AO.

## 2.1 Geological setting

### Physiography

The AO is the smallest and shallowest of all the major oceans (Menard and Smith, 1966). It comprises an area of ∼4.3 % of the total World Ocean area, a volume of ∼1.4 %, and has a mean depth of 1201 m (Jakobsson, 2002). These numbers were derived using the International Hydrographic Organization (IHO) definition of the AO in Publication S-23 "Limits of Oceans and Seas" ((IHO), 2002) and the IBCAO Version 1.0 gridded bathymetric model (Jakobsson and Cherkis, 2001). However, in scientific literature, the AO is commonly defined from its physiography, i.e. the almost landlocked ocean around the North Pole, consisting of a deep ocean basin with submarine ridges and marginal plateaus within, that is surrounded by continental shelves (Jakobsson et al., 2004; Weber, 1989). This implies a much smaller area than the IHO-defined AO, which includes the Norwegian, Greenland and Iceland seas as well as Davies Strait and Baffin Bay. From hereafter I will use Jakobsson's (2002) definition, including the deep ocean basin, the wide European and Siberian continental shelves where the Barents, Kara, Laptev, East Siberian and Chukchi Seas are located, the narrower continental shelves of North America and northern Greenland where we find the Beaufort and Lincoln Seas, also including the White Sea, and the shelves of Northwestern Svalbard, Northeastern Greenland and Northern Canadian Arctic Archipelago (Fig. 1).

The shallow continental shelves (from the coastline to the shelf break) of the AO cover more than 50 %, but they contain less than 6 % of the total volume (Jakobsson, 2002). These are unique values considering that in the rest of the oceans, the continental shelves together with the slope cover only from 9.1 % to 17.7 % of their respective ocean area (Menard and Smith, 1966). The deep central basin, which comprises ∼47 % of the total AO area and nearly 95 % of the volume, is surrounded by continental shelves in all its points but one, the Fram Strait, between Northeastern Greenland and Northwestern Svalbard (Jakobsson, 2002). Within the basin the following features are found, from the most to the least extensive provinces: ridges, covering ∼15.8 % of the AO; abyssal plains (∼11.8 %); continental rises (∼7.7 %); continental slopes (∼5.7 %); perched continental rises (∼3.8 %); perched abyssal basins (∼2.3 %); submarine highlands (included in the abyssal and perched abyssal plains); and isolated basin (∼0.2). These submarine features for which percentages are calculated by Jakobsson et al. (2003) might not fit perfectly with respect to their classification with the IHO-IOC GEBCO "Gazetteer of Undersea Feature Names" (GEBCO, 2024). The reason for this is that the classification of some physiographic provinces, e.g. whether it is a ridge or spur, may vary depending on the context. A clear example is the Nautilus Basin considered a perched abyssal plain by Jakobsson et al. (2003) while it is referred to as the Mendeleev Abyssal Plain in the IHO-IOC GEBCO (2024). In this project, I have refrained to use the feature classification of IHO-IOC GEBCO (2024) as the standard for the names of the features.

The Lomonosov Ridge (Fig. 1) divides the basin into two major sub-basins, which are the Amerasia Basin and the younger Eurasia Basin. This ridge, described as a "double-sided passive margin" (Jokat et al., 1992), is an almost 1800 km long narrow fragment of continental crust that extends from the Lincoln Shelf to the north of New Siberian Islands in the East Siberian Shelf. It has steep flanks and a relatively flat top, with a width ranging from 45 to 200 km, and heights sticking up from the surrounding seafloor as much as 3500 m. An erosional unconformity around 500 m below the top of the ridge has given a clue about the flatness of this structure, which Jokat et al. (1995) explained to be a result of strong subaerial and shallow water erosion during the subsidence of the ridge. However, the glacial history addressed below may also have played a large role with the respect to the flat-topped crest's appearance.

The Amerasia Basin (Fig. 1) is bounded by the Lomonosov Ridge, the Canadian, Alaskan and

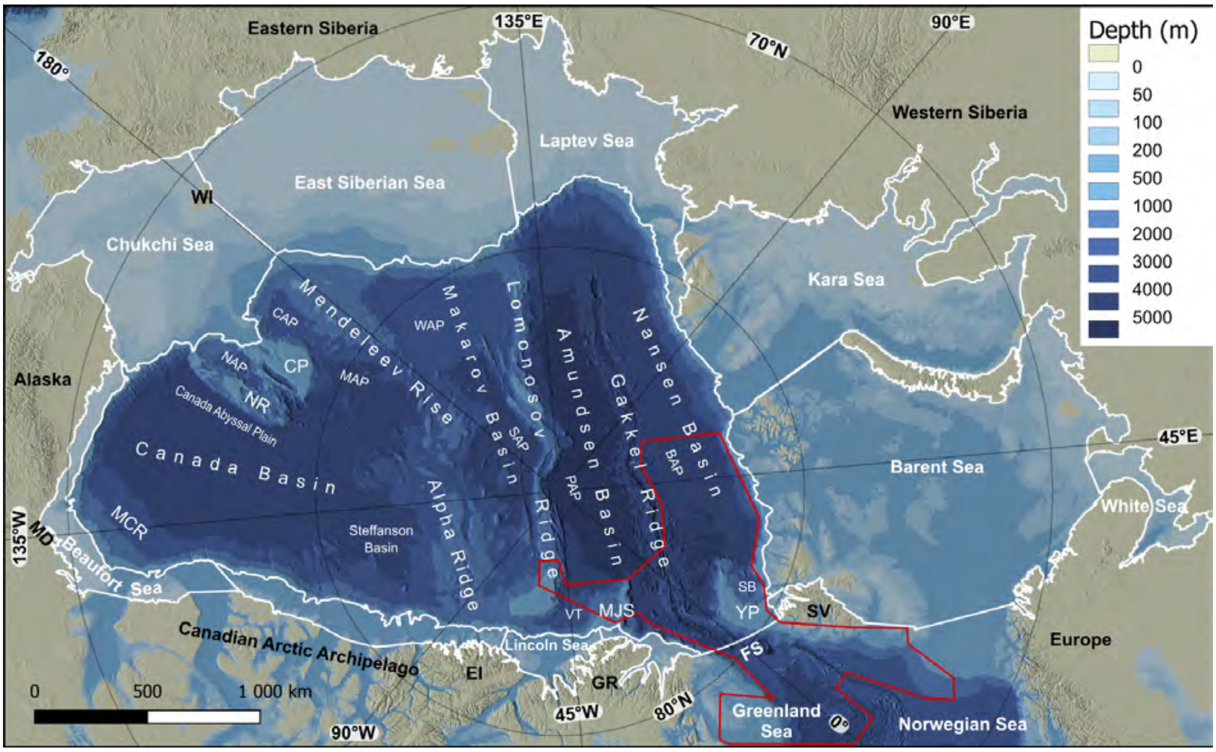


**Figure 1**. Overview map of the AO showing the main bathymetric features. The white lines confine the area under Jakobsson et al. (2002) definition of the AO, also delimiting the central basin and the different seas. The red line confines this study area of interest. Base map from IBCAO Ver. 4.2 by Jakobsson et al. (2020). BAP: Barents Abyssal Plain; CAP: Chukchi Abyssal Plain; CP: Chukchi Plateau; EI: Ellesmere Island; FS: Fram Strait; GR: Greenland; MAP: Mendeleev Abyssal Plain; MCR: Mackenzie Continental Rise; MD: Mackenzie Delta; MJS: Morris Jesup Spur; NAP: Northwind Abyssal Plain; NR: Northwind Ridge; PAP: Pole Abyssal Plain; SAP: Siberia Abyssal Plain; SB: Sophia Basin; SV: Svalbard; VT: Voronov Terrace; WAP: Wrangel Abyssal Plain; WI: Wrangel Island; YP: Yermak Plateau.

East Siberian continental shelves, and the shelf of the Chukchi Sea. In this case, the submarine feature that subdivides the basin is the Alpha-Mendeleev Ridge complex, leaving on its south the Canada Basin, and on its north the Makarov Basin. The Alpha-Mendeleev Ridge (Fig. 1), with a total area of more than 700 000 km$^2$ (Jakobsson et al., 2003), is the largest physiographic feature of the AO. It is a 1700 km long and 200 to 700 km wide morphologically complex feature that extends from the northwest of Ellesmere Island in the Canadian Continental Shelf to the north of Wrangel Island in the Russian Continental Shelf. The ridge axis is typically between 1500 m and 3000 m below actual sea level in the centre, and between 800 m and 2000 m at the edges. Numerous seamounts are located here. The top of the ridge is covered by less than about 1.5 km of probably Cenozoic hemipelagic drape (Bruvoll et al., 2010), which is also shown in Boggild et al. (2018) surficial geology map. However, the stratigraphy can become complex in the bathymetric lows, with substantial unconformities and mass-wasting deposits (Boggild et al., 2020; Brumley, 2014; Bruvoll et al., 2010; Hegewald and Jokat, 2013; Shimeld et al., 2011; Weigelt et al., 2014). Compared to the Mendeleev Rise, the Alpha Ridge is in general wider and less blocky (Coakley et al., 2016).

The Canada Basin (Fig. 1) is bounded by the Mackenzie Continental Rise at its south, the Northwind Ridge at its west, the informally named Nautilus Basin at its north-west, the Alpha Ridge at its north, the Stefansson Basin and the Sever Spur at its north-east, and the Canada-Greenland Rise at its east. This basin lies at around 3800 m below sea level, covering an area of almost 500 000 km$^2$, and is extremely flat, rising less than a hundred metres from west to east and from south to north. The sediment thickness is estimated to increase eastwards until arriving at the Mackenzie Delta, with more than 15 km of sediment (Grantz et al., 2011; Helwig et al., 2011; Mosher et al., 2012). In the delta, seismic profiles show reflections representing stacked mass-failure deposits. These reflections become more coherent towards the Canada Basin, where they remain continuous and parallel for hundreds of kilometres, interpreted as hemipelagic deposits interbedded with turbidite sequences (Coakley et al., 2016). The main physiographic province within the Canadian Basin is the Canada Abyssal Plain.

The Makarov Basin (Fig. 1), adjoining the Lomonosov Ridge, the Alpha-Mendeleev Ridge, and the East Siberian Shelf, is composed of the smaller Siberian Abyssal Plain at the northernmost part and the Wrangel Abyssal Plain at the other side. The Siberia Abyssal Plain is around 4000 m deep with a sediment thickness of less than 3.5 km, whereas the Wrangel Abyssal Plain depth increases northwards from around 2600 to 3300 m with a 4-6 km thick sediment cover. These numbers reflect the restricted sediment transport from the south due to the basement ridge between both abyssal plains (Kutschale, 1966; Lebedeva-Ivanova et al., 2006; Sorokin et al., 1999). Therefore, the Siberian Abyssal Plain seemed to have another sediment source, and according to onlapping structures in the Lomonosov Ridge, Jokat (2005) proposed the Eurasian Margin during the Cretaceous (when the Lomonosov Ridge was still part of the Eurasian Shelf).

Connected to the shelf of the Chukchi Sea we find the Northwind Ridge and the Chukchi Plateau, both separated by the isolated small Northwind Abyssal Plain (Fig. 1). The grouping of these parallel NNE-SSW-trending basins and plateaus is informally known as Chukchi Borderland. This $\sim$400 x 600 km bathymetric high is generally considered a thinned continental fragment (Hall, 1990; Hunkins, 1966; Klemperer et al., 2002; Laxon and McAdoo, 1994; Wolf et al., 2002). The east flank has slopes that can surpass 30°, going from the Canada Abyssal Plain at almost 3900 m deep to the top of the Northwind Ridge, usually shallower than 1000 m deep. The west flank is less steep with less than 2000 m of relief from the Chukchi Abyssal Plain to the top of the Chukchi Plateau. The north flank is composed of a bathymetrically complex ramp at the west, and an elongated escarpment that penetrates the basin at the east. Between the Chukchi Plateau and the Mendeleev Rise, we find the Chukchi Abyssal Plain just off the continental slope, and the Mendeleev Abyssal Plain at the north-west of the plateau.

The Eurasia Basin (Fig. 1) is bounded by the Lomonosov Ridge, the shelves of the Barents, Kara and Leptev Seas and Northern Greenland, and the Fram Strait. Here, the Gakkel Ridge bisects it into the Amundsen and Nansen Basins. The Gakkel Ridge (Fig. 1), with spreading rates of 13 mm/yr near Greenland and 6 mm/yr near the Laptev Sea, is the slowest spreading ridge on Earth (Cook et al., 1986; Glebovsky et al., 2006; P. R. Vogt et al., 1979). It extends for more than 150 000 km from the Lena Through (northeastern Greenland, where the ridge changes its NE-SW direction for a NW-SE direction) until it gets buried by Cenozoic sediment (Pease et al., 2014) near the continental slope of the Laptev Sea. It keeps the shape of the early continental rifting since it still conforms to the Lomonosov Ridge. It is shocking the absence of transform faults along the ridge, but the combination of morphological, tectonic, and magmatic segmentation typical of ultraslow-spreading ridges is found (Dick et al., 2003). The axis of the ridge consists of a big through that surpasses 5000 m deep in some places. Moving away from the axis, we find large ridges and mountains that are aligned relatively parallel to the axis, until these get completely covered by sediments deposited in the Amundsen and Nansen basin.

The Amundsen Basin lies between the Lomonosov Ridge and the Gakkel Ridge, whereas the Nansen Basin lies on the other side of the Gakkel Ridge (Fig. 1). In these basins, we find the Pole Abyssal Plain and the Barents Abyssal Plain respectively. The Amundsen Basin is flatter, deeper ($\sim$4000-4500 m), and with thinner sedimentary cover ($\sim$3.5 km in the centre of the basin), whereas the Nansen Basin ranges from depths around 3200 m near the Laptev continental margin to 4000 m and 4.5 km thick sediment cover near Barents continental margin. Then, depth itself gives a relative idea of the sedimentation rates in both basins (Backman et al., 2004), and Johnson (1969) suggested that the rates in the Amundsen Basin are lower because the Gakkel Ridge prevents terrestrial sediment input from the Eurasian continental margin, whereas the Nansen is connected with this sediment source area over most of its length.

In the Eurasia Basin there are also two smaller ridge systems: the Yermak Plateau, connected to the shelf of Northwestern Svalbard; and the Morris Jesup Spur, connected to the shelf of Northeastern Greenland (Fig. 1). The shape of the Yermak Plateau is like an inverted "L", extending from the shelf in a SW-NE direction and culminating in the Nansen Basin with a SE-NW direction. The north and northwest flanks are steeper, rising from 3800-4000 m deep to less than 800 m. The Sophia Basin separates it from the continental shelf of the Barents Sea.

The Morris Jesup Spur extends more than 200 km basinward with a steeper north-east flank that surpasses slopes of 40° and with a maximum of 52.8°, one of the steepest points in the AO. It rises around 2700 m from Voronov Terrace, which lies between the spur and the Gakkel Ridge.

### ***Tectonic Evolution***

The tectonic evolution of the AO is connected to the position of the boundaries between the Pacific, North American, and Eurasian lithospheric plates, mainly determined by the difference in subsidence velocities of the Pacific Plate under the North American and Eurasian plates (Petrov, Kashubin, et al., 2021). The initial formation of the first part of the Arctic Ocean, i.e. the Amerasia Basin, has been widely debated. Here I will present the tectonic history from literature, without evaluating which of the theories are more valid than others.

The formation of the features that we find today in the AO started in the early Mesozoic (Petrov, Kashubin, et al., 2021), but it was not until early Jurassic when the formation of the oceanic crust of the Canada Basin started with the extension and thinning of continental lithosphere. The seafloor spreading begun around 130 Ma (Embry, 1993; Grantz et al., 1990; Grantz et al., 2011). During these periods, the boundary between the Eurasian and North American plates was extending along this rifting region (Petrov, Kashubin, et al., 2021). In the Aptian (∼120-110 Ma), the development of the high Arctic large igneous province (HALIP) started, causing both the emplacement of mafic magma into and underlying the lithosphere, and the extension of the lithosphere (Pease et al., 2014). Due to a change in kinematics of the Eurasian and the North American plates at the turn of the Mesozoic and Cenozoic, the formation of the Eurasian Basin started with a rift (Gakkel Ridge) that splintered apart the Lomonosov Ridge from the Barents-Kara continental margin, with a first stage of rifting between late Cretaceous and early Eocene (∼80-55 Ma), and a second stage at the second half of the Miocene (∼14-5 Ma; Drachev, 2011; Franke et al., 2001). The boundary between both lithospheric plates was set since along the Gakkel Ridge and in the Laptev Sea following a series of rift depressions.

Thus, the Amerasia Basin was formed during the Mesozoic and has remained tectonically inactive since then, whereas the seafloor spreading that opened the Eurasia Basin started later and is still ongoing. Compared to the well-constrained tectonic evolution of the Eurasia Basin, the kinematic history of the Amerasia Basin and the origin of most of the features within are still under debate. The complex evolution resulted in an Amerasia Basin mainly composed of continental crust that was thinned and reworked by the HALIP (Petrov, Kashubin, et al., 2021). The Siberia Abyssal Plain and the center of the southern part of the Canada Basin are the only areas of this basin where evidence of oceanic crust is found. In the Canada Basin, this fact is supported by seismic reflection and refraction data (Grantz et al., 2011; Mosher et al., 2012), gravity anomaly patterns extrapolated from the southern Beaufort Sea area (Stephenson et al., 1994), linear magnetic anomalies (Taylor et al., 1981), and the observations of Døssing et al. (2013). The oceanic nature of the Siberia Abyssal Plain crust is more controversial, but the crustal thickness and the absence of a significant reflector between the Moho and the top of the basement suggest a thickened oceanic crust (Pease et al., 2014). Nevertheless, Evangelatos and Mosher (2016) interpreted the acoustic basement as intrusive and extrusive rocks of the HALIP, so the crust in this abyssal plain is either considered continental reworked by HALIP or oceanic. The presence of oceanic crust in the Siberia Abyssal Plain would imply seafloor spreading from the Beaufort Sea to the northernmost part of the Makarov Basin during the Lower Cretaceous (Pease et al., 2014). It is more accepted though, the continental nature of the crust in the Wrangel Abyssal Plain and the Alpha-Mendeleev Ridge. Both are considered heavily attenuated and intruded continental crusts that resulted from intense mafic magmatism of the HALIP (Døssing et al., 2013; Pease et al., 2014). However, some researchers proposed the interaction between the HALIP and seafloor spreading, along or perpendicular to the Alpha-Mendeleev Ridge, to form thickened oceanic crust, similar to the crust of Greenland-Iceland-Faroe Ridge (Forsyth et al., 1986; Funck et al., 2011; Grantz et al., 2011; Jackson et al., 1985; Lawver and Müller, 1994). Kashubin et al. (2021) concluded that any uplift structure in the central AO cannot be assigned to the oceanic type with the data available. The Chukchi Borderland was long ago inferred as a continental fragment (Dietz and Shumway, 1961; Hall, 1990; Jokat et al., 1992) and modern data seems to confirm it (Dove et al., 2010), although its origin and pre-rift position remain under debate. Probably the model from Grantz et al. (2011) is the most considered and explains that the Chukchi Borderland was rifted from the shelf of the Canadian Arctic to the East Siberian shelf. Then it was separated from the Siberian shelf with a clockwise rotation that placed it over the Canada Basin.

In the opening of the Eurasia Basin, the Lomonosov Ridge was separated from the shelves of the Barents and Kara seas, then it subsided below sea level during the beginning of the Eocene (2006) but remained shallow until the early Miocene (2008). HALIP manifestations in the Lomonosov Ridge are restricted to local areas (Petrov, Pubellier, et al., 2021). Then, the continental nature of the crust in this ridge is recognized by most of the researchers. The oceanic crust of the Eurasia Basin is atypically thinner in the older parts, which suggests mantle exhumation in these areas (Pease et al., 2014). At the same time, it is thinner beneath the Amundsen Basin compared to the Nansen Basin, explained by the lower spreading rates on this side of the Gakkel Ridge (1979). The Yermak Plateau and the Morris Jesup Spur are thought to be separated by the seafloor spreading just as the Lomonosov Ridge was separated from the Eurasian continental margin. This occurred along the Gakkel Ridge in the southwest part of the Eurasia Basin during the early Oligocene (2003, 1979). Kristoffersen et al. (2020) defined the southern and northwestern Yermak Plateau as a continental outlier. For the northeastern part, Jokat et al. (2008) support a stretched and intruded continental crust, that is afterward overprinted by basalt production when it separates from the Morris Jesup Spur. A new study proposes the geological evolution of the southwestern and northeastern Yermak Plateau to be different. The former formed in a continental extensional regime at the north of Svalbard, and the second derived from the North American plate that was then separated from the Morris Jesup Spur and merged to the southwestern part by seafloor spreading (Estrada et al., 2024). Moving away from the deep basins, the continental shelfs of the AO are characterized by thinned continental crust of similar thicknesses but variable structures (Kashubin et al., 2021).

In summary, the physiographic provinces of the AO are the result of a common evolution and were then subdivided by neotectonics submergence of the central AO (Kashubin et al., 2021). The extensional phases during the Jurassic in the Canadian-Alaskan Arctic, and during the Cretaceous in the Eurasian continental margin, which are related to the breakup of the supercontinent Pangea and Eurasia, created new oceanic lithosphere after the breakup and rifting of the continental lithosphere (Pease et al., 2014). The development of large igneous provinces and extensional attenuation rejuvenated the existing lithosphere.

## 2.2 Glacial History

Earth's Cenozoic glacial history is characterized by its change from a greenhouse state to a state where ice sheets are continuously waxing and waning at about 33 Ma (Zachos et al., 2001). Mudelsee and Raymo (2005) found that the glaciation of the Northern Hemisphere was a gradual transition that started 3.6 Ma and finished 2.4 Ma, with an intensification around 2.7 Ma (Raymo, 1994; Shackleton et al., 1984). After the glaciation, the first part of the record show a 41-ka glacial-interglacial periodicity, that shifted to a 100-ka periodicity between 1.2 and 0.8 Ma in the so-called "mid-Pleistocene transition" (Ruddiman et al., 1986).

Glacial-interglacial cycles are characterized by the progressive growth of ice sheets moving to a glacial stage and the relatively abrupt retreat of ice sheets moving to an interglacial stage. These cycles are mainly driven by the orbital configuration of the Earth (Hays et al., 1976) which acts as the pacemaker, and by the Earth system processes and feedbacks which magnify the subtle changes that the orbital forcing caused (Imbrie et al., 1993; Ruddiman et al., 1986; Shackleton, 2000). Ice sheets are those glaciers (perennial accumulation of ice, snow, rock, sediment, and liquid water that forms on land and flows by the action of gravity) that extend in continuous sheets covering more than 50 000 km$^2$. The floating parts of the ice sheets that extends into the ocean are called ice shelves.

During the Quaternary, AO physiography and environment have been subjected to dramatic changes caused by these glacial-interglacial cycles (Jakobsson et al., 2014). Since the 19$^{th}$ century, many hypotheses about the ice conditions in the AO during the Quaternary have been postulated, and are still an ongoing debate. The speculation about an extensive thick floating ice mass started in 1888 with Thomson (1888) and was refined later thanks to deduction from direct observational data (Broecker, 1975; Hughes et al., 1977; Mercer, 1970). Now we talk about the possibility of a km-thick ice shelf covering the entire central AO during the marine isotope stage (MIS) 6 ($\sim$140 ka) and potentially older glacial periods (Jakobsson, Nilsson, et al., 2016; Fig. 2). This hypothesis is supported by geophysical data showing evidence of ice grounding and sub-bottom glacial erosional unconformities at the Lomonosov Ridge (Jakobsson, 1999; Jakobsson, Nilsson, et al., 2016; Jakobsson, Polyak, et al., 2008; Jakobsson et al., 2010), East Siberian Continental Margin (Dove et al., 2014; Niessen et al., 2013), the Yermak Plateau (J. A. Dowdeswell et al., 2010; Jakobsson et al., 2010), the Chukchi Plateau (Dove et al., 2014; Jakobsson, Polyak, et al., 2008; Polyak et al., 2001), the Mendeleev Rise (Jakobsson, Nilsson, et al., 2016; Joe et al., 2020) and the continental slope at its south (Jakobsson, Nilsson, et al., 2016), and the Alaska-Beaufort margin (Engels et al., 2008); by the analysis of sediment cores retrieved from the East Siberian shelf, the De Long Trough (Alatarvas et al., 2022; O'Regan et al., 2017), the Lomonosov Ridge (Geibert et al., 2021; Jakobsson, Nilsson, et al., 2016; Jakobsson, Polyak, et al., 2008), the Mendeleev Rise (Geibert et al., 2021; Song et al., 2024), the region north of the Chukchi Plateau, the Morris Jesup Spur, the Yermak Plateau, the Fram Strait, and the Vöring Plateau (Geibert et al., 2021); and by ice models that explain how this ice-sheet could be formed (Gasson et al., 2018) and its dynamics (Nilsson et al., 2017).

However, this hypothesis has always faced opponents. Before the discovery of glacial erosion in the Lomonosov Ridge, most scientists agreed on an AO similar to the one today, consisting of seasonal sea ice (J. F. Bischof and Darby, 1997; D. L. Clark, 1990; Ishman et al., 1996; Phillips and Grantz, 2001). Kristoffersen et al. (2004) suggested armadas of large icebergs embedded in sea ice to be the explanation for the erosion documented on the crest of the Lomonosov Ridge in 1996 (Jakobsson, 1999). A similar explanation was given by Schlager et al. (Schlager et al., 2022), who termed the ice mass grounding at the Lomonosov Ridge as a composite ice mass (sea ice that encloses thicker fragments from calving events) with variable thickness. Jakobsson et al. (2010) did first conclude that the 1 km thick ice shelf in the central AO can be rejected since areas of the Lomonosov Ridge shallower than 1000 m below present sea level appeared to not show any sign of ice erosion. However, with the clear evidence of ice grounding from multibeam bathymetry and sub-bottom profiles gathered in 2014 from several parts of the Arctic Ocean during the SWERUS-C3 expedition, they changed their interpretation and proposed a complete cover of an ice shelf during the penultimate glaciation and/or earlier (Jakobsson, Nilsson, et al., 2016). The gaps that Geibert et al. (2021) found in the 230Th stratigraphy of the AO and the adjacent Nordic seas, which were interpreted as an ocean not only covered by a thick ice shelf but also filled with fresh water, encountered rivalry with the explanation that Spielhagen et al. (2022) gave to this low 230Th. Kim et al. (2021) and Lehmann et al. (2022) defend that the glacial features at the outer Chukchi Shelf and Chukchi Borderland were formed by the interaction of local ice sheet-shelf systems in the region.

This way, we still lack information for a comprehensive understanding of the AO glacial history. The advancing of this knowledge is crucial for a better understanding of how global climate changes affect the ice sheet dynamics, which in turn have an impact on the Arctic environment, the sea level, and the global ocean circulation patterns. The ice-sheet extent reconstructions serve as a valuable input for earth systems and global climate models that span the Quaternary (Batchelor et al., 2019), also providing key information for future sea-level change projections (DeConto and Pollard, 2016).

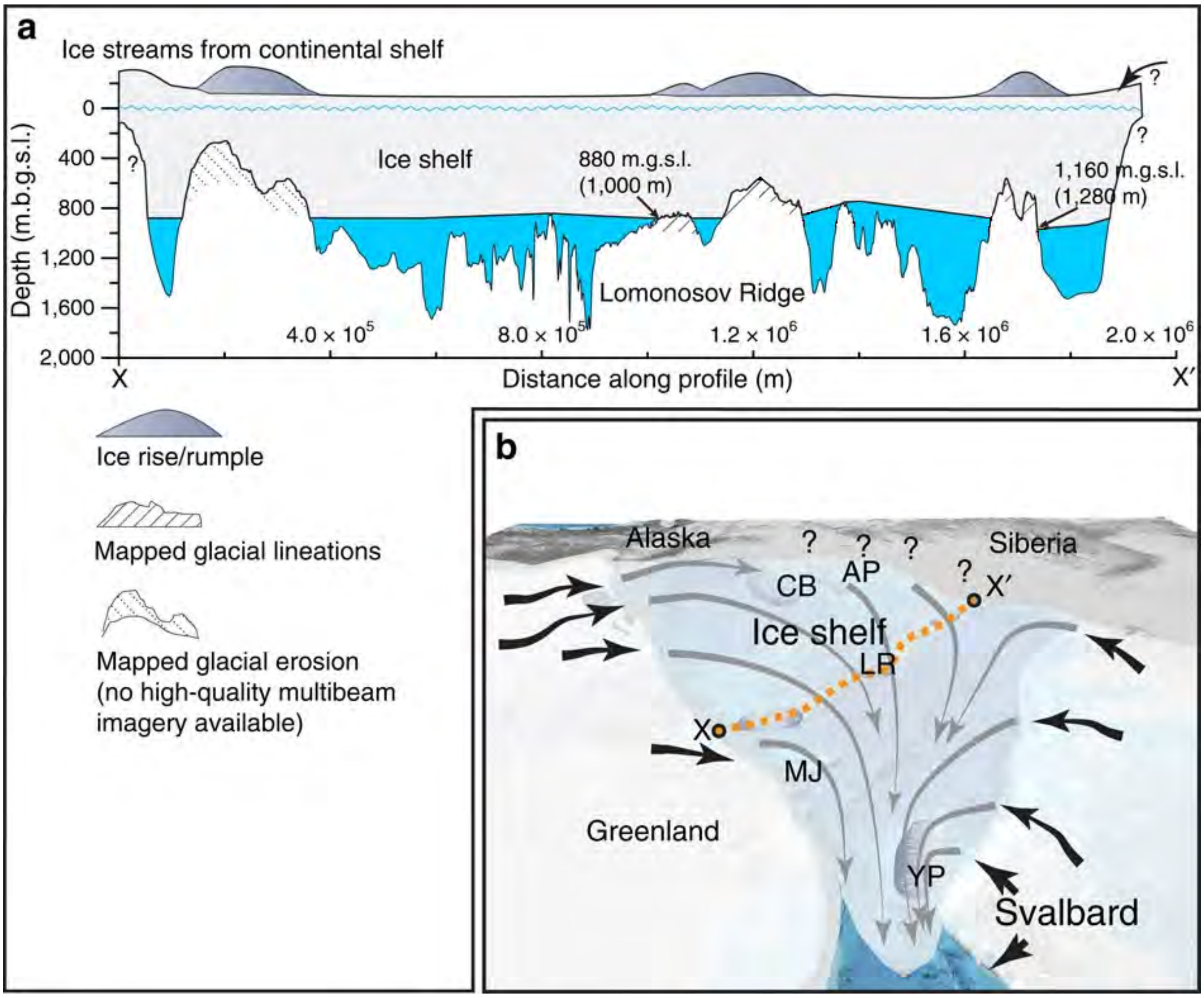


**Figure 2**. Schemes of the hypothesised ice shelf that covers the entire AO flowing toward the Fram Strait, adapted from Jakobsson et al. (2016) by using GIMP (Kimball et al., 2021). (a) Bathymetric profile crossing the Lomonosov Ridge from the Greenland margin (X) to the Siberian margin (X') showing where ice erosion is identified and the thickness that the ice shelf should have to explain that erosion. See the location of the profile in Fig. 2b. m.g.s.l: metres below glacial sea level, defined in that paper as 120 m below present sea level. (b) Sketch of the ice shelf from above with flow lines inferred from mapped glacial landforms. Grey arrows represent the flow lines of the ice shelf, and their thickness symbolises the thickness of the ice shelf. Black arrows represent the flow lines of the ice streams that feed the ice shelf. AP: Arlis Plateau; CB: Chukchi Borderland; LR: Lomonosov Ridge; MJ: Morris Jesup Rise; YP: Yermak Plateau.

## 2.3 Sedimentary processes and patterns

Here I present a summary of the most common sedimentary processes that occur in the AO, as well as the changes in the patterns during the Quaternary. The analysis of seafloor sedimentary records and the geophysical mapping of the seafloor are the main tools for reconstructing past environments, disentangling its oceanic circulation, sedimentary processes, biological production, and ice dynamics, critical for understanding anthropogenic climate change and simulating future scenarios (Polyak and Jakobsson, 2011).

Deep-sea sediments are usually classified as terrigenous, which are those produced on land by chemical weathering and erosion, and transported to the coastal areas by the wind, the rivers, or the glaciers; biogenic, which are the remains of the living organisms that lived in the water column; and authigenic, which are those formed in situ by inorganic precipitation of the minerals on the seafloor and the sub-bottom. Once in the oceanic realm, oceanic circulation further distributes the sediments, even resuspending sediment previously deposited (Biscaye, 1965). In shallow coastal areas, waves, tides, and wind-driven currents are the oceanic agents producing erosion, transport, and deposition, whereas near the seafloor these agents are the bottom currents. The action of the waves is gaining importance in the AO as the sea ice cover decrease (J. Thomson et al., 2016; Wang et al., 2015). Tides are key for the development of moraines since they shape glaciers with a grounding line (the place where the ice sheet ceases contact with the floor) that coincides with the calving line, allowing deposition with no height restriction there (R. D. Powell and Molnia, 1989; R. D. Powell, 1990). Bottom currents are any persistent currents in contact with the seafloor that flow preferentially along-slope with varying velocities (Camerlenghi, 2018). These currents capture and transport suspended sediment from the vertical settling and gravity flows, and can even erode sediment particles already settled if the velocity is high enough (Camerlenghi, 2018). The resulting depositional landforms formed when the current velocity decreases and the particles settle are called contourite or sediment drifts (Rebesco, 2005; Rebesco et al., 2008; Rebesco et al., 2014; Stow and Faugères, 2008; Stow et al., 2008; Stow et al., 2002).

The terrigenous and biogenic clays suspended in the water column can settle on the seafloor by gravity, draping it without modifying the underlying substrate and smoothening the relief (Camerlenghi, 2018). This is the so-called vertical settling, which forms the pelagites and hemipelagites (Stow and Piper, 1984). The melting of icebergs and sea ice also contributes to the vertical settling by releasing the sediment they retain (Nürnberg et al., 1994; Wahsner et al., 1999). However, it is more likely that the sediment is transported to deep basins via gravity flows. A type of gravity flow is turbidity currents, which are hyper-pycnal mixtures of water and suspended sediment that flow downslope also by gravity due to their higher density (Parsons et al., 2007). As they flow across the slope they have high erosional power (Mohrig and Marr, 2003; Piper and Normark, 2009; Pratson et al., 2000), and when arriving at lower slopes they progressively lose velocity until all sediment settles out, becoming depositional (Amblas et al., 2018). These currents can continue in case they stay in confined conduits, forming submarine channels (e.g. Boggild and Mosher, 2021) and potentially submarine fans (Camerlenghi, 2018). Turbidity currents are also responsible for forming submarine canyons and turbidites. Even more common in the high latitude continental margins are the debris flows, triggered mainly during glacial maximums when the grounding lines of the glaciers arrive at the shelf edge and deliver sediment directly to the upper continental slope (Camerlenghi, 2018). The result of these glacigenic debris flows is the trough-mouth fans, the major offshore depocenter in this region. Other gravity flows are the submarine landslides, one of the largest natural events on Earth, preconditioned and triggered by a variety of factors such as rapid sediment accumulation during full-glacial periods, bottom currents, tectonic activity, and gas hydrate dissociation (Laberg and Vorren, 2000; Mienert, 2004; Mosher et al., 1994). During deglaciations, glacier retreat occurs in steps, so the still-stand periods of the glaciers allow depositions of the sediments present at the glacier as it melts, forming features such as grounding zone wedges (GZWs) and moraine ridges (R. Powell and Domack, 2002; R. D. Powell and Alley, 1997).

Lastly, the authigenic minerals can be formed by various processes of chemical precipitation such as methane-derived carbonate precipitation (Kravchishina et al., 2017; Lein, 2004) and reprecipitation of Mn by organic matter degradation (März et al., 2011; Yuan-Hui Li et al., 1969).

The different sedimentary patterns, and thus the provenance of the sediments lying at the different AO basins, are largely determined by the Trans-Polar Drift and the Beaufort Gyre (see Section 2.5 for more details about circulation), which have been the main surficial circulation systems at least the last 650 ka (Polyak and Jakobsson, 2011). During interglacials, moderate sedimentation rates varying from several millimetres to 2 cm/ka were mainly delivered from sea ice melting (Backman et al., 2004; Polyak et al., 2009; Stein, Matthiessen, Niessen, et al., 2010). Interglacial sediments enriched in planktonic foraminifera also indicate higher biological productivity enhanced by more open ice conditions (Nørgaard-Pedersen et al., 1998), and/or higher biogenic input from the continental shelves (Polyak and Jakobsson, 2011). Thick sea ice cover within the Beaufort Gyre caused lower sedimentation rates in the Amerasia Basin (Polyak and Jakobsson, 2011). Full glacial periods are characterized by extremely low sedimentation rates, meaning very low productivity and low ice-rafted debris (IRD) delivery, primarily thanks to the presence of packed stable sea ice (Nørgaard-Pedersen et al., 1998). We mostly find this stratigraphic interval in cores retrieved from the Amerasia Basin, likely due to the sediment delivered by meltwater from the ice sheets and the outburst of subglacial lakes (Adler et al., 2009; Polyak et al., 2009; Yamamoto and Polyak, 2009). The extended ice sheets and the lower sea level prevented riverine inputs (Nørgaard-Pedersen et al., 1998). The deglacial events following the glacial maximums were accompanied by dramatically increased sedimentation rates that exceeded 10 cm/ka (Adler et al., 2009), originating from IRD discharge from the icebergs that arrive at the central AO after massive calving events (Polyak and Jakobsson, 2011). In the Amerasia Basin, these stratigraphic intervals contain sediments of Canadian Shield provenance (J. Bischof et al., 1996; Phillips and Grantz, 2001; Polyak et al., 2009; Stein, Matthiessen, and Niessen, 2010; Stein, Matthiessen, Niessen, et al., 2010; Yurco et al., 2010), whereas the Eurasia Basin and Central Lomonosov Ridge contain sediments traced to Barents-Kara Ice Sheet (O'Regan et al., 2008; Spielhagen et al., 2004), and the region north of Greenland traced to Ellesmere Island and Greenland (Nørgaard-Pedersen et al., 2007).

## 2.4 Submarine glacial landforms

Ice sheets advance and retreat shape the land below and beyond them, affecting about 20 % of the global ocean today and affecting a much larger area during past full-glacial conditions (J. A. Dowdeswell, Canals, et al., 2016a). These features sculptured by ice masses are called glacial landforms, and the study of the ones exposed sub-aerially started more than a century ago (e.g. De Laski, 1864). However, the subaerial erosion and human activity disrupt the glacial record on land. This is why during the last few decades, as the marine geophysical data acquisition systems were being improved, the study of well-preserved submarine glacial landforms began to be in the spotlight (J. A. Dowdeswell, Canals, et al., 2016a). It has to be said that these landforms can also be reworked by the action of icebergs, other marine-geological processes such as currents and submarine landslides, and by human activity like natural resources exploitation (J. A. Dowdeswell, Canals, et al., 2016b). The analysis of the nature and distribution of the submarine glacial landforms exposed at the seafloor or buried below it provides key information on former ice sheets' extent, growth, decay, and the changing dynamics and complexities involved (J. A. Dowdeswell, Canals, et al., 2016b; Mosola and Anderson, 2006).

Cross-shelf troughs are relatively large and deep bathymetric depressions that result from the erosion of the continental shelf (Batchelor and Dowdeswell, 2014; J. A. Dowdeswell and Siegert, 1999; Vorren and Laberg, 1997). This erosion is thought to be caused by fast-flowing ice streams during at least one, and more likely several, glacial cycles. This way, the presence of cross-shelf troughs indicates the location of former fast-flowing ice streams (e.g. Ship et al., 1999; Stokes and Clark, 2001), key for understanding past ice sheets since these ice streams are responsible for 80 % of the mass loss of modern Greenland and Antarctic ice sheets (Rignot et al., 2011; Rignot and Kanagaratnam, 2006). The submarine glacial landforms, typically present at the cross-shelf troughs, that indicate past ice-flow directions and velocities (Stokes and Clark, 2002a) are the streamlined subglacial landforms, which include mega-scale glacial lineations (MSGLs), drumlins, flutes, and crag-and-tails (Fig. 3b). MSGLs represent the end-point of these elongated ice-flow aligned features and are sedimentary ridges up to tens of km long, hundreds of m wide, and amplitudes of a few metres, which are organized with regular spacing in a parallel to subparallel way (Stokes and Clark, 2002b). The transverse-to-flow landforms that can be found at the cross-shelf troughs are the GZWs, sedimentary depocenters formed at the grounding zone of marine-terminating ice sheets (R. D. Powell and Alley, 1997) that record the position of grounding zones in periods of still-stand ice sheet during deglaciations, and indicate episodic ice retreat in the trough (Batchelor et al., 2018). Beyond the cross-shelf troughs, if sediment delivery to the shelf edge over successive glacial periods is high enough, the prograding sedimentary depocenters termed trough-mouth fans are formed (J. A. Dowdeswell et al., 1996; J. A. Dowdeswell and Siegert, 1999; Elverhøi et al., 1998). On the upper continental slope of these depocenters, sediments are usually remobilised forming glacigenic debris flows, and the succession of depositions provides long-term records of sediment delivery and ice-stream dynamics (Cofaigh et al., 2003; J. A. Dowdeswell et al., 1996; J. A. Dowdeswell and Siegert, 1999; J. A. Dowdeswell et al., 2006; Vorren and Laberg, 1997).

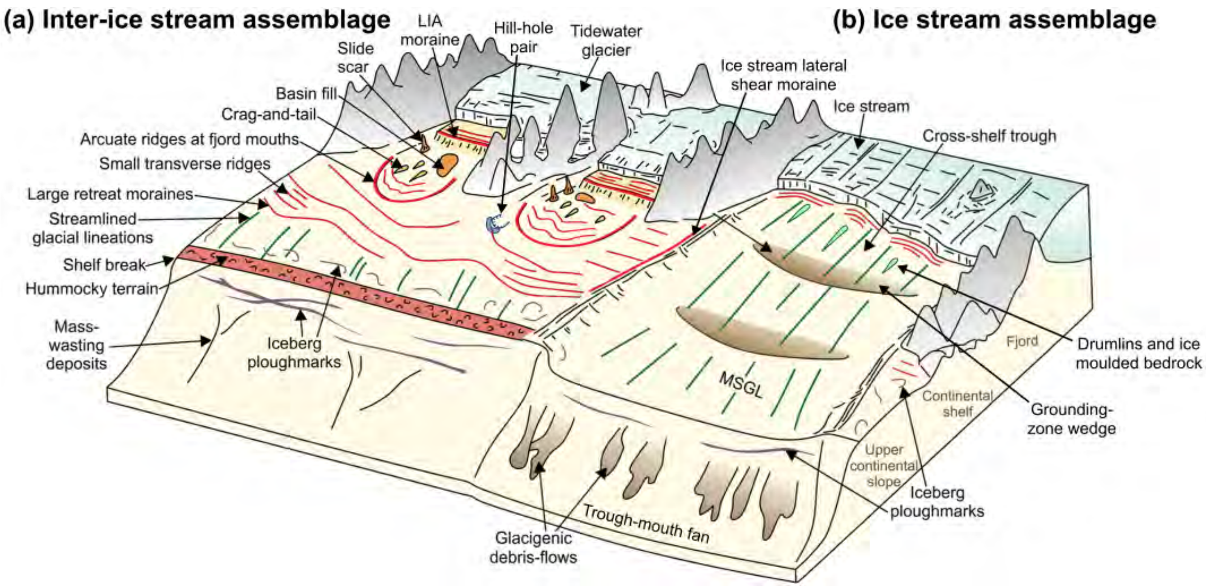


**Figure 3**. Sketches of (a) inter-ice stream banks and (b) cross-shelf troughs, showing the typical submarine glacial landforms that can be found on each assemblage. Modified from Dowdeswell et al., (2016b) and Ottesen and Dowdeswell (2009). LIA: Little Ice Age; MSGL: Mega-scale glacial lineations.

The inter-ice stream continental shelf is shallower and preserves glacial landforms characteristic of slow-flowing ice (Fig. 3a; Ottesen and Dowdeswell, 2009). Examples are moraines and hummocky-terrain belts, which are typically orientated transverse to ice-flow direction, indicating thus the relatively slow retreat of grounding ice across the continental shelf (J. Dowdeswell et al., 2008). In some inter-ice stream banks, landforms aligned with the ice flow can also be found, including hill-hole pairs and even crag-and-tails (Ottesen and Dowdeswell, 2009). In the boundary between fast- and slow-flowing ice we find the lateral shear-moraines (Stokes and Clark, 2002b).

Through calving events, the marine-terminating ice sheets lose mass in the form of icebergs, and when the keels of these enormous blocks of ice ground on the seafloor, they carve linear to curvilinear depressions called iceberg ploughmarks, scours, or furrows (J. A. Dowdeswell et al., 1993; Woodworth-Lynas et al., 1991). Sea-ice drifting can also plough similar features. Although iceberg ploughmarks can be found at the cross-shelf troughs, the inter-ice stream banks, and the upper continental slope (e.g. J. A. Dowdeswell et al., 1993; Woodworth-Lynas et al., 1991), they more commonly occur in the inter-ice stream banks due to a shallower seafloor there (Batchelor et al., 2018). At the same time, the icebergs, the sea ice, and the floating ice tongues can become sediment sources as they melt, spreading glacially-related sediments that might be partially redistributed by oceanic currents (D. A. Darby et al., 2009; Polyak et al., 2009).

Thus, the analysis of the cross-cutting relationships between submarine glacial landforms unveils the complexity of the ice sheet dynamics, implying shifts in sea level, climate regimes, and ice mass loss (J. A. Dowdeswell, Canals, et al., 2016b). A major focus is placed on the cross-shelf troughs, since the fast-flowing ice that is or used to be present in these regions responds dramatically to sub-decadal perturbations (Anandakrishnan and Alley, 1997; Joughin et al., 2003), and can potentially force abrupt climate change by ice and meltwater delivery to the ocean (C. D. Clark, 1994; MacAyeal, 1993). Moreover, these regions can serve as a robust test for past ice sheet modelling as the modelers will try to match the distribution of modelled past fast-flowing ice with the distribution of cross-shelf troughs (J. A. Dowdeswell, Canals, et al., 2016b).

Nevertheless, not all submarine landforms in the AO are formed by the action of the glaciers, even though they are still related in most cases. We can find landforms related to gravity flows such as slope failures (e.g. Boggild et al., 2020; Cherkis et al., 1999), submarine canyons (e.g. Garrison and Becker, 1976) and submarine channels (e.g. Boggild and Mosher, 2021), with currents (e.g. Boggild and Mosher, 2021; J. A. Dowdeswell and Ottesen, 2016), with gas and/or water venting (e.g. Chand et al., 2016; J. A. Dowdeswell and Todd, 2016; Jakobsson and O'Regan, 2016; P. R. Vogt et al., 1994), and with human and animal activity (e.g. Thorsnes et al., 2016).

## 2.5 Oceanographic setting

The vertical structures of the AO waters are largely determined by the oceanic circulation patterns, which are in turn driven by wind forcing and buoyancy changes from heat transfer, freshwater input, and water input from other oceans. Specifically for the AO, the water stratification (i.e. separation of water in buoyancy-stable layers of different properties) at the top few hundred meters of the water column is predominantly controlled by salinity differences, what is known as the Arctic halocline. Therefore, the AO waters are typically composed of three layers: a fresher cold surficial layer separated by a strong halocline from the underlain warmer salty layer of Atlantic origin, and a cold salty bottom layer.

The circulation of the surficial layer and the sea ice is dominated by the wind-driven Ekman transport, which is the net flow of the water at a 45° angle to the wind that induces the motion, as a result of the balance between Coriolis force and the fluid resistance. Thus, the closed clockwise Beaufort Gyre appears in the Amerasia Basin, and a counterclockwise circulation forms over the western Siberian continental shelf and the Nansen Basin influenced by currents coming from the North Atlantic and Nordic Seas (Rudels, 2019). The convergence of both currents forms the Transpolar Drift, which moves towards the Fram Strait with some water rejoining the Beaufort Gyre (Fig. 4a; Rudels and Carmack, 2022). Underneath the uppermost layer, poorly stratified waters move as a barotropic flow (its density is only dependent on the pressure) following depth contours (Nøst and Isachsen, 2003).

North Atlantic Waters that flow into the Nordic Seas and AO are continuously being transformed, changing their density, and returning to the Atlantic both as surficial currents or deep currents, that is why the AO is considered a global-scale double estuary (Carmack and Wassmann, 2006). These warm water masses first cross the Greenland-Scotland Ridge and continue northward as the Norwegian Atlantic Current, which starts to lose heat to the atmosphere and becomes denser enough to join the deep circulation (even if the current is still surficial). The current then split with a significant fraction entering the Barents Sea (Ingvaldsen et al., 2002; Schauer et al., 2002), and the other continuing to the Fram Strait as the West Spitsbergen Current, which in turn splits again, half of it entering the AO and the other half turning around and joining the East Greenland Current that moves southward (Fig. 4; Rudels, 1987). The former continues with the atmospheric cooling since it does not face sea ice until it reaches northeastern Barents Sea, meaning less freshwater input that allows it to remain dense enough to join the deep circulation (Rudels and Carmack, 2022). The currents that successfully cross the Fram Strait, meet sea ice north of Svalbard and start losing heat also by melting the ice, so the upper layer becomes much lighter and shifts to the surficial circulation (Fig. 4a), while the deeper layer forms a boundary current that moves eastward along the Eurasian slope (Fig. 4b; Rudels and Carmack, 2022).

The denser waters of the Barents Sea inflow branch intrude below the boundary current at the St. Anna Trough, whereas the less dense ones mix with the most surficial boundary current, thus forming another boundary current that moves beside but inshore of the Fram Strait branch (Fig. 4b; Rudels, 2019; Rudels and Carmack, 2022). At the north of Severnaya Zemlya, a narrowing of the continental slope causes the inshore boundary current to move downslope and mix isopycnally with the warmer boundary current coming from the Fram Strait (Rudels, 2019; Rudels and Carmack, 2022). This results in a cooling and freshening of the Fram Strait branch. The boundary current continues counterclockwise along the continental slope of the AO cooling gradually until reaching the Fram Strait again. When it encounters major bathymetric features (Gakkel Ridge, Lomonosov Ridge, Alpha-Mendeleev Ridge, and Chukchi Plateau), part of the flow enters the deep basins (Nansen, Amundsen, Makarov, and Canada basins respectively)

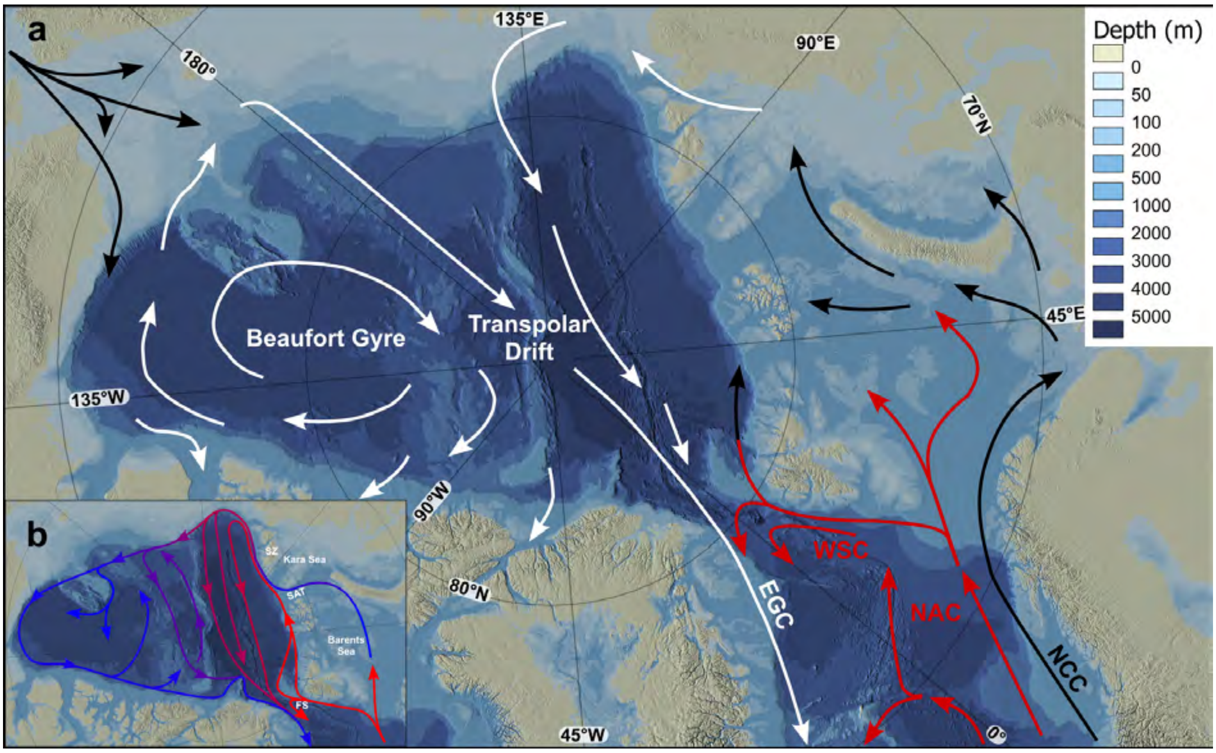


**Figure 4**. Schematics of the water circulation in the AO and the Greenland and Norwegian seas. (a) Circulation of the upper layers with red arrows indicating the flow direction of warm Atlantic currents, white arrows indicating the flow direction of cold and less saline Arctic currents, and black arrows indicating the flow direction of low salinity transformed currents. Based on Rudels et al. (2012). EGC: East Greenland Current; NAC: Norwegian Atlantic Current; NCC: Norwegian Coastal Current; WSC: West Spitsbergen Current. (b) Circulation of sub-surficial and intermediate waters with arrows indicating the direction of the currents. The colour of the arrows symbolises the temperature of the currents, ranging from relatively warm waters (red) to cold waters (blue). Based on Rudels (2019). FS: Fram Strait; SAT: St. Anna Trough; SZ: Severnaya Zemlya.

forming gyres that eventually rejoin the main loop (Fig. 4b; Rudels and Carmack, 2022). In the eastern Laptev Sea, a low salinity current coming from the Norwegian Coastal Current through the Barents-Kara Sea that incorporated runoff from large Siberian rivers crosses the shelf break and forms an intermediate water mass above the Amundsen Basin gyre. At the Canada Basin, the intermediate water is formed mainly due to the low salinity barotropic inflow from the Pacific Ocean (Haine et al., 2015; Woodgate et al., 2010).

The AO waters either leave through the Canadian Arctic Archipelago (Leblond, 1980; Münchow et al., 2006) or the Fram Strait in the East Greenland Current (Woodgate et al., 1999). This way, in periods of weakened Beaufort Gyre and expanded counterclockwise upper circulation in the Eurasia Basin, part of the Pacific inflow exits the AO through the Fram Strait, which otherwise stays in the Amerasia Basin (Steele et al., 2004) or exit through the Canadian Arctic Archipelago (Rudels and Carmack, 2022). Crossing the Fram strait, waters transformed in the AO mix with recirculating Atlantic waters and with central Greenland and Iceland Seas, until they are capable of crossing the Greenland-Scotland Ridge superficially as the East Greenland Current, or deeply as dense overflows (Rudels and Carmack, 2022).

The starting of an AO with "modern" conditions was set, depending on the age models, to 17.5 Ma (Backman et al., 2008; Jakobsson, Backman, Rudels, et al., 2007; Stein et al., 2006) or 38 Ma (Poirier and Hillaire-Marcel, 2009), but in either way, it was related to a shift from euxinic to ventilated open marine conditions (Jakobsson, Backman, Rudels, et al., 2007; Stein et al., 2006), caused by the two-way water exchange through the recently opened Fram Strait (Jakobsson, Backman, Rudels, et al., 2007). Then, during the Quaternary glacial periods, the lowered sea level exposed the continental shelves of the AO, which were moreover partially covered by ice sheets, thus limiting the circulation within and the water exchange with its surroundings (Polyak et al., 2004). The complexity of the system challenges making predictions on how changes in the system will affect the circulation in the AO. In general, a warmer climate would likely cause a weakening of the double-estuary circulation if we consider: 1) an increased isolation between the upper and intermediate layer that would cause a decrease in the pulling effect that the boundary current has on the upper layers, thus weakening superficial circulation, 2) the increase in freshwater input due to melting that would prevent deep water formation (Rudels and Carmack, 2022). Changes in AO circulation threaten global thermohaline circulation by modifying water exchange with the Atlantic and Pacific, potentially impacting global climate (Delworth et al., 1997).

The sea ice extent is also critical for the global climate, affecting the planetary albedo and the exchange of heat, moisture, and gases between the sea ice and both the ocean and atmosphere (Smith et al., 2003). This way, sea ice influences and is influenced by ocean circulation, and if the decline of perennial sea ice cover (Cavalieri and Parkinson, 2012) and thickness (Kwok, 2018) produced during the past decades continues, changes in AO water temperature, salinity, stratification, and dynamics are to be expected (Timmermans and Marshall, 2020).

# 3 Research Area

This study covers part of the Eurasia Basin of the AO, and part of the Fram Strait, Greenland Sea and Norwegian Sea. More in detail, it covers: some areas of the southern Lomonosov Ridge, some of the Morris Jesup Spur, and some of the region between these two features; the Voronov Terrace, the southwestern Gakkel Ridge, the western Nansen Basin, and the Lena Trough and part of its surroundings; the Yermak Plateau and the Sophia Basin; the western Svalbard continental shelf and slope and its southern continuation; the region between Svalbard and Greenland continental shelves, including the Spitsbergen Fracture Zone, Molloy Ridge, Molloy Fracture Zone, Greenland-Spitsbergen Sill, Hovgaard Ridge, north of Knipovich Ridge, Boreas Abyssal Plain, East Greenland Ridge, and part of the Greenland Abyssal Plain; and the Belgica Bank and Norske Trough of the eastern Greenland shelf, including the adjacent slope (Fig. 5). The area at the west of the Lena Trough is included in the surface geology map presented but will not be described and discussed in this thesis because the polygons were digitalized externally by Kai Boggild, and I do not possess the sub-bottom profiles.

The area of the southern Lomonosov Ridge has a crest ranging between depths of 600 and 1000 m deep with a gentle slope. There, above a water depth of 785 m, ice erosion has been previously identified using sub-bottom profiles and multibeam acquired with *IB Oden*. However, the relatively poor quality of the multibeam data, due to sever sea-ice conditions, prevented further interpretation of the seafloor morphology that in other places of the central AO have provided information on ice masses that caused the erosion (Jakobsson et al., 2010). Similarly, traces of ice grounding were identified at the northeastern part of the Morris Jesup Spur (Spielhagen et al., 2004), however, in this case, multibeam data acquired afterward facilitated a precise description of the area and suggested icebergs flowing south-eastward as the responsible of these landforms (Jakobsson et al., 2010). These iceberg ploughmarks were found as deep as 1045 m (Jakobsson et al., 2010). Our map also covers a small relatively flat area at the southwestern part of the Morris Jesup Spur that is around 700 m deep, and the region at its west, which covers a smaller extension of the Greenland shelf also at depths around 700 m and the region that goes downslope until reaching the Amundsen Basin at depths of 3300 m.

The Voronov Terrace is located between the southernmost Gakkel Ridge and the eastern Morris Jesup Spur, and is connected to the Amundsen Basin along its northernmost border. Its depth varies around 3900 m with outcrops from the Gakkel Ridge that can be shallower than 2300 m. This study covers the westernmost part of the Gakkel Ridge as well as the west-central part only from the axis of the ridge to the Nansen Basin. The area of the Nansen Basin covered is the one contiguous to the covered Gakkel Ridge. The Lena Trough is the western continuation of the Gakkel Ridge, thus showing similar physiography perhaps with less pronounced and more separated crests than the adjacent section of the Gakkel Ridge. The rugose axis of this trough varies from $\sim$4700 m deep at the northern part to $\sim$4100 m at the southern part. No

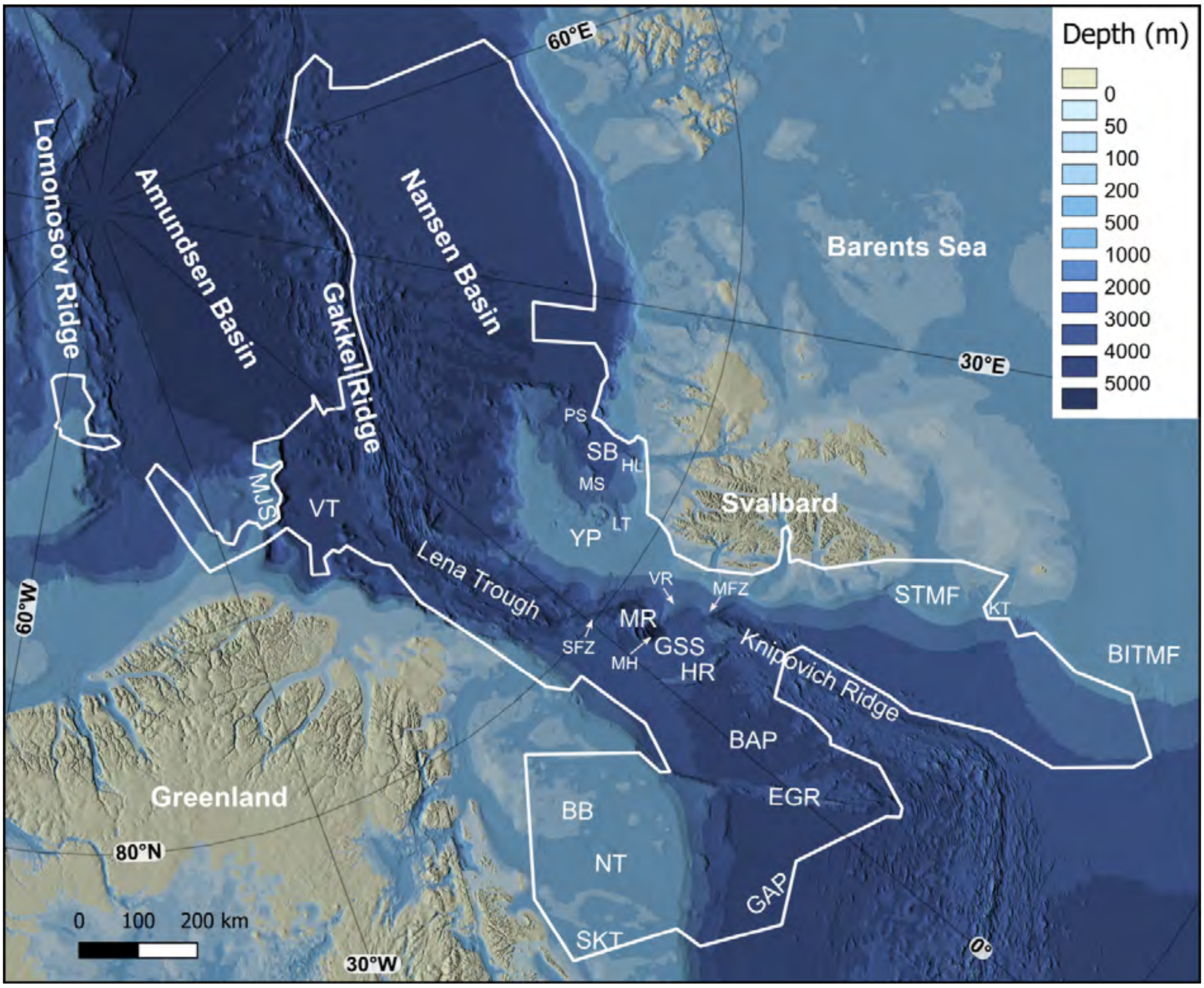


**Figure 5**. Map of the research area of this study showing the main physiographic features. The research area is represented by the transparent polygons with white borders. BAP: Boreas Abyssal Plain; BB: Belgica Bank; BITMF: Bear Island Trough-Mouth Fan; EGR: East Greenland Ridge; GAP: Greenland Abyssal Plain; GSS: Greenland-Spitsbergen Sill; HL: Hinlopen Landslide; HR: Hovgaard Ridge; KT: Kveithola Trough; LT: Litke Trough; MJS: Morris Jesup Spur; MFZ: Molloy Fracture Zone; MH: Molloy Hole; MR: Molloy Ridge; MS: Mosby Seamount; NT: Norske Trough; PS: Polarstern Seamount; SB: Sophia Basin; SFZ: Spitsbergen Fracture Zone; SKT: Store Koldewey Trough; STMF: Storfjorden Trough-Mouth Fan; VR: Vestnessa Ridge; VT: Voronov Terrace; YP: Yermak Plateau

further than 110 km to the west from the axis we find the northeastern Greenland continental shelf and 90 km to the east the Yermak Plateau. The Fram Strait is the only deep gateway of the AO, so the seafloor around this region (which includes the Lena Trough, Yermak Plateau, and northwestern Svalbard and northeastern Greenland margins and the seafloor between them) is largely influenced by the water exchange between the AO and the North Atlantic (Fig. 4). The Fram Strait was a result of the separation between Greenland and Svalbard through seafloor spreading starting in the late Mesozoic to early Cenozoic (Ehlers and Jokat, 2009; Geissler et al., 2011; Läderach et al., 2011; Sundvor and Eldholm, 1979).

On the Yermak Plateau, many traces of ice grounding can be found. Linear elongated ridges are mainly identified on the southern ridge crest of the plateau shallower than 600 m and at the northwestern Yermak Plateau between depths of 725-850 m (Batchelor et al., 2016; J. A. Dowdeswell et al., 2010; Gebhardt et al., 2011; Jakobsson et al., 2010). Possible interpretations are grounding ice from the Svalbard Barents Sea Ice Sheet, from the remnants of an Arctic ice shelf, or from the keels of icebergs trapped within sea ice, capable of ploughing the seafloor in a uniform pattern (J. A. Dowdeswell et al., 2010; Gebhardt et al., 2011). Then linear to curvilinear depressions of two types were identified, wide parallel to sub-parallel probably caused by icebergs packed within sea ice (J. A. Dowdeswell et al., 2010; Jakobsson et al., 2010), and narrow irregular caused by isolated icebergs (J. A. Dowdeswell et al., 2010; Gebhardt et al., 2011; P. R. Vogt et al., 1994). At the southeastern part, we can find a 2 km curved moat around the southeast basement high of the plateau, interpreted as an overflow channel likely formed by the West Spitsbergen Current (Fig. 4) that crosses the southern ridge of the plateau (J. A. Dowdeswell et al., 2010; P. R. Vogt et al., 1994). Thus, also considering sediment cores and seismic and sub-bottom profiles, three major events were suggested to shape the plateau (Batchelor et al., 2016): ice-sheet grounding during MIS 19/20 (J. A. Dowdeswell et al., 2010; Gebhardt et al., 2011), grounding of an ice shelf or icebergs likely during MIS 6 (J. A. Dowdeswell et al., 2010; Jakobsson et al., 2010), and isolated iceberg groundings during late Pleistocene (J. A. Dowdeswell et al., 2010; P. R. Vogt et al., 1994). However, recent studies of AO age models established for sediment cores question the assigned age of MIS 6 for the key unit associated with ice-shelf grounding; it may in fact be older (Razmjooei et al., 2023). Despite this, this study will stick to the previous age models as they are used by all referenced studies here, and the dating of the AO sediments is now subjected to continuous review. The Sophia Basin, surrounded by the east flank of the plateau, the northern Svalbard margin, and the southeastern Nansen Basin, ranges from about 1100 m deep at its mouth to deeper than 3100 m at its connection with the Nansen Basin. The Litke Trough connects the southeastern Yermak Plateau with the Sophia Basin (Fig. 5). Part of the West Spitsbergen Current flows directly above the trough (Manley et al., 1992), which probably has an impact on the sediment dynamics there (Fig. 4). Two seamounts are located in the Sophia Basin, the almost 1000 m high Mosby Seamount at the southwest, and the $\sim$1460 m high Polarstern Seamount at the northeast (Fig. 5). The Hinlopen landslide, of which scar is located at the northern Svalbard shelf edge, also affected the seabed morphology of this trough by delivering a large quantity of debris and block, with an estimated volume of 1250 - 1350 km$^3$ (Vanneste et al., 2006; Winkelmann et al., 2008).

On the western margin of Svalbard and Barents Sea, all kinds of submarine glacial landforms have been described, including cross-shelf troughs (e.g. Batchelor and Dowdeswell, 2014; Bjarnadóttir et al., 2013; Ottesen et al., 2007), trough-mouth fans (e.g. Lucchi et al., 2013; Pedrosa et al., 2011; Vorren et al., 1998), GZWs (e.g. Forwick and Vorren, 2010; Ottesen et al., 2007; Rebesco et al., 2011), MSGLs (e.g. Andreassen et al., 2007; Ottesen et al., 2007), drumlins (e.g. Bjarnadóttir et al., 2013) and moraine ridges and hummocky terrains (e.g. J. A. Dowdeswell, Ottesen, and Rise, 2016). All these landforms were formed as a result of the advancing and retreat of the Svalbard-Basents Sea Ice Sheet, both at cross-shelf troughs and inter-stream banks, and the last time this ice sheet reached the shelf edge causing upper slope instabilities was 24 ka (Andersen et al., 1996; Elverhøi et al., 1995; Jessen et al., 2010). Other widespread landforms in this area are the iceberg ploughmarks, suggested to be formed during MIS 2 and MIS 6 by giant icebergs from the AO that crossed the Fram Strait and then recirculated in the Norwegian-Greenland Sea ploughing western Svalbard margin, and during MIS 2 by smaller icebergs coming from west Barents Sea ice streams (Zhao et al., 2017).

Moving to the central part of the Fram Strait we find the Hovgaard Ridge, the shallowest obstacle in this region approximately 130 km long, 20 km wide at its widest part, and NW-SE-orientated. Its summit is $\sim$1170 m deep and here some of the deepest iceberg ploughmarks were identified. Six N-S-orientated depressions at about 1200 m deep, probably caused by giant icebergs coming from the AO in a north-to-south direction (Arndt and Forwick, 2016; Arndt et al., 2014), hypothesis that supports the origin of the iceberg ploughmarks on the western Svalbard margin (Zhao et al., 2017). At the north of the Hovgaard Ridge, the Greenland-Spitsbergen sill lies at depths between 2300 and 2700 m. North and east of this sill we find the spreading ridges that continuate the Lena trough southward. The Molloy Ridge is connected to the southern Lena Trough through the Spitsbergen Fracture Zone and connected to the northern Knipovich Ridge through the Molloy Fracture Zone. The intersection between the Molloy Ridge and Fracture Zone creates a deep nodal basin (Fournier et al., 2008) called Molloy Hole (Fig. 5; Thiede et al., 1990), the deepest point of the IHO-defined AO ((IHO), 2002) arriving at depths of 5560 m.

The Boreas Abyssal Plain, bounded by the Hovgaard Ridge at its North, the Knipovich Ridge at its east, the East Greenland Ridge at its south, and the Greenland continental shelf at its east, is a rather flat basin at depths ranging from 3000 to 3200 m that accommodate a few relatively small outcrops from the spreading ridge. The East Greenland Ridge is an elongated continental sliver NW-SE-oriented, with an average depth of 2000 m, 250 km long, and 30 km wide (Døssing et al., 2008). Its steep southern flank ends at the Greenland Abyssal Plain at around 3700 m. Its northwestern part is connected to the eastern Greenland shelf by a prominent spur.

The part of the Greenland continental shelf that this study covers is the eastern/northeastern, a region with one of the widest continental shelves in Greenland, extending more than 330 km offshore. Specifically, from south to north, it covers part of the Store Koldewey Trough, Norske Trough, and the inter-ice stream shelf Belgica Bank. Although the northeastern Greenland shelf is sparsely mapped due to sea ice conditions there, many different glacial landforms have already been identified. Glacial lineations, GZWs, moraines, and iceberg ploughmarks were identified on the Store Koldewey Trough (Laberg et al., 2017; Olsen et al., 2020), and on the Norske Trough (Arndt et al., 2015, 2017; López-Quirós et al., 2024). The Norske Trough margin has been subjected to mass-wasting processes, with scars and divergent channel-like depressions on the upper slope, stacked debris flow lobes below, and a turbidite system arriving at the Greenland Abyssal Plain (García et al., 2016; García et al., 2012). The Belgica Bank seafloor has an undulating irregular physiography as a result of active salt diapirism (Arndt et al., 2015; Hamann et al., 2005), where glacial lineations, moraines, iceberg ploughmarks, and elongated depressions caused by the interaction between ice-marginal processes and current-related erosion, can be found (Arndt et al., 2015, 2017).

# 4 Acoustic Facies

Damuth (1975, 1978, 1980) started to subdivide different seafloor provinces according to the appearance of bottom echoes and sub-bottom reflections on sub-bottom profiles. Following the same principle, I classify sub-bottom profiler data from the AO and the Fram Strait according to the character of the bottom echo and sub-bottom reflections, and adopting Boggild et al., (2018) acoustic facies classification scheme that was used for characterization of the Amerasia and Amundsen basins. This subdivides the data into acoustic facies (Table 1) and compound facies (Table 2). The former is the distinct types of single facies while the latter comprises an aggregation of two or more single facies. The acoustic facies are grouped into three categories corresponding to: 1) chaotic or irregular seafloor, 2) smooth seafloor with acoustically transparent sub-bottom, 3) laminated sub-bottom reflections. The compound facies emphasize which is the most surficial acoustic facies while making stratigraphic relationships with the acoustic facies that are found underneath. Thus, the compound facies reflect changes in the processes that were present in the region having an impact on the seafloor and sub-bottom. For this study, the addition of a few more types of compound facies that were not defined by Boggild et al. (2018) was needed. These facies are presented in Table 4 (Section 6). Note that the compound facies presented in Table 2 and 4 are only those that were translated to polygons, meaning that more compound facies types were identified in the sub-bottom profiles, but their appearance was not consistent enough for creating a polygon. All facies identified can be found at Appendix I.

**Table 1.** List of the principal acoustic facies, their description, and the generalised geologic interpretation depending on the area they are found, adapted from Boggild et al. (2018). Each facie type has a colour that will be used afterwards for the mapping. An example of each facie type is shown.

Principal Facies

| Category | Name | Example | Description | Generalized Geologic Interpretation |
|---|---|---|---|---|
| Chaotic / Irregular Seafloor | 1a | 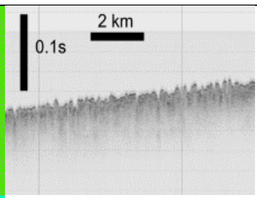 | Chaotic bottom echo with amorphous or transparent sub-bottom reflections. | **Shelf:** Ice-scoured / turbated sediment or till<br>**Shelf break:** Slump / mass transport deposit (MTD)<br>**Slope / Ayssal Plain:** MTD |
| | 2a* | 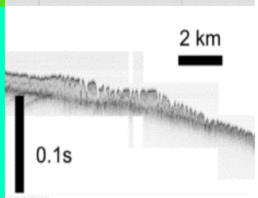 | Scoured bottom echo with amorphous or transparent sub-bottom and semi-parallel incoherent reflections. | **Shelf / Shelf Break:** Ice-scoured sediment with turbated upper layer |
| | 2b* | 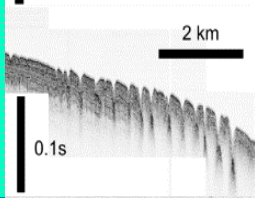 | Semi-parallel coherent reflections interrupted by troughs at the seafloor surface. | **Shelf / Shelf Break:** Ice-scoured bedded sediments with minimal or no turbation |
| | 3a | 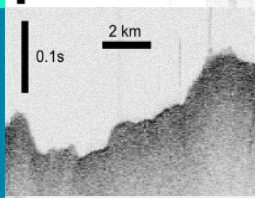 | High amplitude, irregular bottom echo with amorphous sub-bottom reflections. | **Shelf:** Eroded surface or till<br>**Slope:** Eroded surface, exposed bedrock, MTD or channel thalweg<br>**Ayssal Plain:** Exposed bedrock (seamount), channel thalweg |
| | 3b | 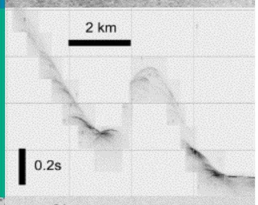 | Varying amplitude, broad or one-sided hyperbolic bottom echo with no sub-bottom reflections. Occur on steep bathymetric gradients. Hyperbolae 1-2 km in width. | Fault / mass failure scarp or basement structure |
| | 4a | 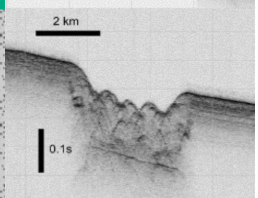 | Chaotic bottom echo with amorphous or transparent sub-bottom reflections. | **Shelf / Shelf Break:** Ice-scoured sediment or slump<br>**Slope:** Slump / MTD<br>**Ayssal Plain:** MTD |
| | 4b | 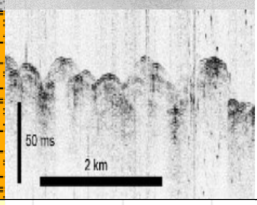 | Narrow hyperbolic to irregular reflections with semi-coherent sub-bottom reflections in the uppermost 20-50 ms that maintain a consistent amplitude profile laterally. | Slump crown cracks within stratified (e.g., hemipelagic drape) or hemipelagic drape burying complex topography of buried MTD |
| Smooth Seafloor/ Transparent | 5a | 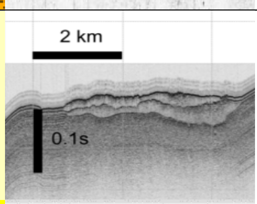 | Smooth bottom echo with incoherent transparent lens-shaped deposit(s). | **Shelf:** Diamict (often till from glacier retreat phase), or MTD<br>**Slope:** Debris flow, MTD |
| | 6a | 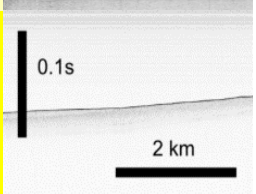 | High amplitude, smooth bottom echo with acoustically transparent sub-bottom. | **Shelf:** Undisturbed deglacial and post-glacial deposits<br>**Slope:** Channel lag deposits part of MTD |

| Category | Name | Example | Description | Generalized Geologic Interpretation |
|---|---|---|---|---|
| Coherent sub-bottom reflection = Bedded / Laminated | 7a | 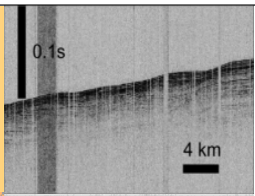 | Smooth undulating, coherent parallel to subparallel reflections. Reflections pinch out, diverge, or vary in amplitude laterally. | **Shelf Break:** Current-influenced glaciomarine and post-glacial deposits **Slope:** Mixed turbidites / hemipelagites, contourites, fan deposits **Ayssal Plain:** Undulating turbidites or contourites |
| | 7b | 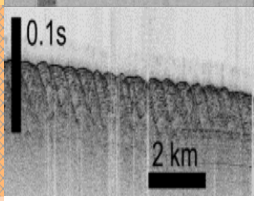 | Smooth, wavy coherent parallel to subparallel reflections with sediment waves. Sediment waves defined by dipping planes of pinching reflections. | **Slope:** Fan sediments, levee sediments related to deep-sea channels |
| | 7c* | 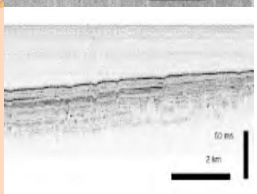 | Smooth undulating, coherent parallel stratified reflections with down-section transition to acoustically blank / chaotic reflectivity. Some narrow blanked zones as well. | **Shelf** / **Shelf Break:** Permafrost sediments, glacimarine sediments with buried syn-sedimentary ice scours, or gas if complete blanking |
| | 7d | 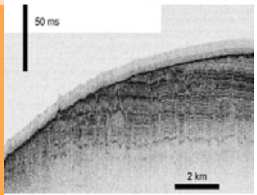 | High amplitude smooth bottom echo truncating coherent, semi parallel sub-bottom reflections. May experience blanking at depth. | **Shelf:** Eroded glacimarine / periglacial or Holocene sediments. Blanking due to gas, buried margin wedges, buried ice scours |
| | 7e | 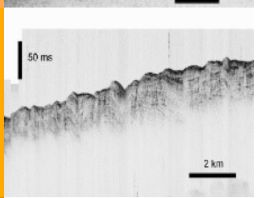 | Rugose bottom echo with semi-coherent contorted parallel/subparallel and amorphous sub-bottom reflections. | **Slope:** Deformed sediments, MTD, or fan deposits with small-scale sediment waves |
| | 7f | 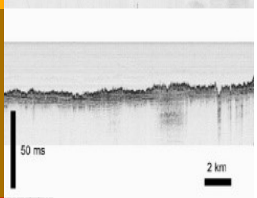 | Chaotic bottom echo truncating coherent semi-parallel reflections. | **Shelf:** Eroded preglacial / glacimarine sediments |
| | 8a | 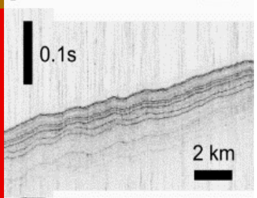 | Smooth bottom echo with coherent parallel to sub-parallel reflections that mimic bathymetry. Sub-bottom reflections maintain a consistent amplitude laterally. | **Shelf:** Laminated glaciomarine / Holocene hemipelagic drape deposits **Slope:** Hemipelagic drape, mixed fan sediments |
| | 8a | 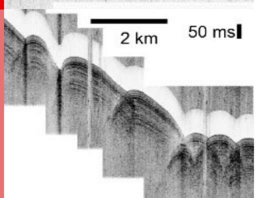 | Smooth bottom echo with coherent parallel to sub-parallel reflections that mimic bathymetry. Sub-bottom reflections maintain a consistent amplitude laterally. Seafloor forms broad hyperbolae of 1 - 2 km in width. | **Slope:** hemipelagic sediments over 'pitted' slope |
| | 9a | 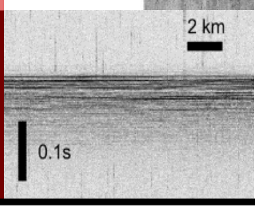 | Smooth, flat-lying, coherent parallel reflections. Reflections typically onlap neighbouring facies or structural highs. Reflections may thicken towards depocenter. | **Ayssal Plain:** Flat-lying turbidites and interbedded hemipelagites |

* Facies types that were not grouped into polygons.

**Table 2.** List of the compound facies described by Boggild et al. (2018) that were used in this mapping, their description, and the generalised geologic interpretation depending on the area they are found. Each compound facie type has a colour that will be used afterwards for the mapping. An example of each compound facie is shown.

## Compound Facies

| Category | Name | Example | Description | Generalized Geologic Interpretation |
|---|---|---|---|---|
| Chaotic / Irregular Seafloor | 1a over 1a | 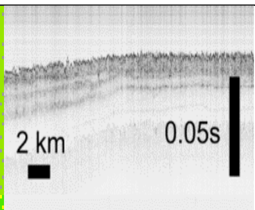 | Chaotic bottom echo with amorphous / transparent sub-bottom reflections overlying chaotic sub-bottom reflections. | **Shelf:** Stacked ice-scoured / till deposits / till tongues |
| | 1a over 6a | 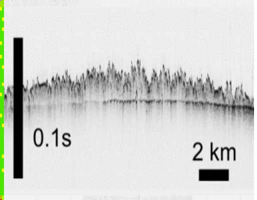 | Chaotic bottom echo with amorphous/transparent sub-bottom reflections overlying high amplitude smooth echo with amorphous/transparent sub-bottom. | **Shelf:** Ice-scoured sediment, till and / or glacimarine iceberg turbate |
| | 1a truncating 8a | 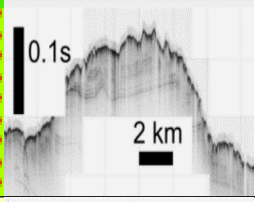 | Chaotic bottom echo with acoustically transparent sub-bottom truncint coherent, parallel to semi-parallel stratified reflections. | **Shelf:** Ice-scoured sediment / diamict unconformably overlying older stratified sediments |
| Smooth Seafloor/ Transparent | 5a interbedded with / over 7a | 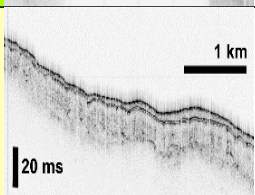 | Smooth bottom echo with incoherent transparent wedge deposits overlying sub-parallel sub-bottom reflections / semi-coherent contorted subparallel and amorphous sub-bottom reflections. | **Slope / Abyssal Plain:** MTD interbedded with / over turbidites |
| | 5a interbedded with / over 8a | 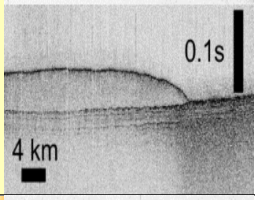 | Smooth bottom echo with incoherent transparent wedge deposits interbedded with coherent parallel/sub-parallel sub-bottom reflections. | Debris flow / MTD / diamict over stratified sediment (e.g. hemipelagic / turbidites / glacimarine) |
| Coherent sub-bottom reflection = Bedded / Laminated | 7a interbedded with / over 5a | 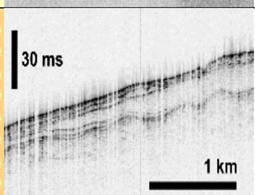 | Smooth undulating, coherent parallel to subparallel reflections interbedded with transparent wedge-shaped deposits. | **Shelf Break:** Current-influenced glaciomarine and post-glacial deposits interbedded with / over MTDs<br>**Slope / Abyssal Plain:** Turbidites interbedded with / over MTDs |
| | 8a over 1a | 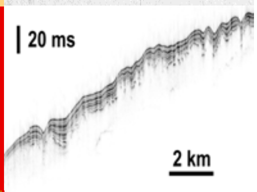 | Rugose seafloor echo underpinned by veneer of stratified reflections that mimic seafloor morphology, overlain on chaotic reflection with no discernible deeper reflections. | **Shelf / Submarine Elevations:** Hemipelagic drape overlying diamict |
| | 8a over 1a truncating 8a | 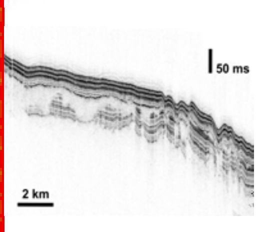 | Rugose seafloor echo underpinned by veneer of stratified reflections that mimic seafloor morphology, overlain on chaotic reflection with acoustically transparent sub-bottom. This transparent unit subsequently truncates stratified coherent reflections at depth. | **Shelf / Submarine Elevations:** Hemipelagic drape overlying diamict that in turn truncates underlying hemipelagic sediments |
| | 8a over 3a | 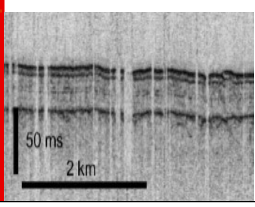 | High amplitude, smooth bottom echo with acoustically transparent sub-bottom. | **Shelf / Submarine Elevations:** Hemipelagic drape overlying MTDs - basal reflection of MTD is beyond penetration depth |

| Category | Name | Example | Description | Generalized Geologic Interpretation |
| --- | --- | --- | --- | --- |
| Coherent sub-bottom reflection = Bedded / Laminated | 8a interbedded with / over 5a | 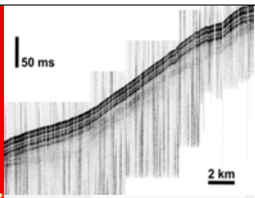  | Smooth bottom echo with draping coherent sub-bottom reflections interbedded with transparent wedge-shaped deposits. | **Slope:** Hemipelagic drape interbedded with MTDs / debris flows |
| | 8a over 5a truncating 8a | 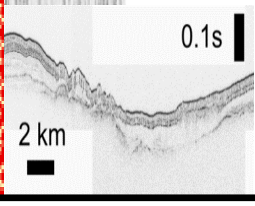  | Smooth bottom echo with draping coherent sub-bottom reflections overlain on transparent wedge-shaped deposits. This transparent unit subsequently truncates stratified coherent reflections at depth. | **Slope:** Hemipelagic drape interbedded with erosive MTDs / debris flow |

# 5 Methods

## 5.1 Data acquisition

All the data used in this project was acquired with sub-bottom profilers (SBPs). These systems are echo sounders used to explore the uppermost sediment layers below the seafloor, which typically operate with lower frequencies (1-20 kHz) than conventional single-beam echo sounders. The operating principle is the transmission of an acoustic pulse vertically down from a transducer that get reflected at any boundary with a strong enough acoustic impedance contrast. The sound pulse reflected is received by the same or another transducer, recording thus the two-way travel time (TWT), which is the time spent from the transmission until the reception of the sound pulse. Since lower frequencies attenuate less than higher, and long sound pulses contain more energy, SBPs are able to penetrate the seabed, and the pulses continue down until all their energy is absorbed. The result are echograms that stack the intensity of each received ping (sound pulse sent) one after the other, with often the TWT in the y-axis (Fig. 6). Thus, continuous profiles (as the vessel moves forward) that symbolize boundaries with strong impedance contrast are created, giving an idea of how the seafloor and the sub-bottom look.

Although expeditions based on *IB Oden* as the scientific platform are the principal data source for this project, data acquired with the Canadian *CCGS Louis S. St-Laurent*, the American *USCGC Healy*, and the German *RV Polarstern* were also used. The data acquired with *RV Polarstern* and *CCGS Louis S. St-Laurent* was managed and transformed into polygons by Kai Boggild. In Table 3 are listed the relevant expeditions for this study. All these vessels have different SBP systems installed.

*IB Oden* is equipped with a Kongsberg SBP120 (3°x3°), which is a SBP integrated with the EM120 multibeam echo sounder. It works with its own 8 m long and 1 m wide transmit transducer array, and shares an 8 m long and 1 m wide broadband receive transducer array with EM120. The normal transmit waveform is a chirp signal, which is a frequency-modulated (FM) pulse that, in this case, sweeps from 2.5 to 7 kHz. The FM pulse is compressed using matched filtering (Schock et al., 1989), so from an originally long pulse with a relatively low peak amplitude, it produces a narrow pulse with a high peak amplitude (Jakobsson, Gyllencreutz, et al., 2016). Thus, the penetration and resolution are maximized, and noise does not correlate with the filter, resulting in a higher signal-to-noise ratio (Jakobsson, Gyllencreutz, et al., 2016). The acoustic beams can penetrate up to nearly 100 m in moderate ice conditions, with an approximate maximum vertical resolution of 0.3 ms. The horizontal resolution is dependent on sampling density, the insonified area, and the mode of bottom detection (Jakobsson, Backman, Anderson, and Björk, 2007). Sampling density is in turn dependent on the transmission method, ping rate and vessel speed. With this system, the insonified area is stipulated by the first Fresnel zone above 440 m water depth, and by the beam footprint below that depth. The first Fresnel zone depends on the frequency of the beams and the water depth, while the beam

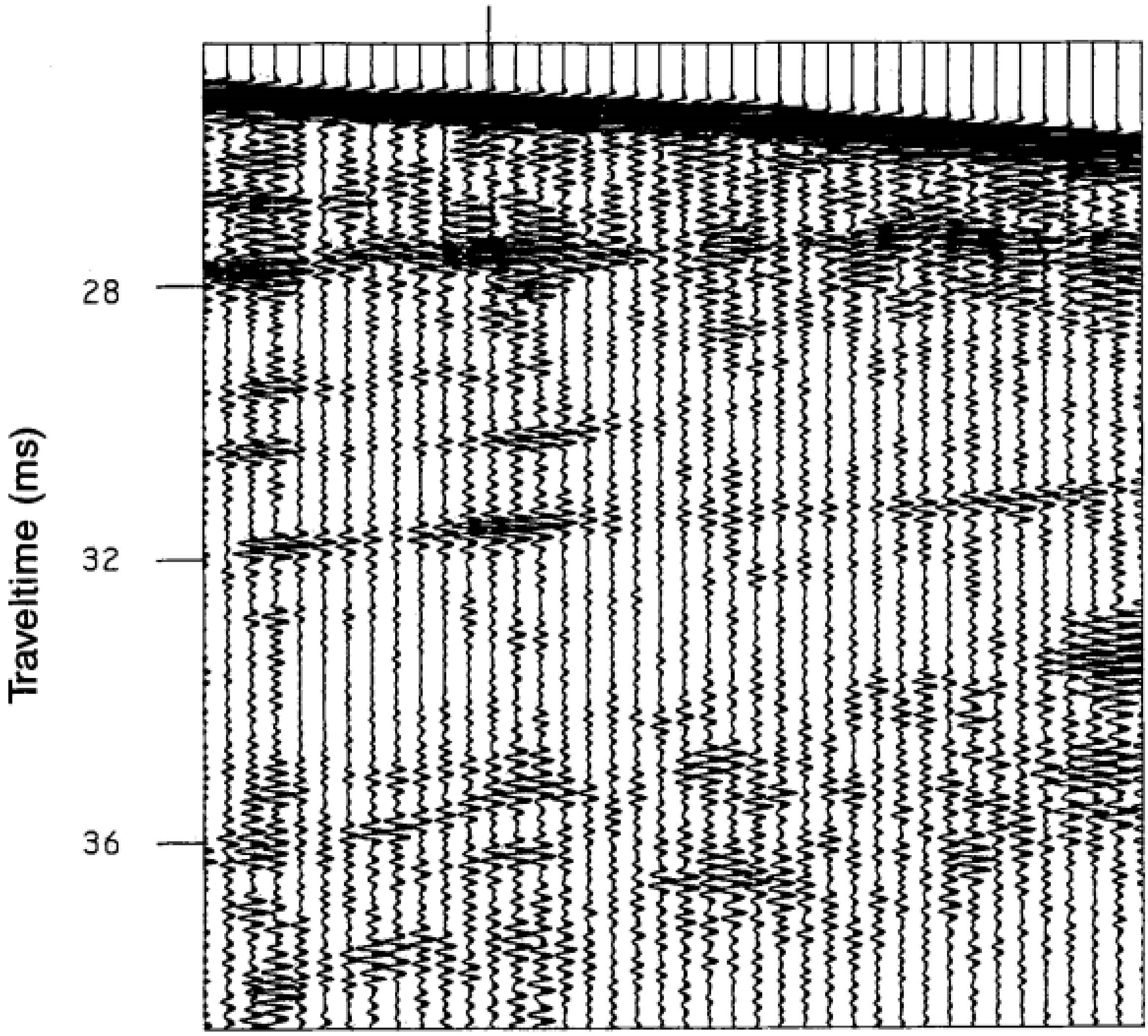


**Figure 6**. Example of an echogram, in this case a section from a chirp sub-bottom profile of the west passage of Narragansett Bay, Rhode Island, from Schock et al. (1989). Here, individual pings can be discerned (each horizontal line that changes in amplitude when trespassing boundaries with strong enough impedance contrast). Higher travel time means that the sound waves are reflected later, representing greater depths. The plotting of the traces one after another along the ship's track gives the spatial continuity. The black stripe at the top represents the seafloor, the strongest impedance contrast in this profile.

footprint depends on the angle of opening (3° in this system) and depth. Thus, for a water depth of 100 m, the first Fresnel zone diameter would be about 11 m, and for a water depth of 1000 m, the beam footprint would have a diameter of about 52 m.

Other possible transmit modes are the continuous wave pulses, hyperbolic chirps, and Ricker pulses (Jakobsson, Marcussen, and Party, 2008). This system can operate with 11 across-track beams with a 3° beam width and a spacing of usually 3°; it is also compensated for roll, pitch, and heave using the Seatex Seapath 320 navigational system with a MRU 5 motion sensor.

In *CCGS Louis S. St-Laurent*, a Knudsen 3260 Chirp system sweeping from 2.3 to 5.3 kHz is installed (Mosher et al., 2018). *USCGC Healy* had, during the HOTRAX´05, a Knudsen 320B/R dual frequency echo sounder installed, meaning that it can work at ~3.5 and 12 kHz. Chirp signals can be created at both frequency channels, but in that expedition, only the lower frequency channel, sweeping from 3 to 6 kHz, was used (D. Darby et al., 2005). *RV Polarstern* has a Parasound echo sounder, a parametric system that works in a frequency range of 2.5-5 kHz with a beam angle of opening of 4° and a footprint of 7 % of the water depth (Fütterer, 1992). A parametric system is characterized by the transmission of two primary high-frequency signals that create a secondary low-frequency signal that is able to penetrate the seabed. This method allows the creation of low-frequency and low-beamwidth signals with relatively small transducers. The systems settings vary in each cruise depending on different parameters such as the water depth, survey speed, and seafloor reflection.

Table 3. Expeditions from which SBP data has been used in this study, sorted chronologically and with the name of the scientific platform they are based on.

| **Expedition Name** | **Year** | **Vessel** |
|---|---|---|
| ARK-VII/3 | 1991 | *R/V Polarstern** |
| HLY0503 | 2005 | *USCGC Healy* |
| AGAVE | 2007 | *IB Oden* |
| LOMROG I | 2007 | *IB Oden* |
| NEGC | 2008 | *IB Oden* |
| ASCOS | 2008 | *IB Oden* |
| SAT | 2009 | *IB Oden* |
| LOMROG II | 2009 | *IB Oden* |
| EAGER | 2011 | *IB Oden* |
| LOMROG III | 2012 | *IB Oden* |
| 2014 Canadian expedition to the North Pole | 2014 | *CCGS Louis S. St-Laurent** |
| SWERUS-C3 LEG2 | 2014 | *IB Oden* |
| 2015 Canadian expedition to the North Pole (no specific name identified) | 2015 | *CCGS Louis S. St-Laurent** |
| SWEDARCTIC 2016 | 2016 | *IB Oden* |
| SWEDARCTIC 2018 | 2018 | *IB Oden* |
| SAS | 2021 | *IB Oden* |

* Expeditions whose data was processed and interpreted for this study by Kai Boggild.

## 5.2 Data post-processing

Data acquired in raw-format (.raw) with Kongsberg SBP 120 installed on *IB Oden* needs to be converted into SEGY-format to be readable in post-processing and interpretation software. The *KM SBP* (Kongsberg, 2019) software was then used for replaying the .raw data acquired and saving it in SEGY-format. The software chosen for the interpretation of the sub-bottom profiles is the *SegyJp2Viewer* (Courtney, 2020). Before this, SEGY files are combined and speed-corrected using the *Combine Segy* (Courtney, 2015) software, and subsequently converted into JPEG 2000 (Jp2 hereafter) format using the *SEGYJp2* (Courtney, 2009) software.

The files are combined and speed-corrected in order to improve the visualization and interpretation since we get longer profiles with equidistant along-track distances in the X-axis. Without speed correction, the traces (recorded signals of the pings) are simply plotted one after each other in the X-axis of the profile, so when the vessel is standing still while the SBP keeps collecting data, all the traces of a standing vessel are displayed in the profile and can lead to misinterpretations (Fig. 7).

Jp2 files are commonly viewed as a greyscale image, however, these SEGY-encoded Jp2 files contain all the trace information derived from the SEGY header data. This way, SEGY data is encoded efficiently, allowing quick visualization of a large number of traces without excessive loading on system resources, and offering a framework for embedded interpretations that

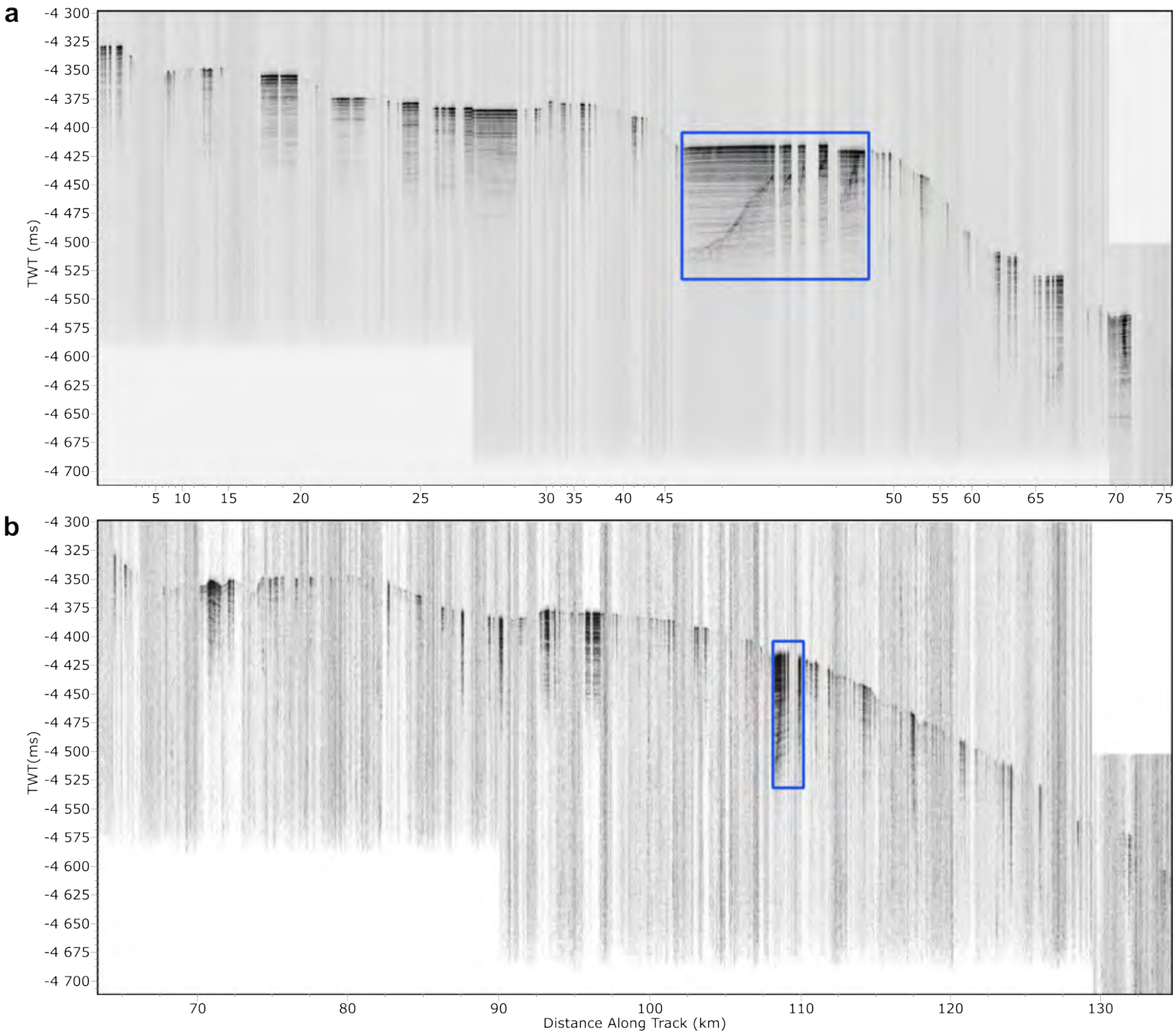


**Figure 7**. Sub-bottom profiles showing the difference between (a) non-speed-corrected and (b) speed-corrected sub-bottom data. Both are located in the same place. In (b) the sub-bottom is represented more accurately since the data is displayed as if the vessel was moving at the same speed during the survey. The blue box in (b) covers the same area as the blue box in in (a). In (b) the sub-bottom is classified as facies type 7a, whereas in (a), the parallel acoustic facies of a standing vessel can lead the classification to 8a. Note that the distance along track is not equivalent in both profiles because (b) is a combined profile (combination of the file of profile (a) and other files), and the distance along track represents the distance that the vessel covers from the beginning of each specific file.

accompany the data. But perhaps the main advantage of working with Jp2 files is the multi-scale nature of the Jp2 storage framework, which enables the display of near-optimal images as one zooms in and out (Fig. 8), again, at an incredible speed and with very little load on computer resources. This allows playing with vertical exaggeration, improving visualization in steep slopes, and continuously adjusting the displayed data in elongated profiles. When converting to Jp2, it is important to tell the software to calculate the signal power envelope, since it improves visualization of data acquired by echo sounders.

## 5.3 Categorization

The Jp2 files can now be opened in the *SegyJp2Viewer* for categorization based on the character of bottom echo and sub-bottom reflections, here following Boggild et al. (2018) acoustic facies classification scheme. The software allows you to draw horizons with different names, colours, and descriptions. Therefore, horizons with the name of the facies and compound facies are created to divide the sub-bottom profiles into sections with the same characteristics. These horizons are exported as shapefiles (a format for storing the geometric location and attribute information of geographic features; ESRI, 1998) to be imported into *QGIS* (Q. Devel-

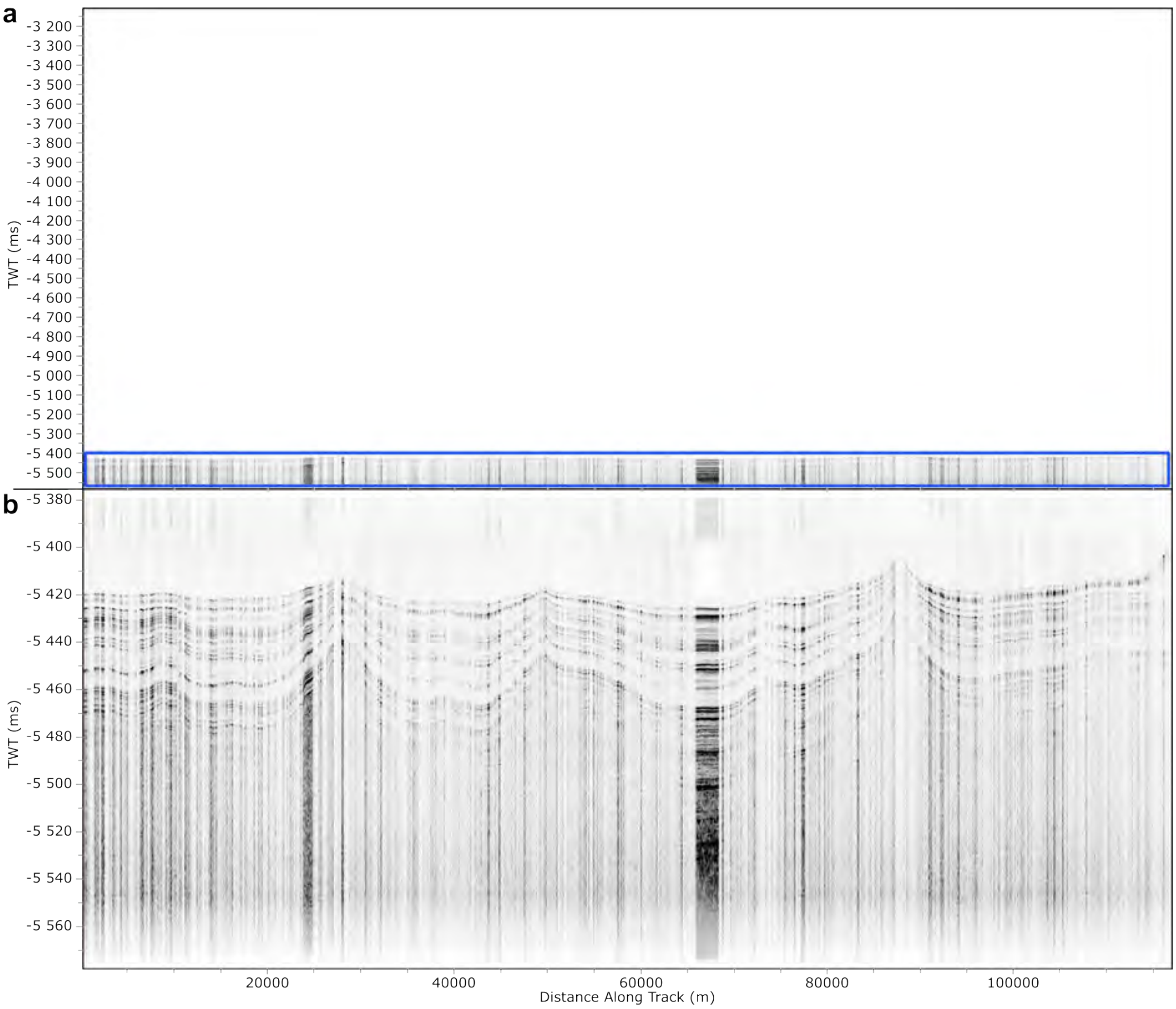


**Figure 8**. Sub-bottom profiles showing (a) a complete display of a file and (b) the zoomed profile. The blue box is the zoom applied to (a) profile. The result is (b), a near-optimal profile that adjusts the data to the shape of the zoom, exaggerating the vertical scale in this case.

opers, 2023), showing the ship tracks, but divided into all horizons created. Different colours to different facies types are assigned, so the result is a shapefile with the ship tracks of all the expeditions coloured according to Boggild et al. (2018) (Fig. 9). This visualization facilitates the spatial analysis of the facies, which will help with the polygon digitalization.

The procedure was first to characterize the profiles expedition by expedition, second to import all horizons in *QGIS*, then to revise all horizons, this time considering the spatial distribution of the facies and the bathymetry from the IBCAO Ver. 4.2 Grid (Jakobsson et al., 2020), and finally import again the revised horizons. A useful feature, both for the revision of the facies and the drawing of the polygons, was the possibility to directly open the Jp2 files from the *QGIS* environment. When the shapefiles are exported, they automatically save the information of where the profiles are stored (hyperlink), and those are shown in the *QGIS* attribute table as a field. Creating a new ‘Action’ that opens the URL of the field ‘hyperlink’ allows to click on a shapefile and automatically open the Jp2 file linked to that shapefile.

## 5.4 Mapping

The different facies are visualized as ship tracks (lines) in *QGIS*, meaning that for creating the acoustic facies-type map (Fig. 10), interpolation between lines and extrapolation is needed. Crucial for this step is the bathymetric information (200 x 200 m resolution) from the IBCAO Ver. 4.2 Grid (Jakobsson et al., 2020), together with its derived parameter ‘slope’. The slope is

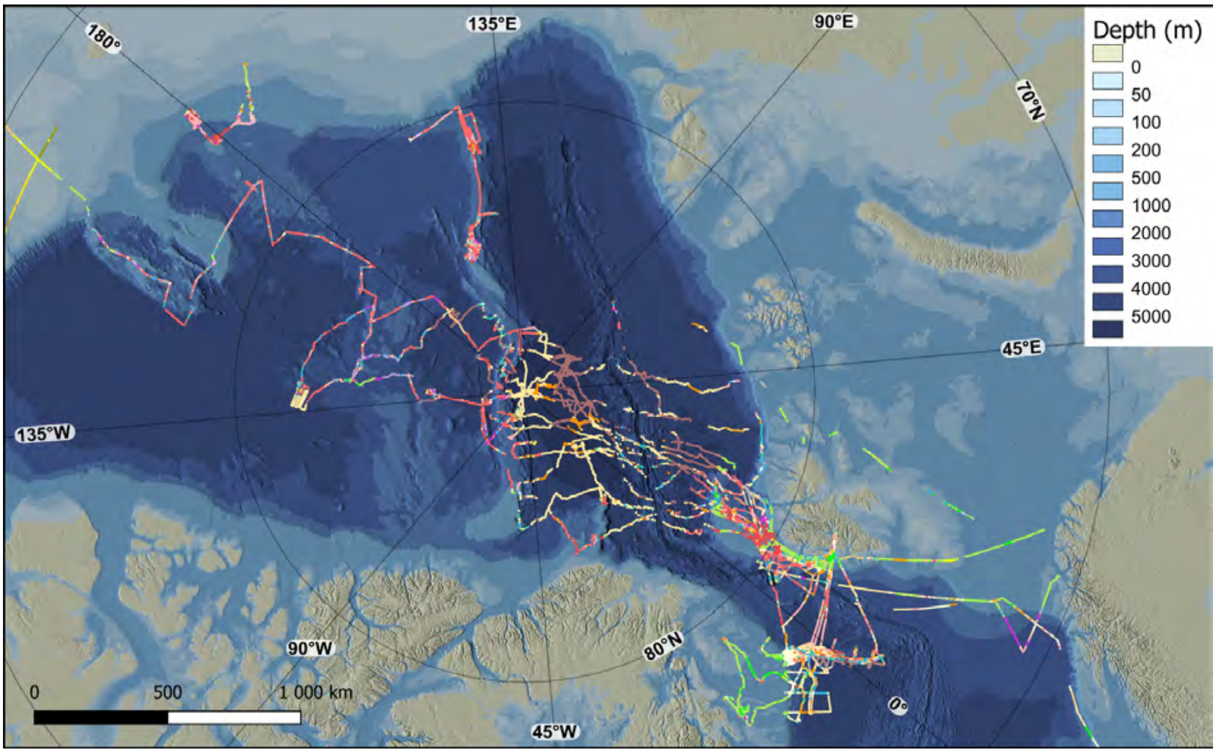


**Figure 9**. Map of the Arctic Ocean showing all the classified sub-bottom profiles during this project. The colours represent the different acoustic facies, see Appendix I for more information about the classification scheme.

the first derivative of the Digital bathymetric model (DBM), and it represents the rate of change of elevation for each digital cell. The 'slope' layer is created by means of the GDAL raster analysis incorporated in *QGIS*, with the IBCAO grid as the input layer. A 200 x 200 m resolution Data Identifier Grid from the IBCAO Ver. 4.2 Grid (Jakobsson et al., 2020) is also imported to *QGIS* to provide information about the type of data that a grid cell of the bathymetric layer is based on, allowing distinction between the actual bathymetric data and the interpolated one.

Thus, a new vector layer is created for drawing the polygons that group acoustic facies of the same type together. The *QGIS* Advanced Digitizing Toolbar is used for drawing the polygons together with the Snapping Toolbar, which is key for avoiding overlap between polygons and accelerating the process. The shape of the polygons depends on the boundary between facies of different types and the bathymetric information. This means that in areas where sub-bottom information is relatively poor, the extension of the polygons can only be guessed, resulting in rather unnatural angular shapes. While drawing the polygons, the facies type assigned to the profiles is also continuously being revised (which implies modification and exportation of horizons in *SegyJp2Viewer* followed by the importation in *QGIS*) in order to refine the end product as much as possible. Last adjustments were made considering previously published studies of other expeditions (Gebhardt et al., 2011; Howe et al., 2008; Spielhagen et al., 2004; P. R. Vogt et al., 1994).

Once the facies-type map is made, each polygon has to be geologically interpreted in terms of the processes that shaped the surficial strata. To do that, we followed when possible the interpretation given by Boggild et al. (2018) to each facies or compound facies type depending on where the facie is found (continental shelf, slope, abyssal plain…). Since the facies and interpretations of the Amerasia Basin and part of the Eurasia Basin cannot always be extrapolated to our research area, the interpretation of newly defined compound facies was needed. The interpretation of these facies was based on the interpretation of the individual facies that form the compound facie. The result is a surficial geology map, which will be presented in the discussion section.

See Fig. 11 for an overview of the workflow of the methodology followed during this project. All maps in this work were produced by using *QGIS* (Q. Developers, 2023) and with the IBCAO

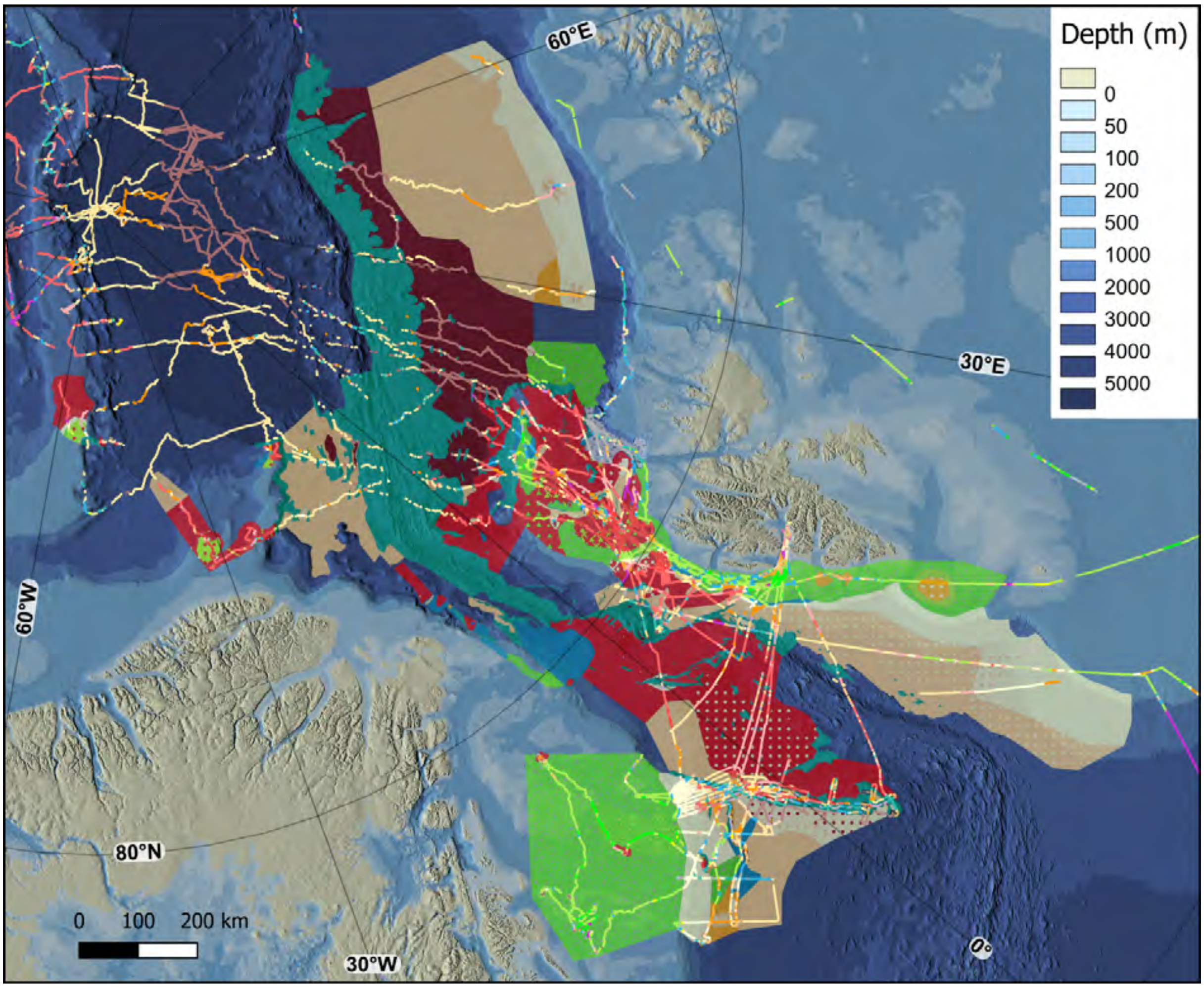


**Figure 10**. Facies-type map created by means of the interpolation and extrapolation of facies type horizons, which are the coloured lines plotted above the map. The colours of the lines represent the different acoustic facies, see the legend of the horizons in Appendix I. The symbols representing all facies types of the polygons are shown below the map.

Ver. 4.2 Grid (Jakobsson et al., 2020) as the base map. All sub-bottom profiles were produced by using *SegyJp2Viewer* (Courtney, 2020). All figures but Fig. 2 and 6 were produced by using *Inkscape* (I. Developers, 2023).

# 6 Results

The new compound facies that were not described by Boggild et al. (2018) in the Amerasia Basin and Amundsen Basin, are listed in Table 4. For attributing a generalized geologic interpretation to these facies, the following was considered: 1) geologic interpretation of similar compound facies described by Boggild et al. (2018), 2) individual geologic interpretation of the principal facies described by Boggild et al. (2018), since the newly compound facies are composed by principal facies already described, 3) the stratigraphic relationship between the principal facies that compose the new compound facies, 4) the region where they are found. Only six relatively small polygons represented by 5a truncating 8a facies were digitalized. This facies is characterized by smooth to rugose bottom echoes, and incoherent transparent deposits, truncating parallel coherent reflections. Two of the identified areas of 5a truncating 8a facies were found at the Yermak Plateau closest to northwestern Svalbard, other two at the foot of the Hovgaard Ridge and East Greenland Ridge, one at the flank of the East Greenland Ridge, and the other at the continental slope of northeastern Greenland.

At the Voronov Terrace and the Amundsen Basin, two small 5a over 9a polygons are found,

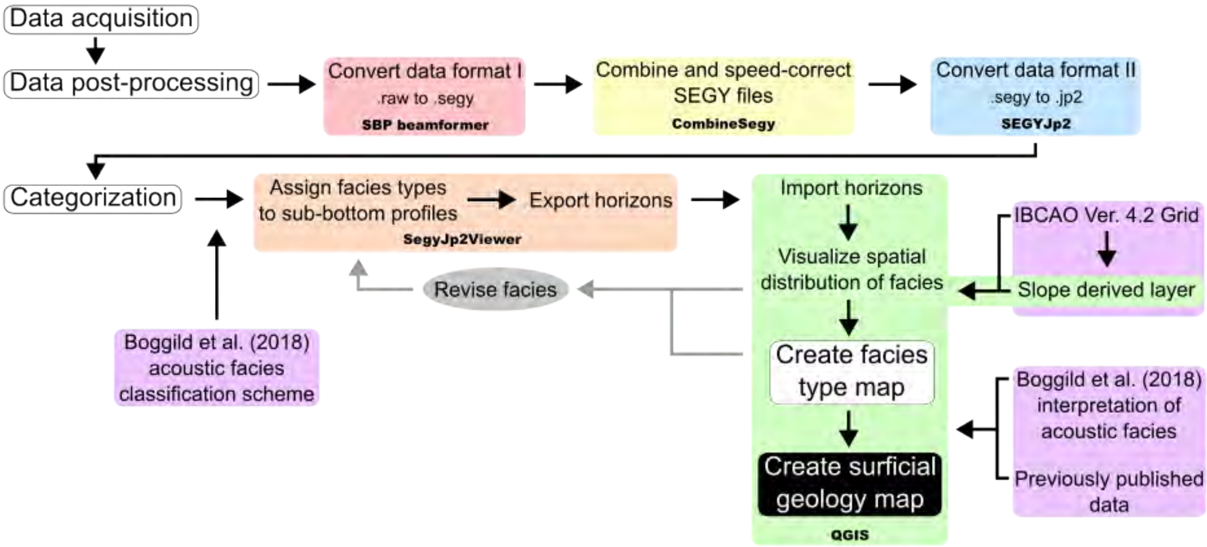


**Figure 11**. Scheme of the workflow from data acquisition to facies-type map digitalization. The white boxes symbolize the main sections. Coloured boxes are the steps followed within the main section that they succeed. Each colour but the purple represents the step or steps done using specific software. The text in bold is the name of the software. The purple boxes represent the external information that help with the categorization and the mapping. Forward arrows are drawn in black and backward arrows in grey. Backward arrows are related to the iterative process of revising facies (grey ellipse). The black box represents the end product of this project.

whereas at the northeastern Greenland Abyssal Plain, this facies covers a larger area. Even if 5a over 9a facies found in the Greenland Abyssal Plain present some local variations, their general appearance is a smooth bottom echo with transparent deposits overlying coherent parallel reflections that onlap on neighbouring bathymetry. Polygons represented by 7e over 3a, 7e over 5a, and 7e interbedded with 5a facies are not abundant and are linked to cross-shelf troughs and continental rises. The former is characterized by rugose seafloor with semi-coherent and amorphous sub-bottom reflections that alternate with each other and are underlain by a basal reflection. The others are also characterized by rugose seafloor with semi-coherent and amorphous sub-bottom reflections that alternate with each other, but in this case, overlying or interbedded with transparent wedge-shaped deposits. The four polygons represented by 8a truncating 8a facies are present at the northeast of Svalbard and characterized by smooth bottom with coherent parallel sub-bottom reflections that truncate other coherent parallel reflections.

The most representative facies in this study (Fig. 12) are 7a, 3b, 1a, 8a, 5a, and 9a, with more than 155 000, 138 000, 113 000, 96 000, 84 000, and 70 000 km$^2$ respectively. The reason why 7a facies cover a huge area is because they occupy a significant part of the abyssal plains as well as regions affected by bottom currents. 3b facies are mainly found on high slopes and 1a mainly on continental shelves but also on submarine elevations and abyssal plains. 5a facies are characteristic of the continental slopes and 9a of the abyssal plains.

The part of the Lomonosov Ridge that this study covers is represented at the northernmost area (Fig. 13a) by a semi-rugose seafloor with coherent parallel sub-bottom reflections (8a) with a strong basal reflection at some points (8a over 3a). At the south, there is a transition to a more rugose seafloor where it is possible to see small hyperbolae, with incoherent lens-shaped transparent deposits which in turn overlies coherent parallel reflections (5a over 8a), and then to a chaotic bottom echo with transparent sub-bottom that truncates coherent parallel reflections (1a truncating 8a; Fig. 13). Here we also find a small area where there is no truncation of coherent reflections, just acoustically transparent sub-bottom below the chaotic seafloor (1a). The SBP achieves penetrations up to 130 m below the seafloor (assuming a sound speed of 1500 m/s) in some parts of these polygons. In the 8a facies, a single v-shaped depression can be identified in one of the sub-bottom profiles at 1060 m deep (Fig. 13b).

The northeastern Morris Jesup Spur is characterized by 8a facies near the edge of the feature. Transitioning to shallower seafloor, the sub-bottom profiles show rugose seafloor, firstly with

**Table 4.** List of the compound facies found in this study that are not present in Boggild et al. (2018) classification scheme, their description, and the generalised geologic interpretation depending on the area they are found. Each compound facie type has a colour that will be used afterward for the mapping. An example of each compound facies is shown.

Additional compound Facies

| Category | Name | Example | Description | Generalized Geologic Interpretation |
|---|---|---|---|---|
| Smooth Seafloor/ Transparent | 5a truncating 8a | 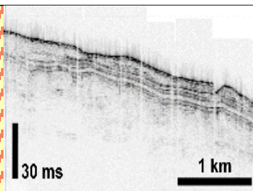  | Smooth to rugose bottom echo with incoherent transparent deposits truncating stratified coherent reflections. | **Shelf:** Ice-scoured sediment / diamict overlying eroded older sediments **Shelf / Rise:** Mass transport deposits truncating hemipelagic drape |
| | 5a over 9a | 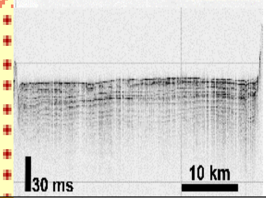  | Smooth bottom echo with incoherent transparent wedge deposits overlying flat-lying, coherent parallel reflections that may onlap neighbouring bathymetry. | **Abyssal Plain:** Mass transport deposits overlying flat-lying turbidites and interbedded hemipelagites |
| Coherent sub-bottom reflection = Bedded / Laminated | 7e over 3a | 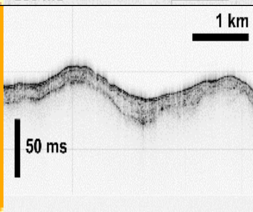  | Rugose, semi-coherent interbedded stratified and amorphous reflections, underlain by basal reflection. | **Shelf:** Deformed glacimarine sediments overlying diamict |
| | 7e interbedded with / over 5a | 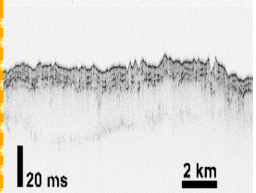  | Rugose bottom echo with semi-coherent contorted parallel/subparallel and amorphous sub-bottom reflections, interbedded with/over transparent wedge-shaped deposits. | **Shelf:** Deformed glacimarine sediments overlying diamict **Rise:** Deformed turbidites interbedded with / over mass transport deposits |
| | 8a truncating 8a | 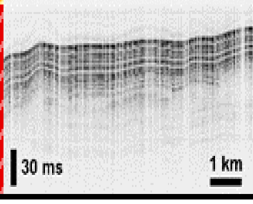  | Smooth bottom echo with draping coherent sub-bottom reflections truncating stratified coherent reflections. | **Shelf:** Hemipelagic drape overlying eroded older hemipelagic sediments |

acoustically stratified sub-bottom reflections that follow the seafloor morphology and truncate coherent parallel reflections below (8a over 1a truncating 8a), and secondly without stratification over the chaotic seafloor (1a truncating 8a; Fig. 13a). At the shallower parts of the southwestern Morris Jesup Spur and along the extension of the Greenland continental shelf located at the west of the spur, the main facies found are 8a over 1a truncating 8a, 8a over 1a, and 1a truncating 8a (Fig. 13a; Fig. 14a). Compared to the northeastern part, the facies 8a over 1a truncating 8a, and 1a truncating 8a show a thicker acoustically transparent unit here between the chaotic bottom and the truncated unit. These facies are separated into three different areas where regularly spaced parallel ridges are identified in the IBCAO bathymetry (Fig. 14b). At the easternmost located area, the ridges are orientated NW-SE with an approximate crest-to-trough height of 10 m. In the central area, the ridges are also orientated NW-SE with maximum crest-to-trough height of 30 m, while they turn to be orientated W-E with maximum crest-to-trough height of 45 m in the westernmost area. Smooth bottom echoes with coherent parallel sub-bottom reflections that are interbedded with acoustically transparent lens-shaped deposits (8a interbedded with 5a) can be found surrounding these areas (Fig. 13a; Fig. 14a). At the deeper parts of this region we find 8a facies with a few marked v-shaped depressions that disturb the most surficial stratigraphy and many minor depressions that have less visual effect on the stratigraphy and are shown in the DBM as crater-like features (Figs 14a, b, c). At the west of the Morris Jesup Spur, getting closer to the Amundsen Basin, the sub-bottom reflections present a more undulating morphology (7a). Similar sub-bottom reflections are found in the Voronov Terrace at the east of the Morris Jesup Spur. The small 5a polygons on the

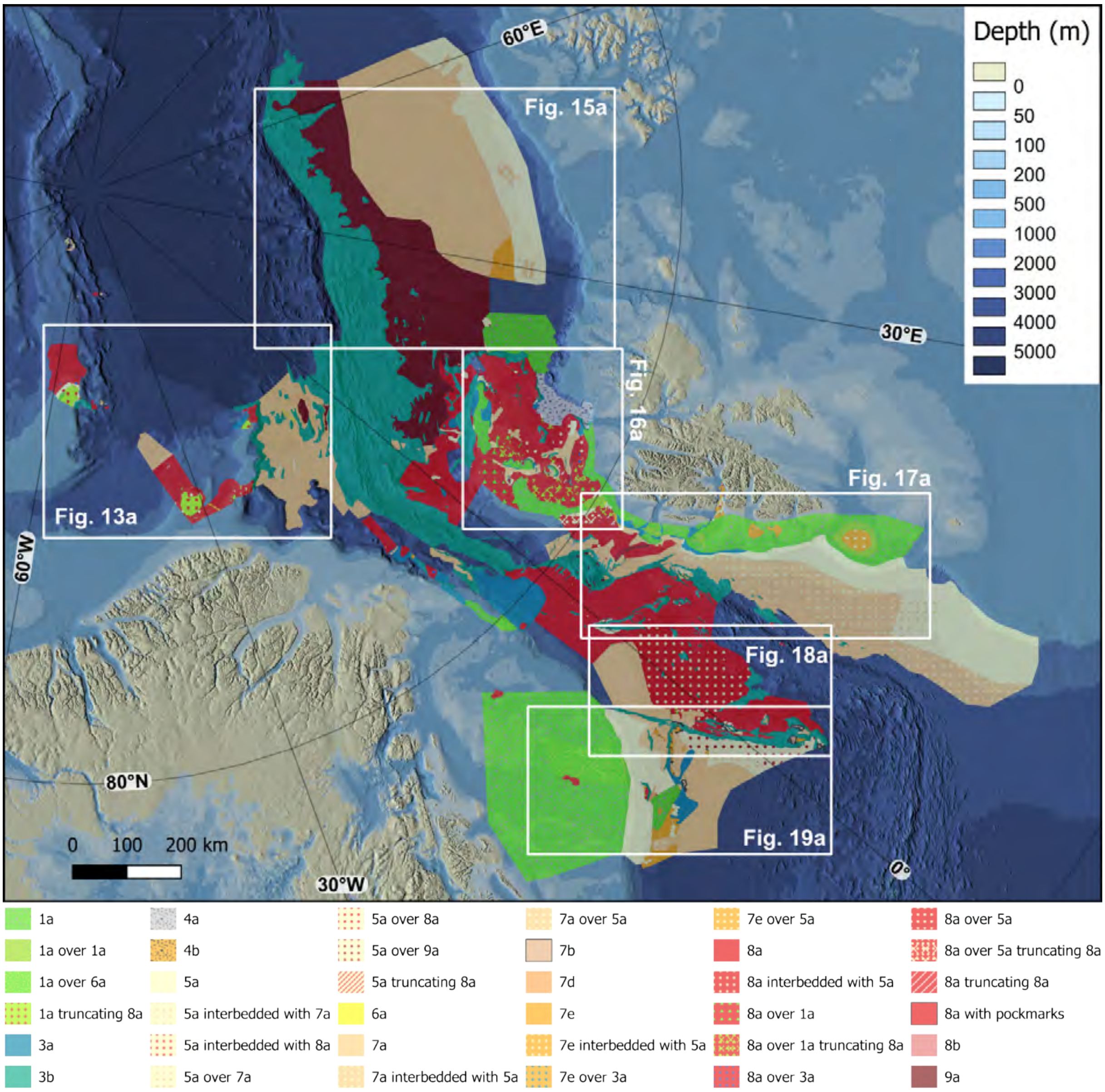


**Figure 12**. Facies-type map of the whole research area. The location of Figs 13a, 15a, 16a, 17a, 18a, 19a are represented by the white boxes. The symbols representing all facies types of the polygons are shown below the map.

Voronov Terrace (Fig. 13a) are coincident with wide rectangular depressions that truncate the adjacent 7a facies (Fig. 14d).

The Gakkel Ridge, Lena Trough, Spitsbergen Fracture Zone, Molloy Ridge, Molloy Fracture Zone, and Knipovich Ridge are characterized by broad or one-sided hyperbolic bottom echoes with no visible sub-bottom reflections (3b; Fig. 12). Even if some sedimentation (mainly 7a and 9a) can be identified between the volcanic ridges (Fig. 15b), they were entirely considered 3b as a whole given the chaotic nature of the ridges in terms of seafloor morphology. Acoustic facies type 3b are also linked with dramatic changes in seafloor depth, so for digitizing these polygons, the 'slope' layer was used as a base map. This process was not automatized (e.g. create polygons where the slope is greater than 6°) since the boundary between 3b and other facies types is done at different slope values depending on the site. However, in considerably steep areas verified by multibeam bathymetric data, 3b polygons were drawn even if there is no sub-bottom data. (Fig. 10).

The Nansen Basin adjacent to the Gakkel Ridge shows practically flat seafloor with coherent parallel sub-bottom reflections that accentuate their inclination with depth and onlap neighbouring bathymetric heights (9a). At the east of the Yermak Plateau, the Nansen Basin shows 1a facies (Fig. 15a, c). The rest of the Nansen Basin that this study covers is characterized by

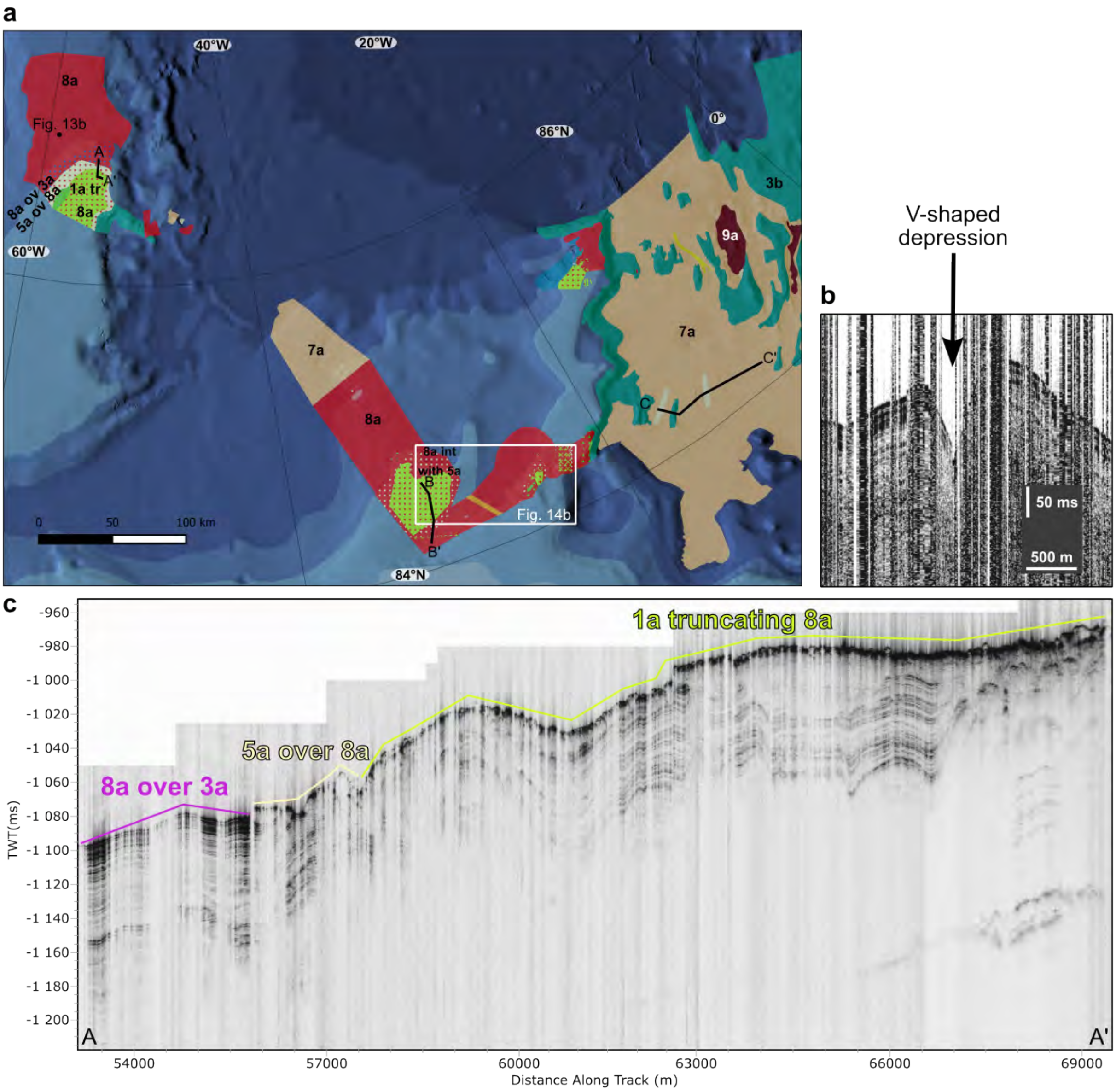


**Figure 13**. Facies-type map of the area encompassing the Lomonosov Ridge (polygons at the top left), the Morris Jesup Spur (polygons at the centre), and the Voronov Terrace (polygons at the right), with panels showing examples of sub-bottom profiles from the area. (a) Map showing the distinct facies of the area and the location of different figures. The name of some acoustic facies is indicated. The sub-bottom profile between A-A' is shown in Fig. 13c. The sub-bottom profiles between B-B' and C-C' are shown in Fig. 13a and d, respectively. The black point shows the location of Fig. 13b. The white box represents the location of the Fig. 14b. (b) Chirp sonar sub-bottom profile from the depression identified on the part of the Lomonosov Ridge that this study covers. The location is indicated in Fig. 13a. (c) Chirp sonar sub-bottom profile from the southern Lomonosov Ridge off the Greenland Margin. In Fig. 13a, the location of the profile between A and A' is shown. The different acoustic facies identified in the profile are indicated with coloured lines and names above the profile. The colours in the map (legend in Fig. 12) and in the profile represent the different acoustic facies.

7a facies. Adjacent to the 7a facies, at the continental rise and slope of the northern Barents Sea margin, we find smooth bottom echo with transparent lens-shaped sub-bottom (5a) that is draped by 7a facies at some points (Fig. 15a, d).

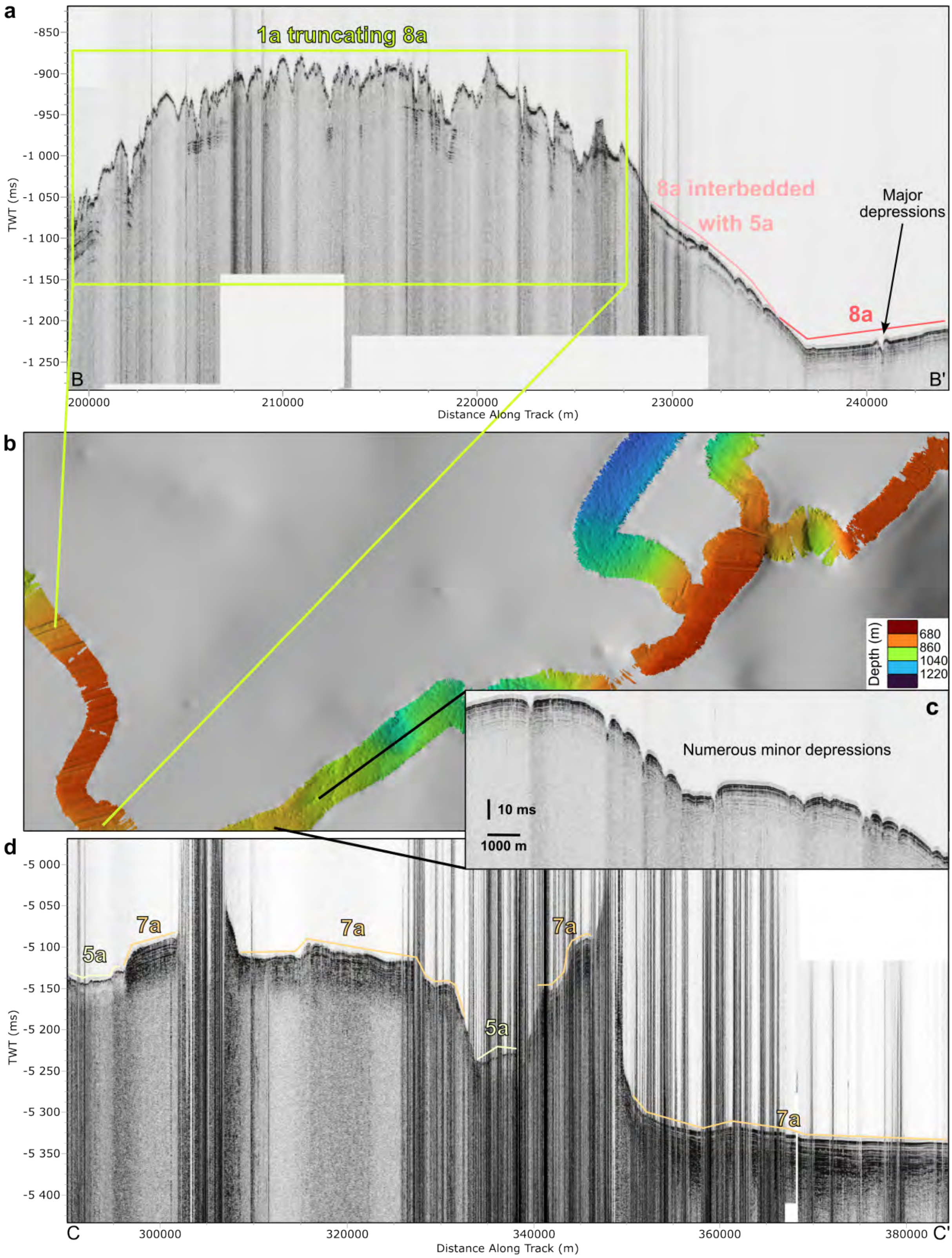


**Figure 14**. Bathymetric map of the southwestern Morris Jesup Spur accompanied by sub-bottom profiles acquired in that area and in the Voronov Terrace. (a) Chirp sonar sub-bottom profile from the extension of the Greenland continental shelf at the west of the Morris Jesup Spur. The location of the profile between B and B' is shown in Fig 13a. The green-yellow box indicates the part of the profile that corresponds to the ridges in Fig. 14b. An example of the major depressions found in this area is indicated. (b) Bathymetric map showing the morphology of the regularly spaced ridges found on the Morris Jesup Spur (right) and at its west (left), and the crater-like features. The sub-bottom profile of the ridges at the left (between the green-yellow lines) is shown in Fig. 14a. The sub-bottom profile of the minor depressions (between the black lines) is shown in Fig. 14c. Base map from IBCAO Ver. 4.2 by Jakobsson et al. (2020) with a higher resolution DBM from SAS 2021 expedition (Bringensparr and Castro, 2021) above. (c) Chirp sonar sub-bottom profile from the minor depressions identified on the 8a facies just west of the Morris Jesup Spur. The location is indicated between the black lines in Fig. 14b. (d) Chirp sonar sub-bottom profile from the Voronov Terrace. The location of the profile between C and C' is shown in Fig. 13a. The different acoustic facies identified in the profiles are indicated with coloured lines/box and names above the profiles.

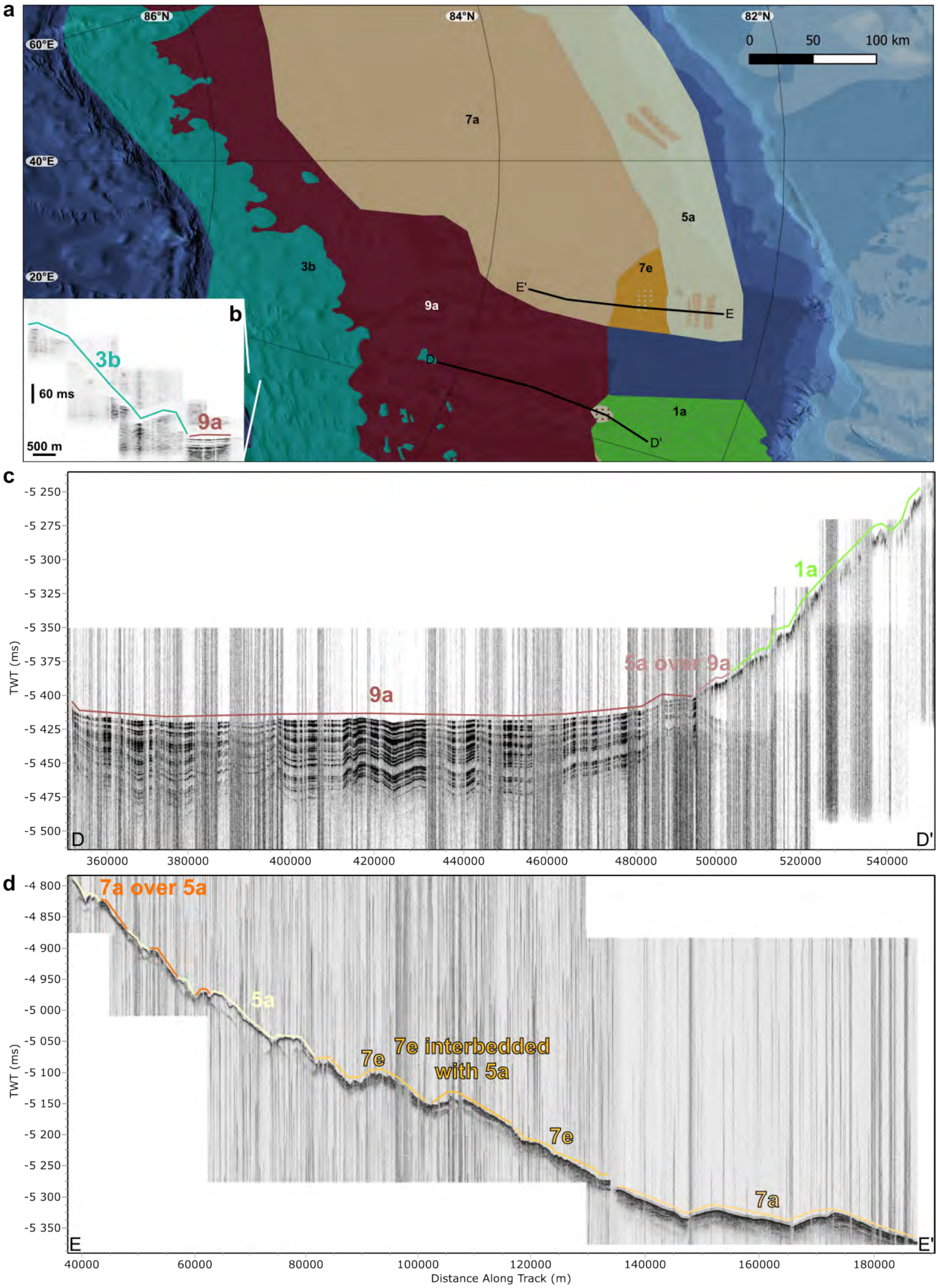


**Figure 15**. Facies-type map of the area that encompasses part of the Gakkel Ridge and Nansen Basin, with panels showing examples of sub-bottom profiles from the area. (a) Map showing the distinct facies of the area and the location of different figures. The name of some acoustic facies is indicated. The sub-bottom profiles between D-D' and E-E' are shown in Fig. 15c and d, respectively. The two white lines indicate the location of Fig. 15b. (b) Chirp sonar sub-bottom profile from the Gakkel Ridge exemplifying 3b facies and the deposition (9a in this case) that occur within the Gakkel Ridge. The location is indicated in Fig. 15a. (c) and (d) Chirp sonar sub-bottom profiles from the Nansen Basin. The location of the profiles between D and D', and between E and E' is shown in Fig. 15a. The different acoustic facies identified in the profile are indicated with coloured lines and names above the profiles. The colours in the map (legend in Fig. 12) and the profiles (add maybe legend in appendix, and change other captions) represent the different acoustic facies.

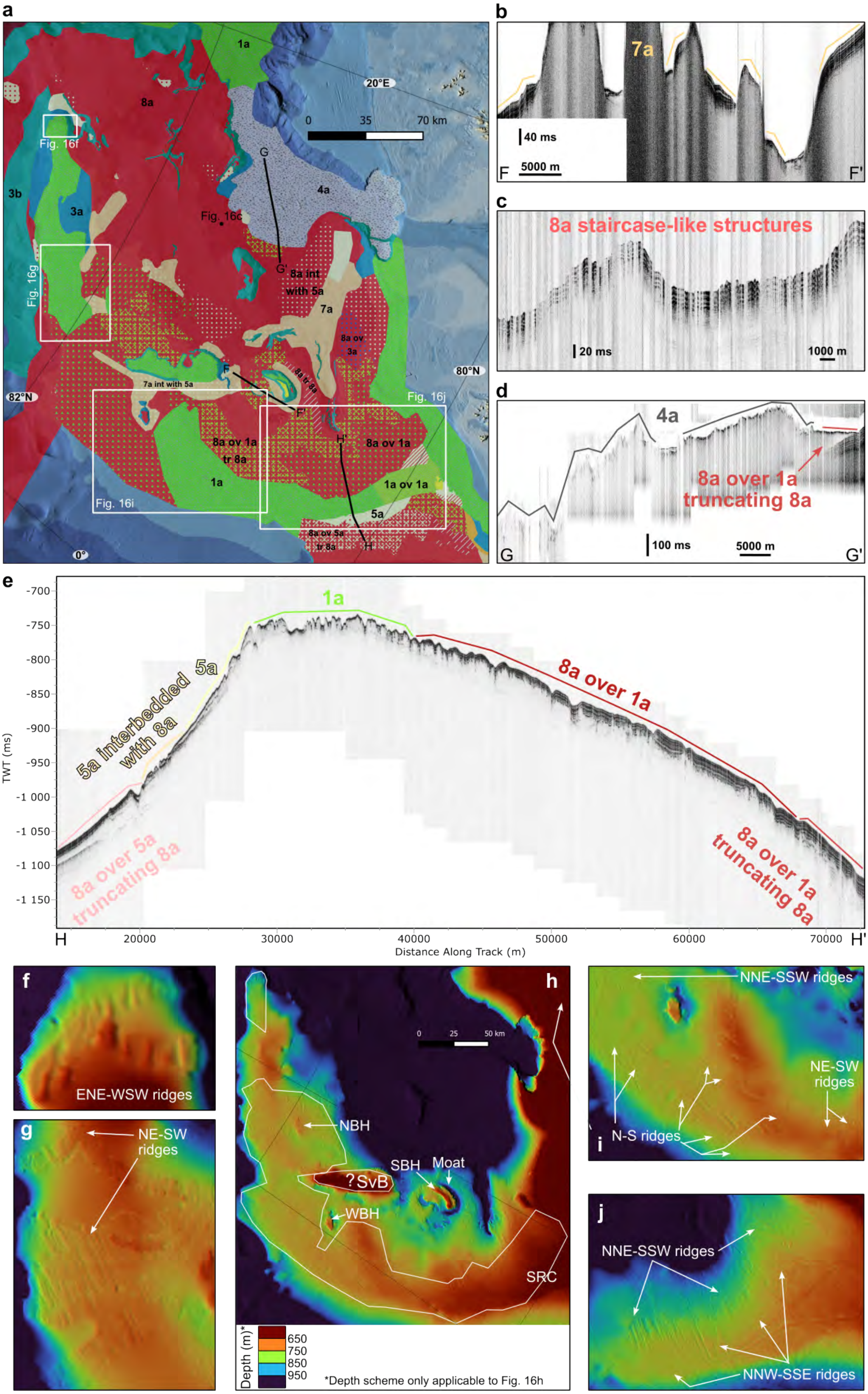


**Figure 16**. (Continued on the following page)

**Figure 16**. Facies-type map of the Yermak Plateau and the Sophia Basin, with panels showing bathymetric maps and sub-bottom profiles of this area. (a) Map showing the distinct facies of the area and the location of different figures. The name of some acoustic facies is indicated. The sub-bottom profiles between F-F', G-G', and H-H' are shown in Fig. 16b, d, and e, respectively. The black points show the location of Fig. 16c. The white boxes represent the location of Figs 16f, g, i, and j. (b) Chirp sonar sub-bottom profile showing the 7a facies of the depressions surrounding the Sverdrup Bank and the southeast basement high, also crossing the moat. The location is indicated in Fig. 16a between F and F'. (c) Chirp sonar sub-bottom profile showing the 8a staircase-like structures identified at the Sophia Basin. The location is indicated in Fig. 16a. (d) Chirp sonar sub-bottom profile transitioning from the undisrupted facies of the Sophia Basin to the facies affected by the Hinlopen landslide. The location is indicated in Fig. 16a between G and G'. (e) Chirp sonar sub-bottom profile from the southern ridge crest of the Yermak Plateau. The location of the profile between H and H' is shown in Fig. 16a. The different acoustic facies identified in the profiles are indicated with coloured lines and names above (or below) the profiles. The colours in the map (legend in Fig. 12) and in the profiles represent the different acoustic facies. (h) Bathymetric map of the Yermak Plateau. White polygons represent the areas with presence of regularly spaced elongated ridges, with a question mark on the Sverdrup Bank representing the uncertainty of the presence of ridges there. The main features found at the Yermak Plateau are indicated. NBH: NE basement high; SB: Sverdrup Bank; SBH: SE basement high; SRC: southern ridge crest; WBH: W basement high. (f), (g), (i), and (j) Zoomed bathymetric maps of the Yermak plateau with an adjusted colour scheme to better show the physiography of the ridges. Ridges with different orientation are indicated with arrows. The location of the figures is shown in Fig. 16a with white boxes.

The Yermak Plateau is composed of several different acoustic facies. Ordering them from chaotic to smooth seafloor echo we find 1a, 8a over 1a, 8a over 1a truncating 8a, and then the rest, which includes 8a, 8a truncating 8a, 8a interbedded with 5a, 7a, and 7a interbedded with 5a (Fig. 16). Areas covered by 1a and 8a over 1a facies are represented in the DBM as regularly spaced parallel to sub-parallel ridges (Fig. 16h). These features are distributed between depths of approximately 1100 and 500 m along almost the entire plateau. The northeastern ridges are orientated ENE-WSW with crest-to-trough heights around 30 m (Fig. 16f). At the north of the northeast basement high, the ridges are orientated NE-SW, less separated and with crest-to-trough heights around 15 m (Fig. 16g). At the north of the west basement high, ridges tilt to a NNE-SSW orientation, and at the west and south of this basement high N-S oriented ridges are found (Fig. 16i). Moving southward the orientation changes dramatically to NE-SW, and then to NNE-SSW (Fig. 16i,j). At the southern ridge crest, ridges orientated NNW-SSE appear, truncating the NNE-SSW-oriented ridges (Fig. 16j). The only bathymetric high within the plateau where the ridges could be identified is the Sverdrup Bank, but the multibeam data is not clear enough to confirm it (Fig. 16h).

Simplifying, the 1a facies are found above 775 m deep on the outer part of the plateau and on the top of the Sverdrup Bank. 8a over 1a facies located at the northeastern plateau have 12 m of draping geometry below the seafloor, at the northwestern edge they have 7 m, and at the southern plateau, they have 10 m. Typically these areas are found adjacent to 1a facies areas but at lower depths, and they transition to 8a over 1a truncating 8a, or to 8a while going deeper (Fig. 16a, e). The transitions are also accompanied by an increase in the thickness of the draping layer. At the southwesternmost edge, 1a facies transition to 5a instead, which in turn transitions to 8a over 5a truncating 8a, or to 8a over 1a truncating 8a (Fig. 16a, e). In this area, depressions on the seafloor can be found rather regularly (Fig. 17c). Some of them disturb the coherency of the sub-bottom reflections. 7a-related facies are found surrounding bathymetric highs present in the plateau (including the Sverdrup Bank, the west basement high, and the southeast basement high), and around the Litke Trough (Fig. 16a, b). The Sophia Basin is characterized by 8a, and 8a interbedded with 5a facies (Fig. 16a). At the northeast of the Mosby Seamount, we find 8a facies type with a small bathymetric expression that continues down sub-bottom, previously referred to as staircase-like structures by Winkelmann et al. (2008). The pattern looks like small steps very close to each other that affect the entire coherent parallel sub-bottom reflections (Fig. 16c). At the escarpment of the Hinlopen landslide and the adjacent area, the bottom echoes show narrow overlapping hyperbolae with no sub-bottom reflections (4a; Fig. 16a, d). A hummocky seafloor morphology containing "mega-blocks" can be observed in the DBM. Between the Yermak Plateau and the Lena Trough we find 8a facies type, and between the plateau and the Molloy Ridge 8a facies that transition to 7a.

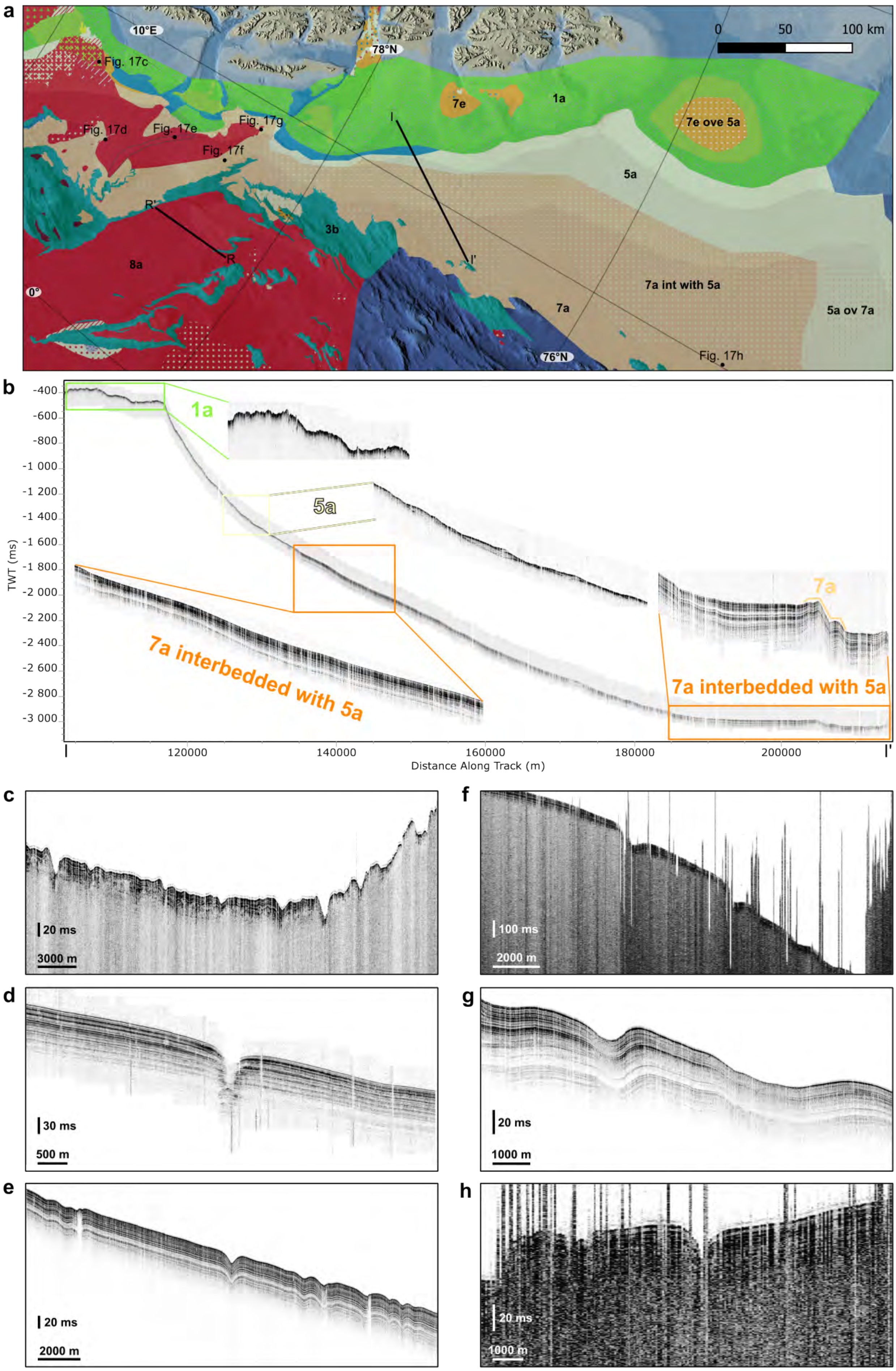


**Figure 17**. (Continued on the following page)

**Figure 17**. Facies-type map of the area that encompasses the western continental shelf and slope of Svalbard and Barents Sea, and the surroundings of the Hovgaard Ridge, with panels showing examples of sub-bottom profiles from the area. (a) Map showing the distinct facies of the area and the location of different figures. The names of some acoustic facies are shown. The sub-bottom profile between I-I' is shown in Fig. 17b. The sub-bottom profile between R-R' is shown in Appendix II. The black points show the location of Figs 17c, d, e, f, g and h. (b) Chirp sonar sub-bottom profile from the western Shavlbard shelf to the continental rise off Knipovich Ridge. The location of the profile between I and I' is indicated in Fig. 17a. Zoomed parts of the profile are represented by colour boxes and are connected to the zoomed profiles by lines with the same colour. The facies type names are indicated. The colours in the map (legend in Fig. 12) and in the profile represent the different acoustic facies. (c), (d), (e), (f) and (g) Chirp sonar sub-bottom profiles from the western Svalbard continental slope showing the variety of depressions and the blanking identified in this area. (h) Chirp sonar sub-bottom profile from the western Barents Sea continental rise showing the v-shaped depression identified there. The location of the profiles is shown with black dots in Fig. 17a.

The continental shelf of the western Barents Sea and Svalbard is mainly characterized by 1a facies (Fig. 17a, b). At the cross-shelf troughs the sub-bottom gets a bit more complex with other chaotic reflections (1a over 1a), smooth reflection (1a over 6a), or rugose semi-coherent interbedded with amorphous reflections (7e; Fig. 17a) underlying the chaotic seafloor echo. At the continental slope between the Svalbard margin, the Molloy Ridge, and the Molloy Fracture Zone, the facies found are 8a and 7a. Here we also identify major depressions truncating the stratigraphy (Fig. 17d, f), minor depressions coherent with the stratigraphy (Fig. 17e), and blanking of the sub-bottom data (Fig. 17g). The slope between the Knipovich Ridge and the margin of the western Barents Sea and Svalbard is characterized by 5a facies. Moving downslope these facies transition to 7a interbedded with 5a and then to 7a facies type (Fig. 17a, b) where a v-shaped depression is found (Fig. 17h).

West of the Molloy and Knipovich Ridges, the facies found are mainly 8a which are in contact with 8a interbedded with 5a facies from the Boreas Abyssal Plain, and with 7a facies at the northeast and at the west of the Boreas Abyssal Plain (Fig. 17a; 18a, b). Sub-bottom profiles from the 8a area show two depressions truncating the stratigraphy (Appendix II). Within the 8a interbedded with 5a polygon, vertical displacements that disrupt the entire stratigraphy (Fig. 18b) are commonly found. The hummocky and steep flanks of the East Greenland Ridge are characterized by 3b facies, whereas the gently sloping parts of the ridge are represented by 8a-related facies at the middle part and by 7a-related facies at the northwestern and southeastern part (Fig. 18a, c). Here we find the region of the research area with the most presence of seafloor 7b facies type (Fig. 18a), which is characterized by a regularly undulating seafloor with sub-parallel stratified sub-bottom reflections forming pinching planes (Fig. 18c).

At the part of the Greenland Abyssal Plain adjacent to the East Greenland Ridge we find smooth bottom echo with transparent lens-shaped deposits overlying 9a facies (Fig. 19). But 9a facies here are a bit different: 1) the coherent parallel sub-bottom reflections just below the 5a facies lose their coherency at a few points and they recover it after 500 - 2500 m (Fig. 19c), 2) instead of onlapping all neighbouring bathymetry, this facies generally abut on 3b and 4b (rough seafloor with semi-coherent sub-bottom reflections forming narrow hyperbolae facies) facies (Fig. 19c), 3) in two sub-bottom profiles, a few 9a reflectors onlapping other 9a reflectors can be identified, 4) at the southeasternmost part of this 5a over 9a polygon, completely vertical 10 m displacements of the coherent reflections are found, and the length of these displacements decrease with decreasing depths, until reaching 5a facies, which do not present displacement (Fig. 19b). The 4b facies in contact with the 5a over 9a are also different than the strict 4b (Fig. 19a, d). Here, they look like a mixture between 4b and 7b. In some parts, they look more similar to 4b, but the more extensive part is represented by a seafloor with some summits that can be separated by flat depressions, with parallel to sub-parallel sub-bottom reflection that can form narrow hyperbolae. Below most of the summits blanking is altering the data, even if some acoustically stratified sediments can still be discerned (Fig. 19a, d). The other part of the Greenland Abyssal Plain covered by this study is primarily classified as 7a which transitions to a high amplitude irregular seafloor echo with amorphous sub-bottom reflections (3a) at its west (Fig. 19a).

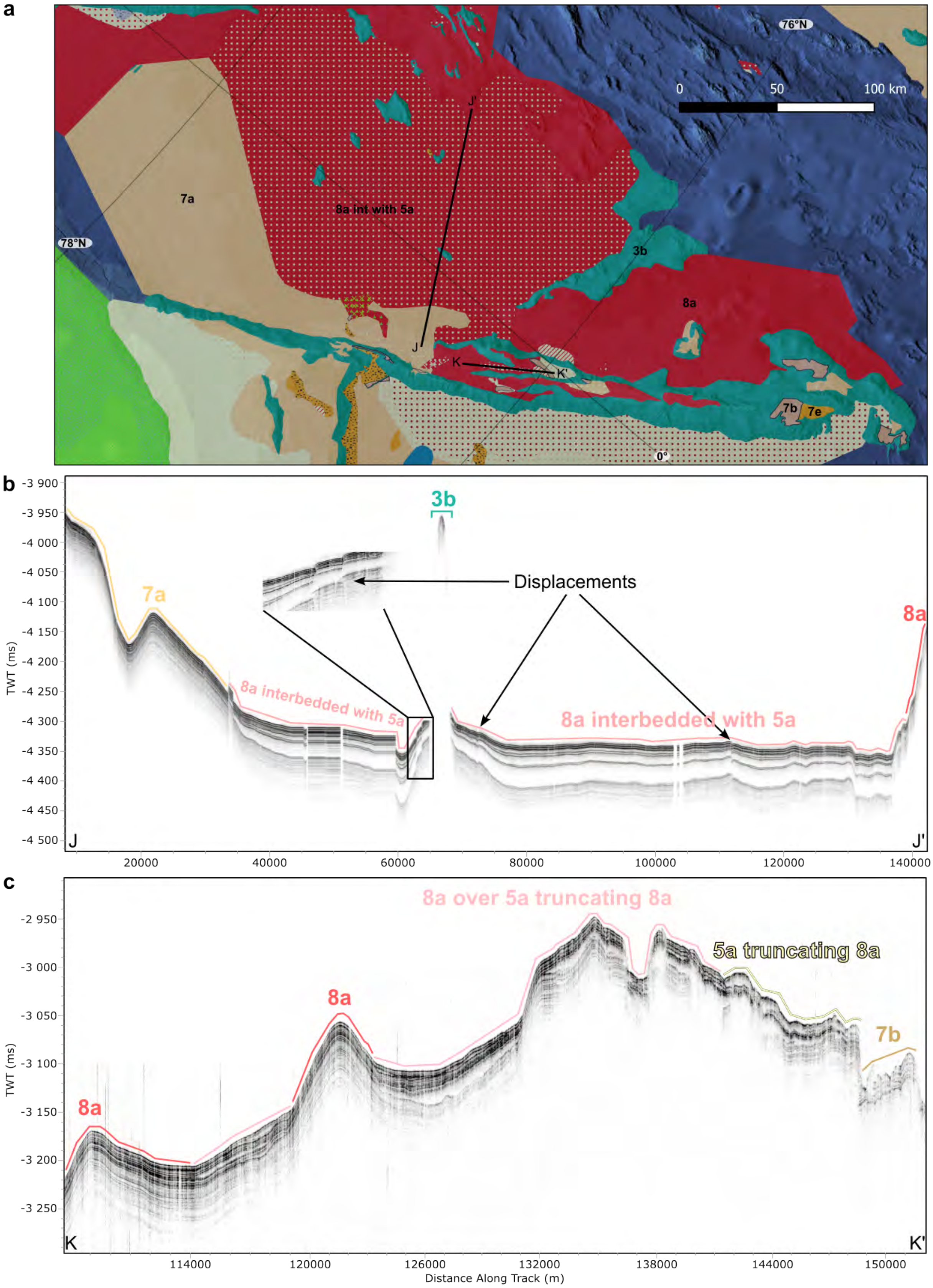


**Figure 18**. Facies-type map that focuses on the Boreas Abyssal Plain and the East Greenland Ridge, with panels showing examples of sub-bottom profiles from the area. (a) Map showing the distinct facies of the area and the location of different figures. The name of some acoustic facies is indicated. The sub-bottom profiles between L-L' and K-K' are shown in Fig. 18b and c, respectively. (b) Chirp sonar sub-bottom profile crossing the Boreas Abyssal Plain. The location of the profile between J and J' is indicated in Fig. 18a. The displacements identified in this area are indicated. (c) Chirp sonar sub-bottom profile along part of the East Greenland Ridge. The location of the profiles between K and K' is shown in Fig. 18a. The different acoustic facies identified in the profile are indicated with coloured lines and names above the profiles. The colours in the map (legend in Fig. 12) and in the profiles represent the different acoustic facies.

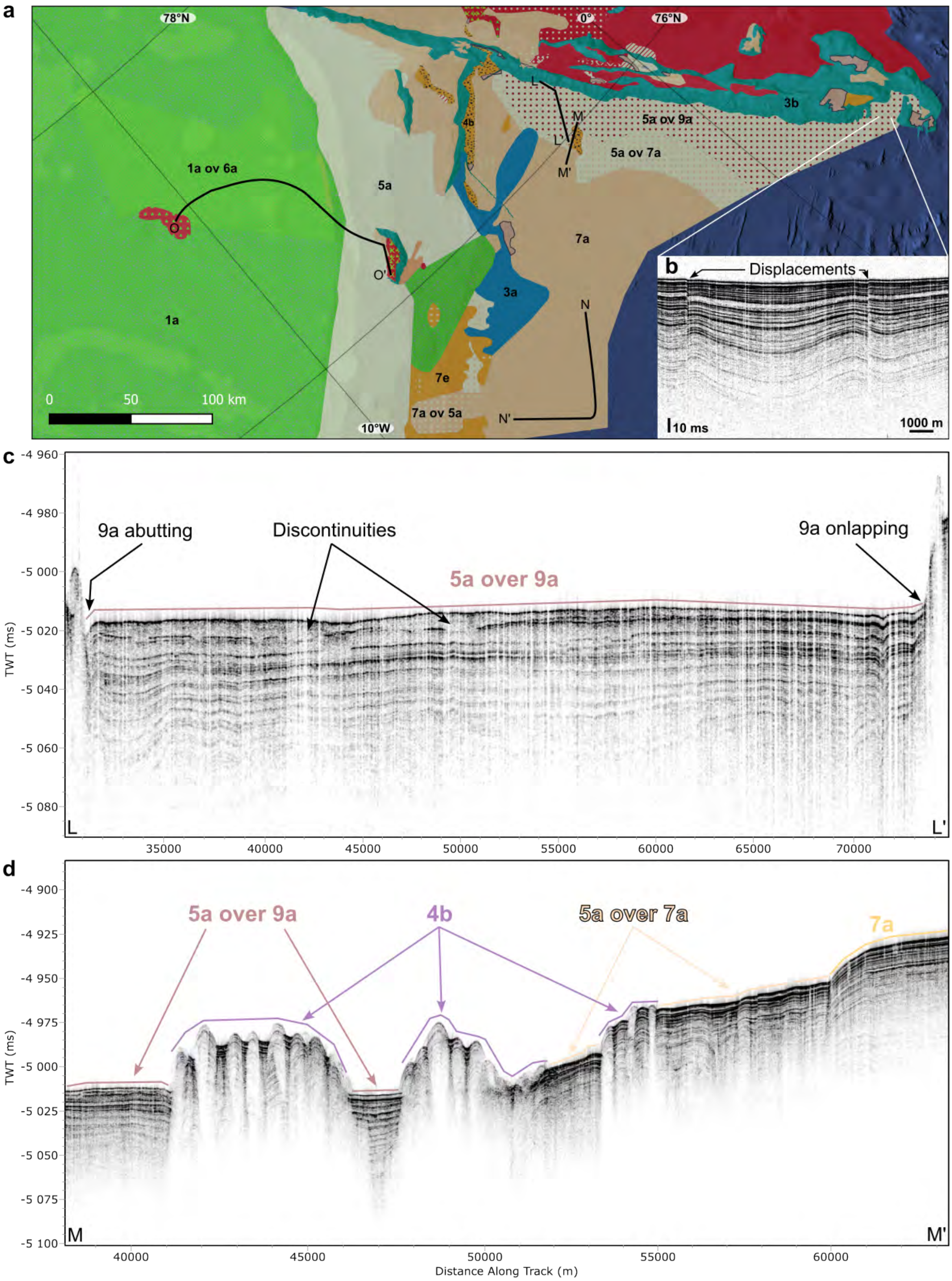


**Figure 19**. Facies-type map focusing on the northeastern part of the Greenland Abyssal Plain, and part of the northeastern Greenland shelf and slope, with panels showing examples of sub-bottom profiles from the area. (a) Map showing the distinct facies of the area and the location of different figures. The name of some acoustic facies is indicated. The sub-bottom profiles between L-L' and M-M' are shown in Fig. 19c and d, respectively. The sub-bottom profiles between N-N' and O-O' are shown in Fig. 20a and b, respectively. The two white lines indicate the location of Fig. 19b. (b) Chirp sonar sub-bottom profile showing the displacements identified at the Greenland Abyssal Plain just next to southwestern East Greenland Ridge. The location is indicated in Fig. 19a. (c) and (d) Chirp sonar sub-bottom profiles from the northeastern Greenland Abyssal Plain. The location of the profiles between L and L', and between M and M' is shown in Fig. 19a. In (c), the characteristic features of 5a over 9a facies found in this region are indicated. The different acoustic facies identified in the profiles are indicated with coloured lines, arrows, and names above the profiles. The colours in the map (legend in Fig. 12) and in the profiles represent the different acoustic facies.

Four seafloor depressions are identified in the 7a profiles of this area (Fig. 20a), some are located on long sinuous channel-like depressions that the DBM show. At the northwestern part, before arriving at an escarpment (3b), 7a facies transition to 4b (Fig. 19a).

At the northeastern continental rise of Greenland proximal to the East Greenland Ridge, 7a is the most characteristic facies, with a relatively small 4b polygon in the middle (Fig. 19a). The southeastern part of the covered continental rise is characterised by 1a and 7e facies, and some smaller polygons combining 7a and 5a facies with different stratigraphic relationship (Fig. 19a). The continental slope is almost entirely composed of 5a facies (Fig. 19a; 20b). Only in two bathymetric elevations in this area, different facies are identified: 7a in the northeast and 8a over 1a truncating 8a in the southwest (Fig. 19a; 20b). The only place where we find a high amplitude smooth seafloor echo that truncates the semi-parallel stratified sub-bottom reflections is at the foot of this last elevation (7d; Fig. 19a). The covered part of the northeastern continental shelf of Greenland shows 1a facies with a big region in the middle showing 1a over 6a facies (Fig. 19a; 20b). On two small areas, one at the middle of the Norske Trough (Fig. 19a; 20b) and the other at the north of the Belgica Bank (Fig. 12), 8a over 1a facies are found.

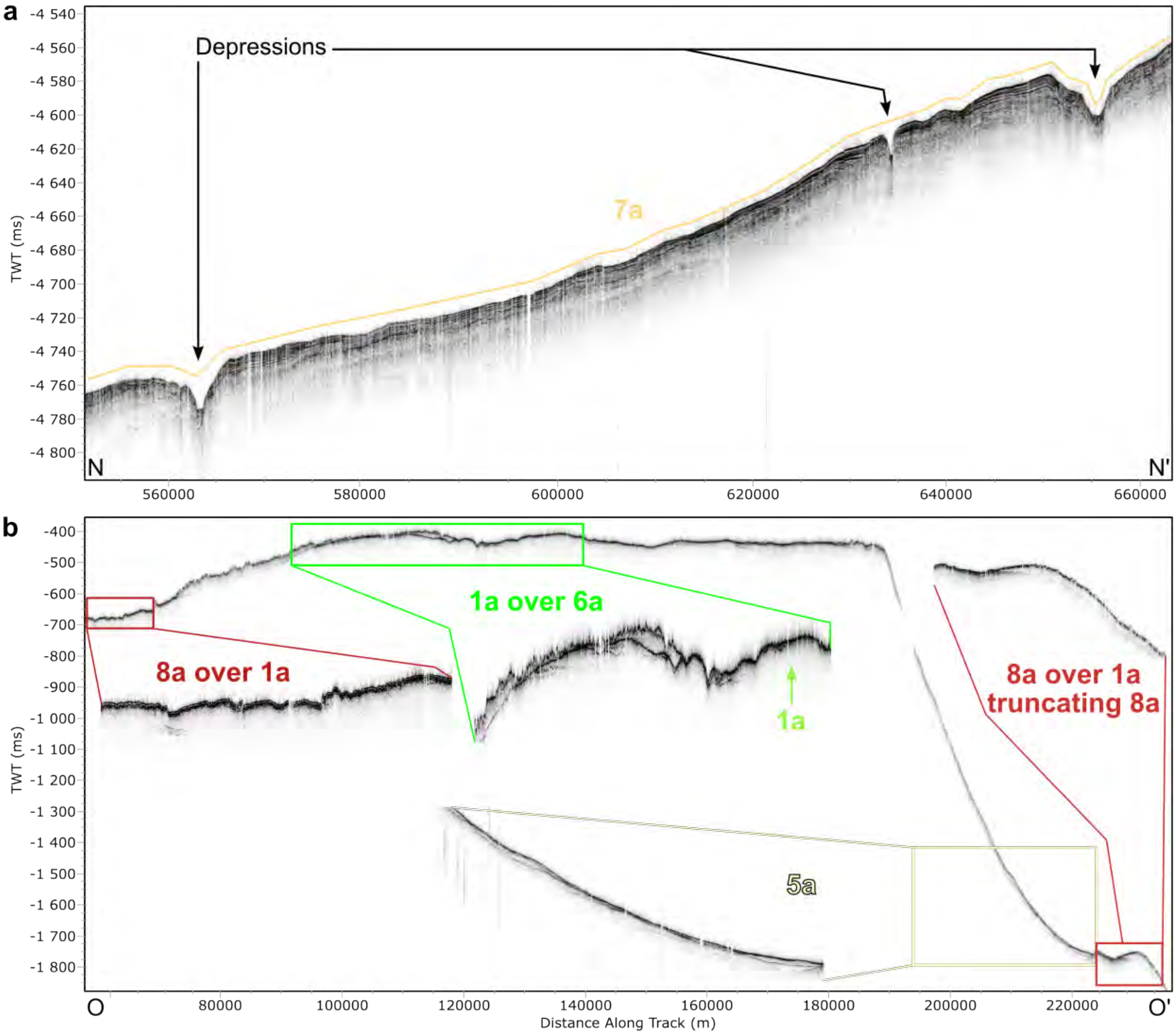


**Figure 20**. Sub-bottom profiles acquired off northeastern Greenland. (a) Chirp sonar sub-bottom profile from the northern Greenland Abyssal Plain. The location of the profile between N and N' is indicated in Fig. 19a. Depressions identified at that area are indicated. (b) Chirp sonar sub-bottom profile crossing the northeastern continental shelf of Greenland and part of the continental slope. The location of the profile between O and O' is indicated in Fig. 19a. Zoomed parts of the profile are represented by colour boxes and are connected to the zoomed profiles by lines with the same colour. The different acoustic facies identified in the profiles are indicated with coloured text and lines/boxes.

# 7 Discussion

## 7.1 Using the facies defined for the Amerasia Basin, Lomonosov Ridge and Amundsen Basin

In general, the acoustic facies defined and described by Boggild et al. (2018) work well to map the surficial geology in the research area that this study covers. Besides 5a over 9a, the newly defined compound facies do not cover large spatial areas, and regarding their characteristic bottom echoes and sub-bottom reflections, they do not differ much from the previously defined compound facies. Therefore, these new facies could easily be assigned to fit other compound facies without losing much information. This may be the way forward when the map created in this study is to be incorporated into the "IBCAO geology" project (Boggild et al., 2018; Mosher et al., 2015; van der Krogt, 2018). In the latest version of the surficial map of the Amerasia Basin made available by Boggild for this study, four small 5a over 9a polygons were outlined, meaning that maintaining this compound facie for the "IBCAO geology" project should not be a problem.

In total, fifteen of the eighteen principal facies described by Boggild et al. (2018) are present in the surficial geology map that covers part of the Eurasia Basin, Fram Strait, Greenland Sea, and Norwegian Sea. The facies not present are 2a, 2b and 7c. Since facies 2a was defined as scoured bottom echo with amorphous/transparent sub-bottom and semi-parallel incoherent reflections, finding it in the study area is to be expected. Therefore, the explanation of its non-appearance could be attributed to the similarity of this facies to others like 1a over 1a, which instead were assigned during the classification of the sub-bottom profiles. The description of 2b facies is similar to 2a but with coherent sub-bottom reflections instead. This facies is rarely observed in the Amerasia Basin map, hence it was not expected to be found in this research area. Facies 7c, described as smooth undulating, coherent parallel stratified reflections with down-section transition to acoustically blank/chaotic reflectivity, could also be expected to appear in this research area. However, again, similar facies like 8a over 1a or 7e were instead assigned during the classification of some profiles.

In terms of compound facies, only fifteen of the previously defined thirty-four were applied in this study. The reasons for this could be various. One of the reasons has already been explained, and it is the assignment of other similar facies. If two or more similar facies could be assigned to a section of a sub-bottom profile, there was a tendency to assign the facie that is most common in the study area. This is way of simplification, enabling the resulting digitized map to contain the least number of different compound facies possible without losing information. A similar procedure was applied when grouping the interpretations of several profiles into polygons. If very similar facies were spatially close enough to be grouped in the same polygon, they were grouped, and the polygon would be assigned to the most abundant facies within. Another reason for only mapping fifteen compound facies in the Eurasia Basin is the difference in density of sub-bottom profiles between the Amerasia and Eurasia basins. Since there are fewer profiles in the Eurasia Basin, and these are more spatially dispersed, not as much information is being captured and less common facies could simply be missed. Another potential reason is the difference in physiography, sediment dynamics, glacial history, and water circulation between the Amerasia Basin and the research area of this study (e.g. the Mackenzie Delta, and submarine canyons and fans at the southern Canada Basin), which directly influence on the sub-bottom appearance. I would like to highlight that the absence of a principal facies or compound facies type in this map does not mean that the facies itself was not identified in any of the sub-bottom profiles, it means that it was not abundant or clear enough to form a new polygon.

## 7.2 Interpretation of acoustic facies

Firstly, I will write about the generalized geological interpretations given to the newly described compound facies, followed by a more detailed interpretation of each region, hypothesizing about the possible processes that made the seafloor and the sub-bottom look like they are now.

The interpretation of the 5a truncating 8a facies is very similar to the one of 5a over 8a. The difference is that in this case, 8a facies are truncated by the acoustically transparent unit. This leads to an interpretation of glacial diamict/till deposited over previously eroded stratified sediments on the continental shelf, and also mass transport deposited over stratified sediments with strength enough to erode the coherent stratigraphy on the continental slope and rise. Diamict refers to poorly-sorted deposits in general, whereas till refers to the unsorted material deposited below a glacier, and is the unsorted characteristic that makes them look acoustically transparent. From now on I will use diamict as the general term for the glacially-related acoustically transparent sediment, including iceberg turbate, which is the deformed and reworked sediment by the action of iceberg ploughing (Vorren et al., 1983). Abyssal plains are the only regions where 5a over 9a facies were identified and these facies can be interpreted as mass transport deposits overlying flat-lying turbidites that are in turn interbedded with hemipelagites. Facies 7e over 3a are only found on continental shelfs (cross-shelf troughs), so they are interpreted as deformed glacimarine sediments overlying diamict, due to the strong acoustic reflector below the 7e facies and acoustically transparent unit below the reflector. A similar interpretation is given to the 7e over 5a when found on the continental shelf. On the continental rise, 7e over 5a and 7e interbedded with 5a facies are interpreted as deformed turbidites interbedded with/over mass transport deposits. A plausible explanation for 8a truncating 8a facies is hemipelagic drape deposited over previously eroded hemipelagic drape. Alternatively, these facies could be interpreted as hemipelagic drape overlying a relatively thin layer of diamict that in turn truncates underlying hemipelagic drape. The reasoning behind the latter interpretation is the similarity between 8a truncating 8a and 8a over 1a truncating 8a facies. The dissimilarity between these two compound facies is the thinner and smoother acoustically transparent layer of 8a truncating 8a.

The southern Lomonosov Ridge off the Lincoln Sea surveyed is mainly reigned by hemipelagic drape (Fig. 21). The depression identified here (Fig. 13b) is approximately 1060 m water deep and looks similar to the features interpreted as iceberg scours on the Yermak Plateau by Vogt et al. (P. R. Vogt et al., 1994). Even though there is a downgrade in sub-bottom data quality in this region due to sea ice breaking, around 6 m of hemipelagic drape can be identified overlying the iceberg ploughmark. Assuming a sedimentation rate of 0.4 cm/ka determined from the closest gravity cores (Löwemark et al., 2012) would imply that the iceberg ploughmark was scoured around 1.5 Ma. Above 785 m deep, the hemipelagic drape starts getting more intensely disrupted by glacial erosion (Figs 13, 21). No hemipelagic drape is identified overlying the chaotic seafloor, meaning recent ice scouring. On the shallower parts, the sediment is directly affected by the ice scouring, while between the eroded parts and the undisrupted hemipelagic drape, the stratified sediment is covered by mass transport deposits likely coming from the glacial erosion at the crest of the Lomonosov Ridge. Multibeam data acquired in heavy sea ice conditions during the expedition LOMROG I prevents a precise description of the landforms originated by the glacial erosion (Jakobsson et al., 2010). A similar issue is found with the more recently acquired multibeam data during the SAS 2021 expedition. Therefore, hypothesizing about what caused this glacial erosion is not straightforward. The shape and orientation of our polygons would suggest an ice mass flowing from the SW to the NE, eroding the crest of the ridge (Fig. 22), and depositing the eroded sediment around the grounding area where the 5a over 8a polygon is (Fig. 13). This is very tentative, only sustained by two survey lines. At this region of the Lomonosov Ridge, the traces left by glacial erosion are found much shallower than on the central part and on the southern Lomonosov Ridge off Siberia, at depths of $\sim$1000 m and $\sim$1280 m respectively (Jakobsson, Nilsson, et al., 2016). Unlike the part covered in this study, the other parts of the Lomonosov Ridge that suffered glacial erosion have a 3-4 m thick drape layer overlying the glacial diamict, dating back the erosion to MIS 6 (Jakobsson, Nilsson, et al., 2016). Then, the southern Lomonosov Ridge off the Lincoln Sea appears to have experienced more recent erosion, likely due to its shallower position or a different source of the ice that grounded there. It could also be that the erosion also happened during MIS 6,

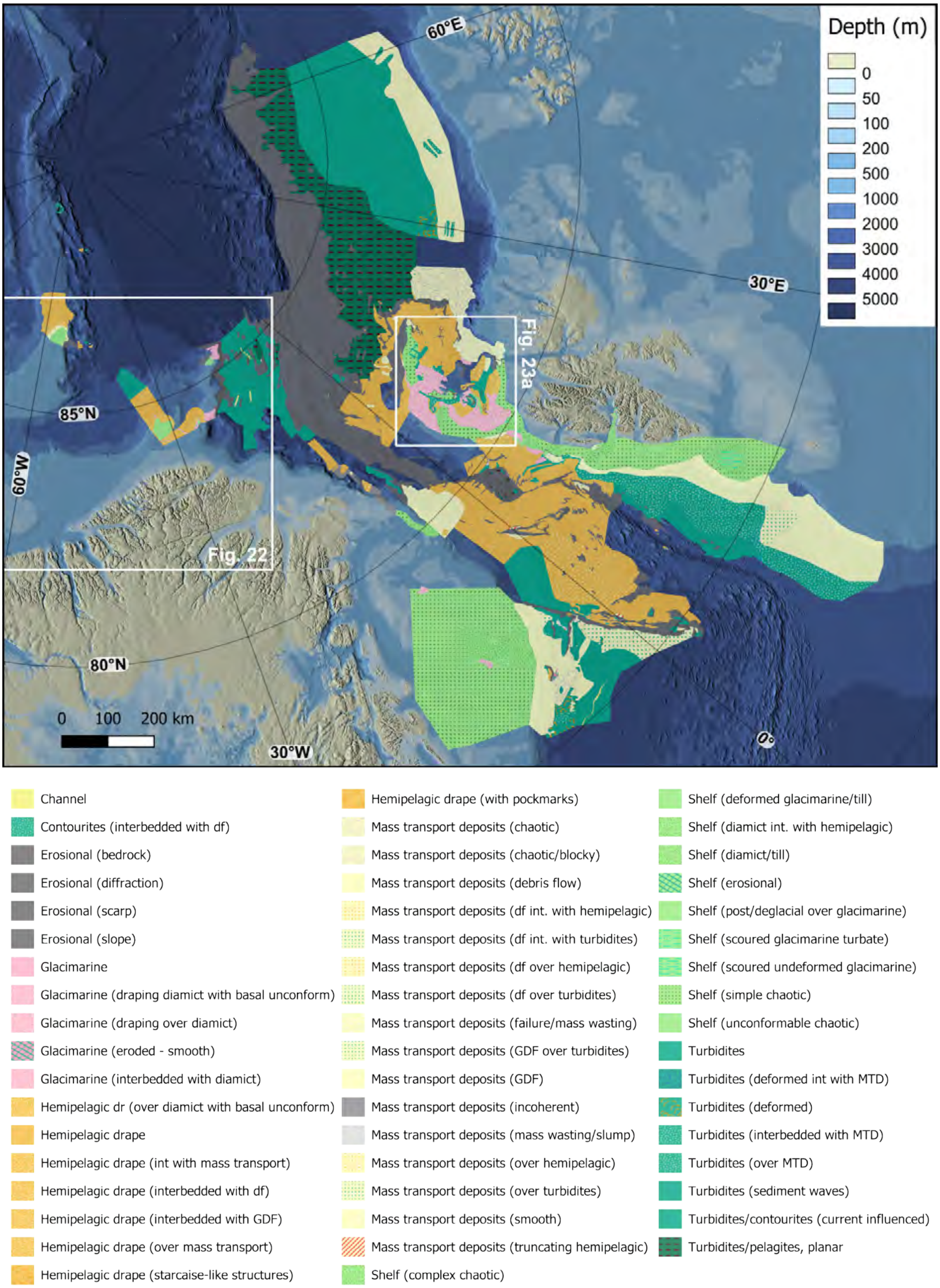


**Figure 21**. Surficial geology map of the whole research area. The location of Figs 22 and 23a are represented by the white boxes. The symbols representing the interpretation of the polygons are shown below the map. Df: debris flow; GDF: glacigenic debris flow; int: interbedded; unconform: unconformity.

but a lower sedimentation rate prevented a draping layer thick enough to be discerned by the SBP. The latter is likely if we consider a sedimentation rate of 0.4 cm/ka (Löwemark et al., 2012) translated to a sediment accumulation of 0.48 m during the last 120 ka, and a maximum vertical resolution of the echo sounder of 0.23 m. Jakobsson et al. (2010) suggest based on coring data, a Pre-MIS 5 age for the ice grounding, most likely MIS 6. A tentative scenario could be then, ice-shelf grounding during MIS 6 (red arrows in Fig. 22), and Post-MIS 6 ice grounding of less coherent ice masses (dark blue arrows in Fig. 22) that disturbed the glacial lineations formed by the ice-shelf grounding.

The Morris Jesup Spur and the bathymetric feature at its west that also protrudes from the northern Greenland continental shelf are also mainly composed of hemipelagic drape that is disrupted by glacial erosion at certain areas (Fig. 21). On the northeastern Morris Jesup Spur, iceberg ploughmarks were identified as deep as 1045 m below sea level (Jakobsson et al., 2010; Spielhagen et al., 2004), with the sub-bottom profiles showing a relatively thin and discontinuous diamict layer overlain by hemipelagic drape at the deeper areas, and thicker and more extensive diamict without drape over it at the shallower areas. This would indicate more recent and intense glacial erosion the shallower the seafloor is, even suggesting ice shelf grounding (Spielhagen et al., 2004) at the shallowest part of this area. As a matter of fact, on the shallower southwestern Morris Jesup Spur (<700 m deep) and the bathymetric feature at its west (<900 m deep), glacial lineations likely caused by the past action of an ice shelf are identified (Fig. 14b). There, the diamict layer is much thicker than on the northeastern part, the peak-to-trough height is greater, and the hemipelagic drape layers deposited over the diamict are not as apparent. Even if the region at the west of the Morris Jesup Spur is deeper than the southwestern spur, the glacial landforms tere are more pronounced (Fig. 14a, b), perhaps suggesting a closer position to the ice sheet that feeds the ice shelf. The glacial lineations on the southwestern Morris Jesup Spur are covered by a thin layer of hemipelagic drape, strengthening the previous idea (Fig. 21). Surrounding the areas that suffered ice-grounding, mass transport deposits are found within the hemipelagic drape (Fig. 21), probably originating from the bulldozing action of the ice shelf at the shallower areas and deposited downslope. Major depressions truncating the hemipelagic drape can be found in this area up to 1040 m deep and are interpreted as iceberg ploughmarks (Fig. 14a). A few potential ploughmarks are identified deeper than 1400 m, yet the resolution of the DBM is not high enough to confirm these features as iceberg ploughmarks. The minor depressions, found below 850 m deep, show the typical shape of pockmarks both in the sub-bottom profiles and the DBM (Fig. 14b, c). These features are likely linked to fluid flow from a gas-hydrate destabilization zone after deglaciation as Chand et al. (2012) suggested for the southwestern Barents Sea. No gas escaping from the pockmarks was captured by the Kongsberg EK80 echo sounder, perhaps indicating that these features are not active today.

Spielhagen et al. (2004) and Jakobsson et al. (2010) proposed that the major glacial landforms that they identified on the Morris Jesup Spur were ploughed during MIS 6. These landforms do not present overlying hemipelagic drape, consequently, the smaller landforms covered by a thin layer of hemipelagic drape were formed during previous glaciations, e.g. MIS 10 if we consider sediment rates at this area from Löwemark et al. (2012). No cores were retrieved from the southwestern Morris Jesup Spur, so setting a date for the glacial erosion is very tentative. Two scenarios could be possible if we consider the northeastern and southwestern together. One of them is assuming that all the ice scouring in the northeast is caused by icebergs. This opens the possibility of a different ice source in the northeastern and southwestern parts, with icebergs during MIS 6 and MIS 10 arriving from the hypothetical ice shelf grounding at the Lomonosov Ridge (Jakobsson, Nilsson, et al., 2016; light blue arrows in Fig. 22), with the Laurentide/Greenland ice shelves grounding on the southwestern spur and the bathymetric feature at its west during MIS 10/12 (red arrows in Fig. 22), and with the ice shelf only grounding at the west of the spur during MIS 6 or subsequent glaciations (dark blue arrows in Fig. 22). The other scenario would be icebergs from Lomonosov Ridge scouring the deeper parts of the northeastern spur during MIS 10 and MIS 6 (light blue arrows in Fig. 22), the Laurentide/Greenland ice shelves grounding on the shallower parts of the northeastern spur and all areas at the southwest during MIS 6 (red arrows in Fig. 22), and grounding only at the west of the spur during subsequent glaciations (dark blue arrows in Fig. 22). These scenarios are consistent with the orientation of the glacial lineations. Thus, the ice flow seems to go directly from Ellesmere Island to the west of the Morris Jesup Spur and bends to an NW-SE direction before getting to the spur due to the transpolar drift flowing toward the Fram Strait. This would mean that the

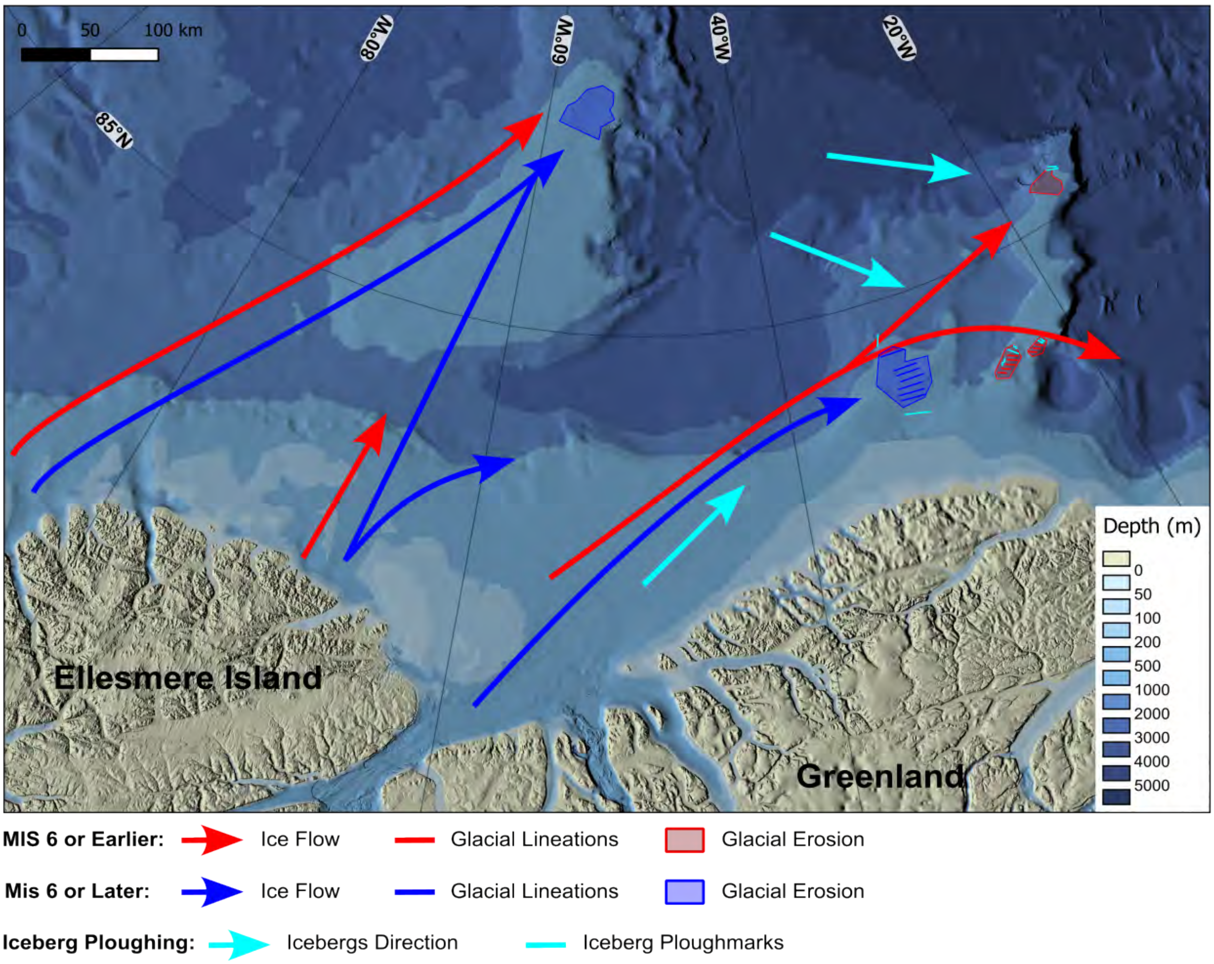


**Figure 22**. Map summarizing the glacial erosion on the southern Lomonosov Ridge off Lincoln Sea and the Morris Jesup Spur (including area at its southwest), and the ice source, direction and age.

Laurentide ice sheet on Ellesmere Island and the Greenland ice sheet flowing to the Lincoln Sea would be the main glaciers feeding the ice shelf that arrives at the Morris Jesup Spur, and not the Greenland ice sheet just in front of the spur since the glacial lineations are basically parallel to the coastline (dark blue and red lines in Fig. 22).

At the west of the Morris Jesup Spur and getting closer to the Amundsen Basin, the hemipelagic drape seems to be reworked by the contour currents that travelled along the continental slope of the AO (Fig. 21). The Voronov Terrace is mainly characterised by turbidites (Fig. 21) probably formed by the arrival of glacigenic debris flows from the trough-mouth fans at the northeastern Greenland margin. The rectangular-shaped depressions (Fig. 14d) found there could be result of the canalisation of the turbidity flows. Similarly, the Nansen Basin is covered by turbidites at the part closer to the Barents Sea, and by distal turbidites interbedded with hemapelagites at the part closer to the Gakkel Ridge (Fig. 15c). In this case, the accumulation of glacigenic debris flows is identified on the continental slope and rise north of the Barents Sea (Figs 15d and 21).

Volcanic ridges like the Gakkel Ridge, and high slope areas are spread throughout the entire study area, and are represented by facies 3b. Thus, the interpretation of these facies changes depending on the geographical situation, but generalizing 3b facies represent high relief scarps, exposed basement, or little to no sediment accumulation (Fig. 21). The explanation of the appearance of these facies has to do with the reflection of the acoustic beam when reaching very inclined and rough seafloor. The roughness could be given simply by the rough nature of volcanic ridges, or by the progressive erosion in steep relief that exposes coarse-grained relict sediments (Damuth, 1978). The inclination prevents the acoustic waves from being reflected towards the receiver, and the irregular seafloor returns hyperbolic echoes, resulting in very faint diffraction hyperbolas overlapping on the seafloor (Fig. 15b; Melles and Kuhn, 1993). It has to be noted that on the troughs between most of the volcanic ridges, turbidites and hemipelagites are identified (Fig. 15b), but those are not shown in the surficial geology map due to the chaotic nature of these areas and the limited data coverage. The turbidites find their way there from the continental shelf that is closer to that part of the ridge, keeping in mind that they do not cross the axis of the ridges (Johnson, 1969).

Many scenarios have been proposed to explain the formation of the regularly spaced parallel to subparallel ridges identified on the Yermak Plateau (Figs 16f, g, h, i, j, and 23a) and interpreted as streamlined subglacial landforms (Batchelor et al., 2016; J. A. Dowdeswell et al., 2010; Gebhardt et al., 2011; Jakobsson et al., 2010; P. R. Vogt et al., 1994). Considering all the previously suggested scenarios and all the available open-source bathymetric and sub-bottom data, I propose the following ice-grounding events as responsible for shaping the landforms assemblage seen today on Yermak Plateau:

1. Grounding of an ice sheet around MIS 19/20. This is shown in the sub-bottom profiles as an erosional unconformity roughly between 600 m and 1000 m water depth at the northeast of the southern ridge crest (red reflector in Fig. 23b), and between 780 and 1000 m at the northeast of the Sverdrup Bank (red reflector in Fig. 23c). It is difficult to infer the direction of the ice mass during this event since in most cases another erosional unconformity is found above. Where unconformities above are not present, a 40-50 m thick layer of acoustically stratified sediments that flattens the seafloor is found, deleting thus the traces of this grounding event from the seafloor. The geotechnical properties of the sediments at this unconformity are compatible with the grounding of an ice sheet (O'Regan et al., 2010), and the sediments just above the unconformity were dated to 790 ka. This unconformity was present in most of the research area of Gebhardt et al. (2011) and was also identified at the south of the Yermak Plateau in this study. Then, all points toward an ice-sheet grounding over almost the entire Yermak Plateau around MIS 19/20.

2. A posterior grounding of ice-shelves remnants around MIS 6. This would be responsible for practically all the regularly spaced parallel to sub-parallel glacial lineations spread all over the Yermak Plateau between 500 and 1060 m deep. In the sub-bottom profiles is shown as an erosional unconformity (dark blue and green reflectors in Figs 23b and c) all over the plateau. At the southern ridge crest, the unconformity is buried under a hemipelagic sediment layer with variable thickness generally increasing with depth, and can be present under a more recent erosional event (light blue reflector in Fig. 23b) or even exposed to the seafloor. At the rest of the Yermak Plateau, from the axis to the outer edge (the side closer to the spreading ridges), the unconformity is buried by a thin layer of hemipelagic sediments or directly exposed to the seafloor (green reflector in Fig. 23c). From the axis of the plateau to the Sophia Basin, the unconformity is again buried by a relatively thick layer of hemipelagic sediments and located in greater water depths compared to the ones on the outer edge of the plateau (dark blue reflector in Fig. 23c). These differences in the thickness of hemipelagic drape over the diamict (unconformity) could mean different grounding events, but Gebhardt et al. (2011) specified that in this case, the difference in thickness was due to difference in sedimentation rates related to the bottom currents, as the Fram Strait and Yermak Plateau are hot-spots regarding the AO circulation. The possibility of the grounding event being caused by an ice sheet during MIS 6 is dismissed since the geotechnical properties of the sediments below the ice-grounding event do not show the overconsolidation expected after a long settling of an ice sheet (O'Regan et al., 2010). The possibility of an ice shelf grounding on the plateau is also dismissed considering that the lineations are not completely straight and parallel in all places, and that between the Sverdrup Bank and the northeast basement high, crosscutting lineations which cannot be explained by the movement of a coherent ice shelf, are identified. Therefore, a feasible scenario is the grounding of remnants of ice shelves. These ice masses would come from the St. Anna and Franz Victoria ice streams in a WSW direction tilting to a SW direction when getting to the southern ridge crest (dark blue glacial lineations in Fig. 23a), and from the central AO ice shelf (Jakobsson, Nilsson,

et al., 2016) in a SSW direction tilting to a S direction when getting to the southern ridge crest (green glacial lineations in Fig. 23a). The asynchronous arrival of ice masses from both sources would explain the crosscutting glacial lineations present at some places of the plateau. In this case, the Sverdrup Bank blocking the ice coming from St. Anna and Franz Victoria ice streams would explain the lack of ENE-WSW oriented lineations at its west. The ice masses from the central AO seem to arrive at the southern ridge crest slightly later and with lower thicknesses, as the N-S oriented lineations there, are only found at lower depths and truncating the NE-SW oriented lineations caused by the ice masses coming from the northern Barents Sea. This hypothesized ice flow would also be supported by the mass transport deposits found in the sub-bottom profiles at the southwest of the Sverdrup Bank, southeastern basement high, and southern ridge crest (Fig. 23a). An MIS 6 age for this event was inferred from cores retrieved from the southern ridge crest (J. A. Dowdeswell et al., 2010; Jakobsson et al., 2010). It is more likely that the lineations were caused by ice shelf remnants and not a coherent mass of icebergs trapped within multi-year sea ice if we date the event to MIS 6. During MIS 6, the AO could be covered by an ice shelf at least on the Amerasia Basin and Lomonosov Ridge (Jakobsson, Nilsson, et al., 2016), then we expect an ice flow similar to that inferred by Hughes et al. (1977) which is in accordance with the glacial lineations. Perhaps the icebergs would follow the West Spitsbergen Current flowing toward Siberia, which would prevent the icebergs from the St. Anna and Franz Victoria ice streams from arriving at the Yermak Plateau.

3. Chaotic deep-keeled and minor icebergs. The area of the southern ridge crest lying above 500 m deep is characterised by a chaotic seafloor interpreted as glacial diamict (light blue reflector in Fig. 23b). These chaotic depressions cannot be identified in the 200 x 200 m grid DBM, but with the 100 x 100 m grid, some of them can be seen. This seems to be caused by single icebergs that reworked the upper sediment layer sometime after MIS 6. The icebergs could be either arriving from the ice streams at the western margins of Svalbard and Barents Sea following the West Spitsbergen Current or directly from the northwestern Svalbard ice sheet. Fine-grained material found in cores from the Yermak Plateau and northwestern Svalbard margin (C. Vogt et al., 2001) supports the idea of icebergs flowing northward from the western Barents Sea ice sheet. The v-shaped depressions found between depths of 500 and 1000 m are likely ploughmarks of single deep-keeled icebergs (light blue in Fig. 23a, c). Here I propose as a possible scenario for the ploughmarks found at the northeast of the Serdrup Bank and southern ridge crest, deep-keeled icebergs drifting southwestward from Franz Victoria and St. Anna ice streams (J. A. Dowdeswell et al., 2010). Icebergs carried by the transpolar drift from the central AO ice shelf (Jakobsson, Nilsson, et al., 2016) or the ice sheets that drain to the AO would explain the ploughmarks found on the central Yermak Plateau. Finally, a possible source for the icebergs that originated the ploughmarks at the southwest of the southern ridge crest would also be the AO. However, instead of grounding directly over the Yermak Plateau, the icebergs would cross the Fram Strait, recirculating and joining the West Spitsbergen Current before grounding on the Yermak Plateau and the western Svalbard margin. (Zhao et al., 2017). Some ploughmarks are buried under hemipelagic drape, meaning that not all these bigger ploughmarks are dated to a post-MIS 6 age. Indeed, at the southwest of the southern ridge crest, ploughmarks buried below the more recent ones described above are identified in the sub-bottom profiles, indicating previous grounding events likely caused by deep-keeled icebergs. It cannot be dismissed that the routes proposed for the deep-keeled icebergs are also valid for minor icebergs.

Note that these are just the hypothesized scenarios recorded in the studied sub-bottom, multibeam, seismic, and coring data, and it does not mean that the Yermak Plateau was not subjected to ice-grounding events during other glacial periods.

Similarly, deep iceberg ploughmarks were identified on the western Svalbard margin between 395 and 980 m deep (Fig. 17c; Zhao et al., 2017) and the Hovgaard Ridge around 1200 m deep (Arndt and Forwick, 2016; Arndt et al., 2014). For the deeper and bigger ploughmarks, the explanation is the same as those of the southwestern Yermak Plateau, coming from the AO, crossing the Fram Strait while grounding on the Hovgaard Ridge (Arndt and Forwick, 2016; Arndt et al., 2014), and finally recirculating and joining the Western Spitsbergen Current before grounding on the western Svalbard margin around MIS 6 (Zhao et al., 2017). The shallower smaller ploughmarks were likely formed by icebergs released from the western Barents Seas ice streams that travelled northward and grounded on the western Svalbard margin (Zhao et al., 2017).

Excluding the Sverdrup Bank, the southeastern basement high, and the northeastern and southwestern parts, the Yermak Plateau is covered by hemipelagic drape, in most cases overlying glacial diamict and without disturbances below (at least) 900 m deep (Fig. 21). The hemipelagic sediments are redistributed by ocean currents in many cases since this area is largely influenced by water exchange between the Arctic and the Atlantic oceans. The areas more affected by water circulation in the Yermak Plateau are the surroundings of the bathymetric highs, an area northwest of the Sverdrup Bank, and the Litke Trough (Figs 16b and 21). As a matter of fact, the West Spitsbergen Current flows just above the Litke Trough (Manley et al., 1992), and the southeastern basement high is surrounded by a curved moat interpreted as an overflow channel also related to the West Spitsbergen Current (J. A. Dowdeswell et al., 2010; P. R. Vogt et al., 1994). Apart from the mass transport deposits associated with the MIS 6 ice grounding previously mentioned, we identified others at the southeast and northeast of the Litke Trough, and at the west of the Sverdrup Bank (Fig. 21). At the southeast of the Litke Trough, the mass transport deposits are a result of glacigenic debris flows from when the northern Svalbard ice sheet arrived at the shelf edge. The others are linked with the downslope flow of turbidity currents. All these commented mass transport deposits are found interbedded with hemipelagic drape.

The surroundings of the Yermak Plateau are mainly governed by hemipelagic sedimentation, and this includes the Sophia Basin (Fig. 21). Nevertheless, the most prominent feature in the Sophia Basin is the traces of the Hinlopen Landslide. These are shown in the sub-bottom data as chaotic hyperbolic seafloor (Fig. 16d), and numerous mega-blocks from the slope failure are identified in the DBM. The mobilised material was even spread out on the Nansen Basin, where chaotic seafloor is identified beyond the connecting point of the Nansen and Sophia basins (Fig. 15a). The staircase-like structures found at the northeast of the Mosby Seamount (Fig. 16c) are deformed hemipelagic drape (Fig. 21) as a consequence of a failure of the sediments during a secondary evacuation phase of the Hinlopen Landslide (Winkelmann et al., 2008).

Most of the continental shelf mapped around Svalbard is characterized by a chaotic seafloor (Figs 16b and 21) similar to that documented by Dowdeswell et al. (1993) on the East Greenland continental shelf. The explanation would then point to icebergs from the Svalbard and Barents Sea ice sheets drifting through cross-shelf troughs and the continental shelf between them. The parts of the continental shelf with a smoother seafloor reflect the difficulties for the icebergs to plough them. Within the cross-shelf troughs, a more complex appearance of the sub-bottom probably reflects the different advances and retreats of the ice streams during distinct glacial periods. Mass transport deposits are identified below the shelf break, and represent glacigenic debris flows that are found interbedded with hemipelagic drape as moving away from the shelf. This area influenced by glacigenic debris flows is very narrow at the northwestern Svalbard margin and it is expanded moving southward (Figs 17b and 21). This is a result of the difference in sediment delivery to the shelf break during past glaciations between the ice streams at the northwestern Svalbard, southwestern Svalbard, and western Barents Sea.

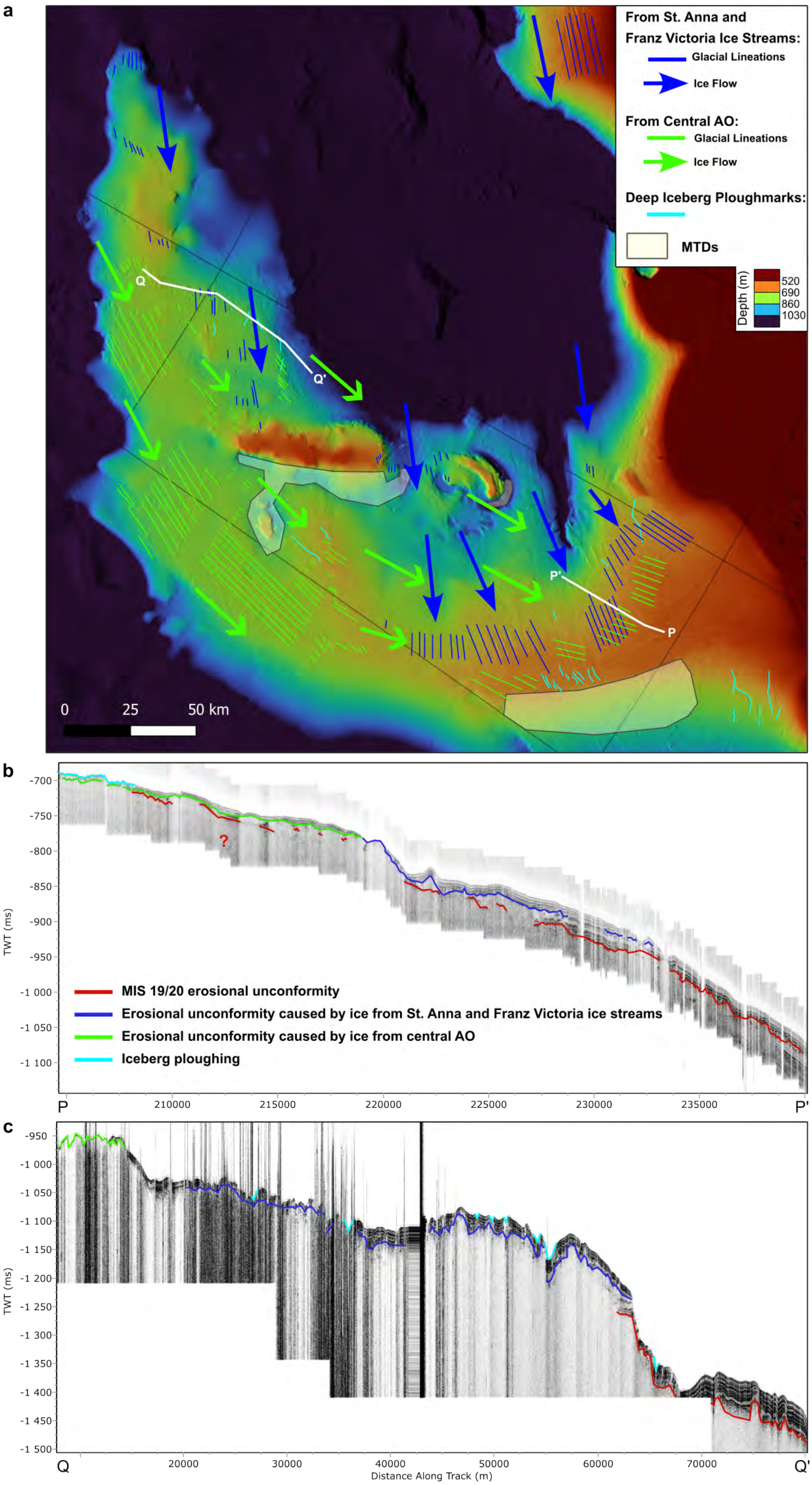


**Figure 23**. (Continued on the following page)

**Figure 23**. Summary of the glacial erosion on the Yermak Plateau and its source. (a) Map of the Yermak Plateau indicating the glacial erosion, ice source, ice direction, and deposits related to this glacial erosion. The sub-bottom profiles between P-P' and Q-Q' are shown in Fig. 23b and c, respectively. Chirp sonar sub-bottom profile from (b) the southern ridge crest and (c) the northeastern area of the Yermak Plateau, showing the distinct erosional unconformities. The location of the profiles between P and P', and between Q and Q' is shown in Fig. 23a. The different erosional unconformities caused by ice grounding are represented by coloured reflectors.

Western Barents Sea margin contains the Kveithola Trough, and the huge Storfjorden and Bear Island trough-mouth fans (Fig. 1), which deliver greater amounts of sediment and spread it over larger areas. These mass transport deposits have been previously documented and interpreted as glacigenic debris flows stacking over the continental slope during successive glacial maxima separated by thin layers of glacimarine and hemipelagic sediments (Damuth, 1978; Laberg and Dowdeswell, 2016; Laberg and Vorren, 1995, 1996; Vorren et al., 1989). The area closest to the Knipovich Ridge is characterised by turbidites (Fig. 21) derived from the distal transport of the glacigenic debris flows that seem to be canalised at some places since a channel is identified here (Fig. 17h). Coming back to the northwestern Svalbard margin, at the east of the Molloy Ridge, hemipelagic drape that might have been reworked by bottom currents covers the region beyond the ice-scoured and debris-flow-influenced areas (Fig. 21). The major depressions found in this area above 980 m deep were explained before and interpreted as iceberg ploughmarks. The other major depressions are found between 1400 (Fig. 17f) and 2400 m deep (Fig. 17d). Even though they might look like iceberg ploughmarks, considering the depth and the geomorphological appearance in the DBM, they are more likely a product of faulting (Fig. 17f) and gravity flows forming submarine channels (Fig. 17d). The minor depressions (Fig. 17e) are found on the top of the Vestnesa Ridge (Fig. 1) in the western Svalbard margin. The Vestnesa Ridge was interpreted as a sediment drift controlled by the bottom currents derived from the West Spitsbergen Current (Howe et al., 2008; P. R. Vogt et al., 1994). Pockmarks (P. R. Vogt et al., 1994) and gas venting (Bünz et al., 2012) have been documented before on the Vestnesa Ridge, therefore these minor depressions can be consistently interpreted as pockmarks associated with venting of methane-rich fluids from gas hydrate and free gas reservoirs (Bünz et al., 2012). Plaza-Faverola et al. (2015) determined multiple seepage periods during the last 2.7 Ma. This deepwater gas hydrate system could also explain the blanking that can be seen in the sub-bottom profiles 40 km to the southeast (Fig. 17g).

The area covering the northern part of the Boreas Abyssal Plain, the Hovgaard Ridge, and the region at its north between the volcanic ridges and the Greenland shelf is governed by hemipelagic drape (Fig. 21). Here, there are some relatively small areas where mass transport deposits are identified in the sub-bottom profiles, the most prominent ones at the foot of the western Hovgaard Ridge. Those are present there truncating the hemipelagic drape, so the gravity flows moving downslope from the ridge crest must be relatively recent and with relatively high strength. They are only mapped at the southwestern part of the ridge and it seems likely that the gravity flows take place all over the ridge slope, but there is lack of data to prove that. As explained above in this section, on the crest of the Hovgaard Ridge, six iceberg ploughmarks and one pit hole, which is explained by a single hit of a rotating giant iceberg, were identified (Arndt and Forwick, 2016). These icebergs scouring the ridge crest could be one of the reasons why we find mass transport deposits at the foot. Two more depressions are identified around 2300 m deep in sub-bottom data at the eastern Greenland-Spitsbergen Sill (Appendix II), and again, the most likely interpretation might be submarine channels and/or little slide scars. The surficial geology of the part of the Boreas Abyssal Plain in contact with the Greenland continental slope and the northwestern East Greenland Ridge is interpreted as turbidites due to the influence of the glacigenic debris flows moving downslope from the northern Norske Trough (Fig. 21). The end basin for these gravity flows is the central Boreas Abyssal Plain though, where really thick layers of turbidites are found interbedding hemipelagites (Figs 18b and 21). Here is where some vertical displacements affecting the complete acoustic stratigraphy are identified (Fig. 18b). These features resemble vertical faults that clearly took place after the deposition of the sediments. The explanation of this is not entirely clear, but it could be a consequence of the Knipovich Ridge tectonism or of the differences in sediment compaction between basement highs and valleys (Duin et al., 1984; Mayer, 1981).

The crest of the East Greenland Ridge is mainly covered by hemipelagic drape even if some parts are interbedded with mass transport deposits and others are current-controlled (Figs 18c and 21). The southeastern part of the East Greenland Ridge seems the be specially influenced by currents due to the sediment waves that we find there, perhaps the deep fraction of the East Greenland Current that recirculates in this area (Rudels and Carmack, 2022). The mass transport material seems to arrive from the shallower parts of the ridge, flowing down along high slopes within and at the flanks of the ridge. The northeastern part of the Greenland Abyssal Plain, which lies at the foot of the East Greenland Ridge, is characterised by a layer of debris flows that extend over turbidites (Figs 19c and 21). This part represents the distal deposition of the turbidites flowing from the continental shelf adjacent to the Greenland Abyssal Plain. The uppermost layer could represent a major glacial sediment input during the Last Glacial Maximum (García et al., 2012). The sub-bottom reflectors generally abut on the East Greenland Ridge flank (Fig. 19c). A plausible explanation could be the subsidence of the sediments formerly onlapping on the flank. Seismic profiles showed that the East Greenland Ridge is bounded by large normal faults to the northeast and the southwest (Døssing et al., 2008), the subsidence would then be related to the activity of the southwestern fault. At the northeastern fault, on the flank of the ridge in contact with the Boreas Abyssal Plain, this subsidence is not as evident but can be still discerned in some profiles. Within this area of the Greenland Abyssal Plain, the sub-bottom reflectors also abut on the flanks of a subtle mound (Fig. 19d). This mound is likely composed of the sediments surrounding it, meaning that it might be formed by uplift in the abyssal plain. The shape of the mound and the blanking in the signal of the sub-bottom profiles suggest that this feature is created by some kind of diapirism. In fact, the morphology and sub-bottom structure of this feature are similar to those of the hummock fields in the Norway Basin and Eastern Island Plateau identified by Vogt (1997) and interpreted as mud diapirism. However, I could not find a clear explanation why at some points of the hummocky field edge, sediments from the abyssal plain subside while at other points they onlap the field. At the easternmost part of the Greenland Abyssal Plain vertical faults similar to those found on the Boreas Abyssal Plain are identified (Fig. 19b), so the explanation would be similar to those. In this case, the uppermost layer of debrites seems to be formed after the faulting event meaning that this event took place before the Last Glacial Maximum. The greater depths of the Greenland Abyssal Plain compared to the Boreas Abyssal Plain, and the thick layers of turbidites in the Boreas Abyssal Plain suggest a higher sediment input to the Boreas Abyssal Plain during subsequent glacial periods.

The central Greenland Abyssal Plain is an extensive turbidite system (Fig. 21) fed by the glacigenic debris flows from the adjacent continental shelf during distinct glacial periods (2012). Indeed, the sub-bottom data from the eastern Greenland continental slope show the stacking of the glacigenic debris flows (Fig. 20b), and in the abyssal plain, a few channels that confined turbidity flows are identified (Fig. 20a). On the continental rise, several mass transport deposits are identified, some of them buried by turbidites and others overlying and deforming the previously deposited turbidites (Fig. 21). The bathymetric elevation present on the continental slope close to the East Greenland Ridge prevents the advance of the glacigenic debris flows, so this area is governed by current-controlled sedimentation (Fig. 21). Alternatively, the bathymetric elevation more to the south suffered the arrival of a mass transport event that eroded the previously deposited sediments (Fig. 20b). The mass transport deposits are covered by a thin layer of hemipelagic drape and turbidites, likely indicating an older age than the Last Glacial Period.

Similarly to the western Svalbard continental shelf, the chaotic seafloor on the northeastern Greenland continental shelf (Figs 20b and 21) is a result of iceberg ploughing. Areas with a thin layer of hemipelagic/glacimarine drape over the diamict (Figs 20b and 21) seem to be protected from iceberg scouring due to its deeper position. Sub-bottom reflectors below the chaotic seafloor (Figs 20b and 21) reflect the advance and retreat of the ice sheet during previous glacial periods.

In summary (Fig. 24), the continental shelves present a chaotic seafloor shaped by the advance and retreat of ancient ice sheets and ice streams, and ancient and recent icebergs. The extension and remnants of the continental shelves (excluding the East Greenland Ridge) also show ice scouring, either caused by the grounding of an ice shelf, ice shelf remnants, coherent iceberg fields trapped within sea ice, single icebergs, or a mixture of them. The deeper parts of these regions are governed by hemipelagic sedimentation that might be redistributed by bottom currents. Other areas characterized by hemipelagic drape include continental slopes with gentle inclination and basins with not much sediment supply from the adjacent slopes. On the continental slopes adjacent to cross-shelf troughs we mainly find glacigenic debris flows, and the mobilised sediment ends up on the abyssal plains in the form of turbidites. Volcanic ridges are found in most of the cases separating the big basins. Some slope failure scars and deposits are identified over the research area, with the most prominent one found on the northern Svalbard shelf.

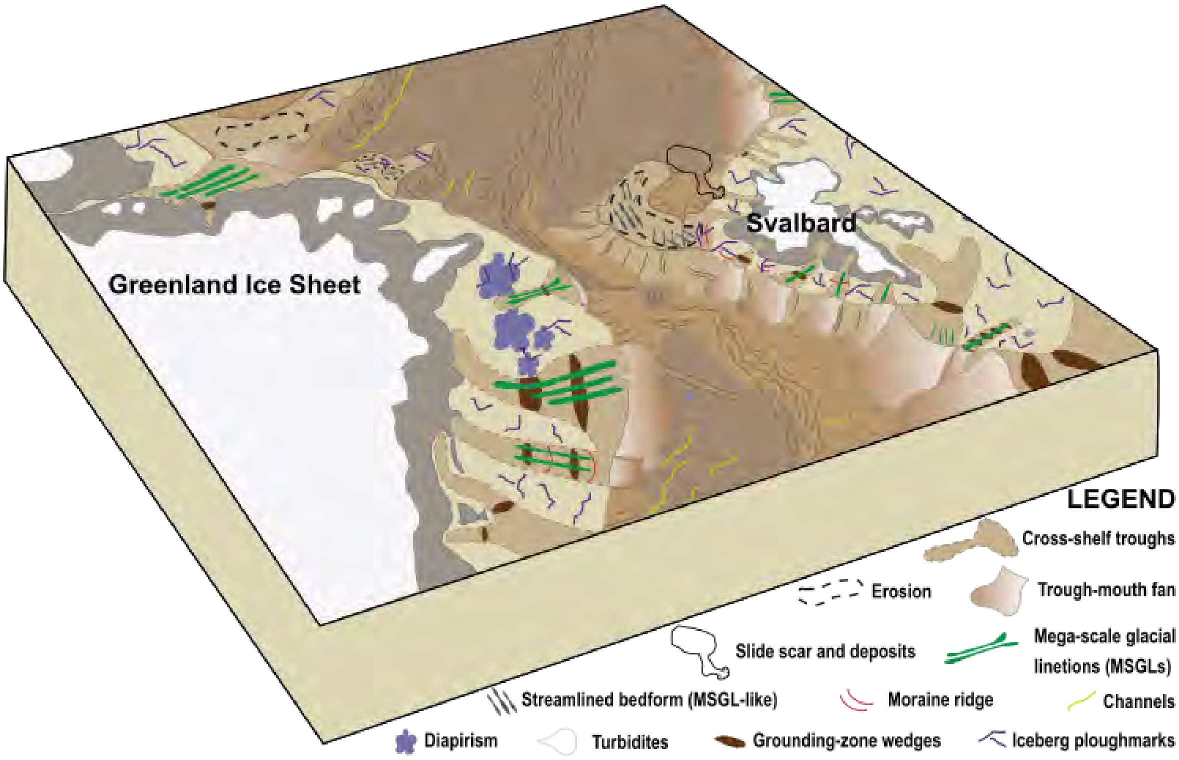


**Figure 24**. Schematic of landform-assemblage and surficial geology for the Fram Strait, and part of the Greenland Sea, Norwegian Sea, Barents Sea and Eurasia Basin of the AO. Modified from Jakobsson (2016).

## 7.3 Limitations and utility of the surficial geology map

The facies type map, created with the extrapolation and interpolation of sub-bottom profiles that were classified according to the characteristics of the seafloor echo and sub-bottom reflections (Fig. 10), provides a general understanding of the appearance of the seafloor and the uppermost sub-bottom. This map was then translated into a surficial geology map (Fig. 21), which provides a general understanding of what we can find in a specific place within the research area. Then, to determine how useful this map can be, a reflexion on the methodological process and its limitations is needed. First of all, this compilation uses sub-bottom profiles acquired with different echo sounders, and also different acquisition settings and environmental conditions during different cruises and within each cruise. These aspects can compromise the data quality and therefore the classification and interpretation of the sub-bottom profiles. Since this study considers data acquired during the last 19 years (33 years if we consider the polygons digitized externally), we need to keep in mind that the ocean is a dynamic environment and some features may have changed or will change from now on, e.g. seismicity, volcanism and slope failure can impact dramatically the seafloor and the sub-bottom within seconds.

The map is a compilation of the sub-bottom data from many expeditions. This means that the expeditions were not designed for the creation of a map like this, so the data density and distribution in many areas are not ideal, dragging uncertainties on the interpolation and extrapolation processes. Another limitation is the DBM used for the digitalization and interpretation of the polygons, which has a grid cell size of 200 x 200 m. Nevertheless, previously published high-resolution bathymetric data and the 100 x 100 m grid DBM from the SAS 2021 expedition improved the interpretation in some areas. Lastly, similarity between different facies can lead to misclassification of the sub-bottom. A clear example of this is the facies 7a and 8a, which in some cases, the decision to classify a polygon as 7a or 8a facies was a result of the hypothesized processes that affect the specific area.

Keeping all the limitations in mind, the surficial geology map seems to serve as a good basis for studies of past and present oceanographic, geologic, and glacial processes. For more detailed studies of the processes that shape and shaped the seafloor and the sub-bottom, additional information such as high-resolution multibeam, coring, and seismic data is needed. Thus, the surficial geology compilation contains the base information for zooming in and out during future studies within the research area. The Subsection 7.2 of this study is an example of this, where the surficial geology map served as the fundamental base for a more insight investigation of processes affecting the different regions of the study area now and in the past.

For offshore development, geohazard risk assessments are needed. Even though there are no established standards and methods to be followed for these assessments, geophysical studies that provide geomorphological and geographical information as well as information about ongoing and past processes are crucial (Moore et al., 2018). A common initial step in the geohazard assessments is a desktop study that integrates all available data of the region of interest in order to provide both a preliminary assessment and support the planning for additional geophysical and geotechnical data acquisition (of Shipping, 2016). Here is where the digitized maps could provide valuable information. The facies type map informs about the appearance of the seafloor and sub-bottom, and the surficial geology map about what to expect to find in a region, and to some extent, the present and past processes there. For example, the polygons called “Mass transport deposits (GDF)” indicate that mass transport material deposited there in the form of glacigenic debris flows, and the polygons called “Glacimarine (draping over diamict)” indicate that the area has been subjected to glacimarine sedimentation after ice grounding events. Indeed, the first version of this map was used for a desktop study regarding the installation of a communication cable across the AO, where a geocost map that considers geometric and process hazards was produced (Jakobsson and Doñate, 2023). The surficial geology map was used then as a base map, where level of risk values regarding the morphology of the seafloor echo (3-highest risk to 1-lowest risk) and the processes hazards (6-ongoing process to 1-recently stable with simple sub-bottom), were assigned to each polygon. The combination of these values, and risk values assigned to the slope with a simple formula, results in a geocost map that indicates the hazard level in the different areas where there is sub-bottom data coverage. The integration of this geocost map, the visual evaluation of the seafloor bathymetry, and the hazards from seismicity resulted in the proposal of three preliminary cable routes and the guidance for future studies and surveys.

Brown et al. (2011) defined benthic habitat mapping as “the use of spatially continuous environmental data sets to represent and predict biological patterns on the seafloor (in a continuous or discontinuous manner)”. One of the most used tools for acquiring spatially continuous environmental data sets is remote sensing, specifically the acoustics, which provide depth (and derived parameters) and backscatter information of the seafloor (Misiuk and Brown, 2024). In that sense, multibeam echo sounding has been primordial for benthic habitat mapping during the last decades, and not as much the sub-bottom profiling. In spite of this, the sub-bottom data could support the interpretation of the multibeam backscatter information, e.g. verifying that low backscatter signals correspond to acoustically stratified sediment in the sub-bottom profiles. In some cases, sub-bottom data could be very valuable since provides information on what is below the seafloor and how this can affect the distribution of species and communities. The surficial geology map also indicates the processes that might be affecting a specific area, and these processes certainly affect the biological distribution, e.g. an area with contourites is most likely subjected to bottom currents, and these currents might favour some kind of organisms or communities over others. Another possible benefit that the surficial geology map would provide is support with the delimitation of the research area and the planning of the ground truthing and high-resolution geophysical survey, e.g. if you are to determine the conservation status of a protected species related to seepage, perhaps you should have a look at the Vestnesa Ridge or the Morris Jesup Spur where pockmarks are found.

In the Environmental Impact Assessment, for the environmental factors likely to be affected by the project, descriptions of the seafloor physiography, geology, and biodiversity need to be included, and as discussed above, the surficial geology map could provide the initial information. In a nutshell, the integration of the IBCAO bathymetric grid (Jakobsson et al., 2020) and derived parameters such as slope and roughness, and IBCAO geology (Boggild et al., 2018; Mosher et al., 2015; van der Krogt, 2018; this study) can serve as a starting point for future research in the AO realm and a useful tool for survey planning. Moreover, the IBCAO grid, the sub-bottom profiles, and (soon) the IBCAO geology are openly available, meaning that people could come back to the source data used for the mapping and thus possess more detailed information and a better understanding of what the map is representing.

# 8 Conclusions

This study gives rise to a surficial geology map of the Eurasia Basin of the AO and the Fram Strait by means of the compilation of sub-bottom profiling data acquired over the past 19 years, primarily with *IB Oden*. While previous regional publications incorporated some of this data, a substantial portion remains uninterpreted, emphasizing the significance of this map. The compilation followed the approach of Boggild et al. (2018), who developed a surficial geology map of the Amerasia Basin. However, the map cannot be digitized solely using sub-bottom profiles. A comprehensive understanding of the seafloor morphology was crucial for understanding the sub-bottom and being able to interpolate and extrapolate within and beyond the SBP survey lines. This understanding was provided by the IBCAO Ver. 4.2 Grid (Jakobsson et al., 2020), a bathymetric model product of the compilation of several datasets, including, but not limited to, multibeam bathymetry.

The surficial geology map has proved to serve as a useful starting point for insight studies of past and recent oceanographic, glacial, and geologic processes affecting a specific region. The data needed to complement the map in the insight studies include high-resolution multibeam bathymetry, sediment coring, and seismic reflection, among others. The map also helps to develop a broader comprehension, linking processes in different regions to understand the interactions within the cryosphere-ocean-sediment system at the AO and its connection to the Atlantic. Similarly, the utility of a surficial geology map for geohazard assessments has been proved, being key for the development of a geocost map used for the proposal of preliminary installation routes of a subsea cable. Although the utility of the surficial geology map for environmental impact assessment and benthic habitat mapping is not as straightforward, there are reasons to support its application. Additionally, planning of future surveys needed to address all aforementioned studies can be largely benefited by the presented map.

Looking ahead, the next step would be to combine this study with the map from the Amerasia Basin, creating thus a unified surficial geology map of the AO. This map would then become part of the IBCAO Geology, a seabed geology layer of the AO that compliments the IBCAO bathymetric grid. The integration of these two layers would provide a comprehensive knowledge of the AO realm. A suggestion for future development of the surficial map is to explore how it can support benthic habitat mapping and environmental impact assessment, and determine if additional data are required to fulfill the needs of these studies.

In terms of areas covered in this study that require more data density, the Amundsen Basin, Yermak Plateau, Morris Jesup Spur, northern Greenland shelf and slope, and Lomonosov Ridge off Ellesmere Island are suggested. Data in the Amundsen Basin are rather dispersed, relying on interpolation and extrapolation over large areas. While the Yermak Plateau has decent data coverage, the complexity of this area asks for improved multibeam coverage. Very packed sea ice has prevented research vessels from accessing the area north of Greenland and Ellesmere Island, including the Lomonosov Ridge and Morris Jesup Spur. This region is critical for understanding past ice dynamics in the central AO, making the potential acquisition of data there highly valuable.

# 9 References

## References


Adler, R. E., Polyak, L., Ortiz, J. D., Kaufman, D. S., Channell, J. E. T., Xuan, C., Grottoli, A. G., Sellén, E., & Crawford, K. A. (2009). Sediment record from the western arctic ocean with an improved late quaternary age resolution: HOTRAX core HLY0503-8jpc, mendeleev ridge. *Global and Planetary Change*, *68*(1), 18–29. https://doi.org/10.1016/j.gloplacha.2009.03.026

Alatarvas, R., O'Regan, M., & Strand, K. (2022). Heavy mineral assemblages of the de long trough and southern lomonosov ridge glacigenic deposits: Implications for the east siberian ice sheet extent. *Climate of the Past*, *18*(8), 1867–1881. https://doi.org/10.5194/cp-18-1867-2022

Amblas, D., Ceramicola, S., Gerber, T. P., Canals, M., Chiocci, F. L., Dowdeswell, J. A., Harris, P. T., Huvenne, V. A., Lai, S. Y., Lastras, G., Iacono, C. L., Micallef, A., Mountjoy, J. J., Paull, C. K., Puig, P., & Sanchez-Vidal, A. (2018). Submarine canyons and gullies. In A. Micallef, S. Krastel, & A. Savini (Eds.), *Submarine geomorphology* (pp. 251–272). Springer International Publishing. Retrieved April 28, 2024, from https://doi.org/10.1007/978-3-319-57852-1_14

Anandakrishnan, S., & Alley, R. B. (1997). Stagnation of ice stream c, west antarctica by water piracy. *Geophysical Research Letters*, *24*(3), 265–268. https://doi.org/10.1029/96GL04016

Andersen, E. S., Dokken, T. M., Elverhøi, A., Solheim, A., & Fossen, I. (1996). Late quaternary sedimentation and glacial history of the western svalbard continental margin. *Marine Geology*, *133*(3), 123–156. https://doi.org/10.1016/0025-3227(96)00022-9

Andreassen, K., Ødegaard, C. M., & Rafaelsen, B. (2007). Imprints of former ice streams, imaged and interpreted using industry three-dimensional seismic data from the southwestern barents sea. *Geological Society, London, Special Publications*, *277*(1), 151–169. https://doi.org/10.1144/GSL.SP.2007.277.01.09

Arndt, J. E., & Forwick, M. (2016). Deep-water iceberg ploughmarks on hovgaard ridge, fram strait. *Geological Society, London, Memoirs*, *46*(1), 285–286. https://doi.org/10.1144/M46.100

Arndt, J. E., Jokat, W., & Dorschel, B. (2017). The last glaciation and deglaciation of the northeast greenland continental shelf revealed by hydro-acoustic data. *Quaternary Science Reviews*, *160*, 45–56. https://doi.org/10.1016/j.quascirev.2017.01.018

Arndt, J. E., Jokat, W., Dorschel, B., Myklebust, R., Dowdeswell, J. A., & Evans, J. (2015). A new bathymetry of the northeast greenland continental shelf: Constraints on glacial and other processes. *Geochemistry, Geophysics, Geosystems*, *16*(10), 3733–3753. https://doi.org/10.1002/2015GC005931

Arndt, J. E., Niessen, F., Jokat, W., & Dorschel, B. (2014). Deep water paleo-iceberg scouring on top of hovgaard ridge–arctic ocean. *Geophysical Research Letters*, *41*(14), 5068–5074. https://doi.org/10.1002/2014GL060267

Atlasov, I. P. (1967). Tectonic map of the arctic and subarctic, scale 1:5 000 000.

Backman, J., Jakobsson, M., Frank, M., Sangiorgi, F., Brinkhuis, H., Stickley, C., O'Regan, M., Løvlie, R., Pälike, H., Spofforth, D., Gattacecca, J., Moran, K., King, J., & Heil, C.

(2008). Age model and core-seismic integration for the cenozoic arctic coring expedition sediments from the lomonosov ridge. *Paleoceanography*, *23*(1). https://doi.org/10.1029/2007PA001476

Backman, J., Jakobsson, M., Løvlie, R., Polyak, L., & Febo, L. A. (2004). Is the central arctic ocean a sediment starved basin? *Quaternary Science Reviews*, *23*(11), 1435–1454. https://doi.org/10.1016/j.quascirev.2003.12.005

Batchelor, C. L., & Dowdeswell, J. A. (2014). The physiography of high arctic cross-shelf troughs. *Quaternary Science Reviews*, *92*, 68–96. https://doi.org/10.1016/j.quascirev.2013.05.025

Batchelor, C. L., Dowdeswell, J. A., Jakobsson, M., Hogan, K. A., & Gebhardt, C. A. (2016). Landform assemblage produced by ice-grounding events on the yermak plateau. *Geological Society, London, Memoirs*, *46*(1), 329–332. https://doi.org/10.1144/M46.169

Batchelor, C. L., Dowdeswell, J. A., & Ottesen, D. (2018). Submarine glacial landforms. In A. Micallef, S. Krastel, & A. Savini (Eds.), *Submarine geomorphology* (pp. 207–234). Springer International Publishing. Retrieved April 28, 2024, from https://doi.org/10.1007/978-3-319-57852-1_12

Batchelor, C. L., Margold, M., Krapp, M., Murton, D. K., Dalton, A. S., Gibbard, P. L., Stokes, C. R., Murton, J. B., & Manica, A. (2019). The configuration of northern hemisphere ice sheets through the quaternary. *Nature Communications*, *10*(1), 3713. https://doi.org/10.1038/s41467-019-11601-2

Beal, M. A. (1969). *Bathymetry and structure of the arctic ocean* [Doctoral dissertation, Oregon State University].

Biscaye, P. E. (1965). Mineralogy and sedimentation of recent deep-sea clay in the atlantic ocean and adjacent seas and oceans. *GSA Bulletin*, *76*(7), 803–832. https://doi.org/10.1130/0016-7606(1965)76[803:MASORD]2.0.CO;2

Bischof, J., Clark, D. L., & Vincent, J.-S. (1996). Origin of ice-rafted debris: Pleistocene paleoceanography in the western arctic ocean. *Paleoceanography*, *11*(6), 743–756. https://doi.org/10.1029/96PA02557

Bischof, J. F., & Darby, D. A. (1997). Mid- to late pleistocene ice drift in the western arctic ocean: Evidence for a different circulation in the past. *Science*, *277*(5322), 74–78. https://doi.org/10.1126/science.277.5322.74

Bjarnadóttir, L. R., Rüther, D. C., Winsborrow, M. C. M., & Andreassen, K. (2013). Grounding-line dynamics during the last deglaciation of kveithola, w barents sea, as revealed by seabed geomorphology and shallow seismic stratigraphy. *Boreas*, *42*(1), 84–107. https://doi.org/10.1111/j.1502-3885.2012.00273.x

Boggild, K., & Mosher, D. C. (2021). Turbidity currents at polar latitudes: A case study of NP-28 channel in the amundsen basin, arctic ocean. *Marine Geology*, *440*, 106571. https://doi.org/10.1016/j.margeo.2021.106571

Boggild, K., Mosher, D. C., Gebhardt, C., Jakobsson, M., Mayer, L. A., Hogan, K., & Dove, D. (2018). Surficial geology of the amerasian basin from subbottom profiler data. *Natural Resources Canada*, (8465). https://doi.org/10.4095/311188

Boggild, K., Mosher, D. C., Travaglini, P., Gebhardt, C., & Mayer, L. (2020). Mass wasting on alpha ridge in the arctic ocean: New insights from multibeam bathymetry and sub-bottom profiler data. *Geological Society, London, Special Publications*, *500*(1), 323–340. https://doi.org/10.1144/SP500-2019-196

Boschen, R. E., Rowden, A. A., Clark, M. R., & Gardner, J. P. A. (2013). Mining of deep-sea seafloor massive sulfides: A review of the deposits, their benthic communities, impacts from mining, regulatory frameworks and management strategies. *Ocean & Coastal Management*, *84*, 54–67. https://doi.org/10.1016/j.ocecoaman.2013.07.005

Bringensparr, C., & Castro, C. (2021). High-resolution bathymetry data from expedition SAS, arctic ocean, 2021. https://doi.org/https://doi.org/10.17043/oden-sas-2021-bathymetry-1

Broecker, W. S. (1975). Floating glacial ice caps in the arctic ocean. *Science*, *188*(4193), 1116–1118. https://doi.org/10.1126/science.188.4193.1116

Brown, C. J., Smith, S. J., Lawton, P., & Anderson, J. T. (2011). Benthic habitat mapping: A review of progress towards improved understanding of the spatial ecology of the seafloor using acoustic techniques. *Estuarine, Coastal and Shelf Science*, *92*(3), 502–520. https://doi.org/10.1016/j.ecss.2011.02.007

Brozena, J., Childers, V., Lawver, L., Gahagan, L., Forsberg, R., Faleide, J., & Eldholm, O. (2003). New aerogeophysical study of the eurasia basin and lomonosov ridge: Implications for basin development. *Geology*, *31*(9), 825–828. https://doi.org/10.1130/G19528.1

Brumley, K. (2014). *Geologic history of the chukchi borderland, arctic ocean* [Doctoral dissertation, Stanford University]. http://purl.stanford.edu/hz857zk1405

Bruvoll, V., Kristoffersen, Y., Coakley, B. J., & Hopper, J. R. (2010). Hemipelagic deposits on the mendeleev and northwestern alpha submarine ridges in the arctic ocean: Acoustic stratigraphy, depositional environment and an inter-ridge correlation calibrated by the ACEX results. *Marine Geophysical Research*, *31*, 149–171. https://doi.org/10.1007/s11001-010-9094-9

Bünz, S., Polyanov, S., Vadakkepuliyambatta, S., Consolaro, C., & Mienert, J. (2012). Active gas venting through hydrate-bearing sediments on the vestnesa ridge, offshore w-svalbard. *Marine Geology*, *332-334*, 189–197. https://doi.org/10.1016/j.margeo.2012.09.012

Burkhanov, V. (1956). *New soviet discoveries in the arctic*. Foreign Languages Publishing House. Moscow.

Camerlenghi, A. (2018). Drivers of seafloor geomorphic change. In A. Micallef, S. Krastel, & A. Savini (Eds.), *Submarine geomorphology* (pp. 135–159). Springer International Publishing. Retrieved April 28, 2024, from https://doi.org/10.1007/978-3-319-57852-1_9

Carmack, E., & Wassmann, P. (2006). Food webs and physical–biological coupling on pan-arctic shelves: Unifying concepts and comprehensive perspectives. *Progress in Oceanography*, *71*(2), 446–477. https://doi.org/10.1016/j.pocean.2006.10.004

Cavalieri, D. J., & Parkinson, C. L. (2012). Arctic sea ice variability and trends, 1979-2010. *The Cryosphere*, *6*(4), 881–889. https://doi.org/10.5194/tc-6-881-2012

Chand, S., Thorsnes, T., Rise, L., Brunstad, H., & Stoddart, D. (2016). Pockmarks in the SW barents sea and their links with iceberg ploughmarks. *Geological Society, London, Memoirs*, *46*(1), 295–296. https://doi.org/10.1144/M46.23

Chand, S., Thorsnes, T., Rise, L., Brunstad, H., Stoddart, D., Bøe, R., Lågstad, P., & Svolsbru, T. (2012). Multiple episodes of fluid flow in the SW barents sea (loppa high) evidenced by gas flares, pockmarks and gas hydrate accumulation. *Earth and Planetary Science Letters*, *331-332*, 305–314. https://doi.org/10.1016/j.epsl.2012.03.021

Cherkis, N. Z., Max, M. D., Vogt, P. R., Crane, K., Midthassel, A., & Sundvor, E. (1999). Large-scale mass wasting on the north spitsbergen continental margin, arctic ocean. *Geo-Marine Letters*, *19*(1), 131–142. https://doi.org/10.1007/s003670050100

CHS. (1979). General bathymetric chart of the oceans (GEBCO) sheet 5.17; map 1:6 000 000. *Canadian Hydrographic Service*.

Clark, C. D. (1994). Large-scale ice-moulding: A discussion of genesis and glaciological significance. *Sedimentary Geology*, *91*(1), 253–268. https://doi.org/10.1016/0037-0738(94)90133-3

Clark, D. L. (1990, January 1). Arctic ocean ice cover; geologic history and climatic significance. In A. Grantz, L. Johnson, & J. F. Sweeney (Eds.), *The arctic ocean region* (p. 0, Vol. 50). Geological Society of America. Retrieved June 6, 2024, from https://doi.org/10.1130/DNAG-GNA-L.53

Coakley, B., Brumley, K., Lebedeva-Ivanova, N., & Mosher, D. (2016). Exploring the geology of the central arctic ocean; understanding the basin features in place and time. *Journal of the Geological Society*, *173*(6), 967–987. https://doi.org/10.1144/jgs2016-082

Cofaigh, C. Ó., Taylor, J., Dowdeswell, J. A., & Pudsey, C. J. (2003). Palaeo-ice streams, trough mouth fans and high-latitude continental slope sedimentation. *Boreas*, *32*(1), 37–55. https://doi.org/10.1080/03009480310001858

Cook, D. B., Fujita, K., & McMullen, C. A. (1986). Present-day plate interactions in northeast asia: North american, eurasian, and okhotsk plates. *Journal of Geodynamics*, *6*(1), 33–51. https://doi.org/10.1016/0264-3707(86)90031-1

Courtney, B. (2009, March 30). *SegyJp2* (Version 1.0). Natural Resources Canada.

Courtney, B. (2015, February 18). *Combine segy* (Version 2.0). Natural Resources Canada.

Courtney, B. (2020, January). *SegyJp2viewer*. Natural Resources Canada.

Damuth, J. E. (1975). Echo character of the western equatorial atlantic floor and its relationship to the dispersal and distribution of terrigenous sediments. *Marine Geology*, *18*(2), 17–45. https://doi.org/10.1016/0025-3227(75)90047-X

Damuth, J. E. (1978). Echo character of the norwegian—greenland sea: Relationship to quaternary sedimentation. *Marine Geology*, *28*(1), 1–36. https://doi.org/10.1016/0025-3227(78)90094-4

Damuth, J. E. (1980). Use of high-frequency (3.5–12 kHz) echograms in the study of near-bottom sedimentation processes in the deep-sea: A review. *Marine Geology*, *38*(1), 51–75. https://doi.org/10.1016/0025-3227(80)90051-1

Darby, D. A., Ortiz, J., Polyak, L., Lund, S., Jakobsson, M., & Woodgate, R. A. (2009). The role of currents and sea ice in both slowly deposited central arctic and rapidly deposited chukchi–alaskan margin sediments. *Global and Planetary Change*, *68*(1), 58–72. https://doi.org/10.1016/j.gloplacha.2009.02.007

Darby, D., Polyak, L., Jakobsson, M., Berger, G., Lövlie, R., Perovich, D., Grenfell, T., Kikuchi, T., & Tateyama, K. (2005). *HLY0503 cruise report*.

De Laski, J. (1864). Glacial action about penobscot bay. *American Journal of Science*, *37*, 335–344.

DeConto, R. M., & Pollard, D. (2016). Contribution of antarctica to past and future sea-level rise. *Nature*, *531*(7596), 591–597. https://doi.org/10.1038/nature17145

Delworth, T. L., Manabe, S., & Stouffer, R. J. (1997). Multidecadal climate variability in the greenland sea and surrounding regions: A coupled model simulation. *Geophysical Research Letters*, *24*(3), 257–260. https://doi.org/10.1029/96GL03927

Developers, I. (2023). *Inkscape* (Version 1.3). https://inkscape.org/

Developers, Q. (2023). *QGIS* (Version 3.32.2-Lima). Free Software Foundation. https://www.qgis.org

Dick, H. J. B., Lin, J., & Schouten, H. (2003). An ultraslow-spreading class of ocean ridge. *Nature*, *426*(6965), 405–412. https://doi.org/10.1038/nature02128

Dietz, R. S., & Shumway, G. (1961). Arctic basin geomorphology. *Geological Society of America Bulletin*, *72*(9), 1319–1329. Retrieved March 7, 2024, from https://jglobal.jst.go.jp/en/detail?JGLOBAL_ID=201602006691090057

Døssing, A., Jackson, H. R., Matzka, J., Einarsson, I., Rasmussen, T. M., Olesen, A. V., & Brozena, J. M. (2013). On the origin of the amerasia basin and the high arctic large igneous province—results of new aeromagnetic data. *Earth and Planetary Science Letters*, *363*, 219–230. https://doi.org/10.1016/j.epsl.2012.12.013

Døssing, A., Dahl-Jensen, T., Thybo, H., Mjelde, R., & Nishimura, Y. (2008). East greenland ridge in the north atlantic ocean: An integrated geophysical study of a continental sliver in a boundary transform fault setting. *Journal of Geophysical Research: Solid Earth*, *113*. https://doi.org/10.1029/2007JB005536

Dove, D., Coakley, B., Hopper, J., Kristoffersen, Y., & HLY0503 Geophysics Team. (2010). Bathymetry, controlled source seismic and gravity observations of the mendeleev ridge; implications for ridge structure, origin, and regional tectonics. *Geophysical Journal International*, *183*(2), 481–502. https://doi.org/10.1111/j.1365-246X.2010.04746.x

Dove, D., Polyak, L., & Coakley, B. (2014). Widespread, multi-source glacial erosion on the chukchi margin, arctic ocean. *Quaternary Science Reviews*, *92*, 112–122. https://doi.org/10.1016/j.quascirev.2013.07.016

Dowdeswell, J. A., Canals, M., Jakobsson, M., Todd, B. J., Dowdeswell, E. K., & Hogan, K. A. (2016a). Introduction: An atlas of submarine glacial landforms. *Geological Society, London, Memoirs*, *46*(1), 3–14. https://doi.org/10.1144/M46.171

Dowdeswell, J. A., Canals, M., Jakobsson, M., Todd, B. J., Dowdeswell, E. K., & Hogan, K. A. (2016b). The variety and distribution of submarine glacial landforms and implications for ice-sheet reconstruction [Publisher: The Geological Society of London]. *Geological Society, London, Memoirs*, *46*(1), 519–552. https://doi.org/10.1144/M46.183

Dowdeswell, J. A., Jakobsson, M., Hogan, K. A., O'Regan, M., Backman, J., Evans, J., Hell, B., Löwemark, L., Marcussen, C., Noormets, R., Ó Cofaigh, C., Sellén, E., & Sölvsten, M. (2010). High-resolution geophysical observations of the yermak plateau and northern svalbard margin: Implications for ice-sheet grounding and deep-keeled icebergs. *Quaternary Science Reviews*, *29*(25), 3518–3531. https://doi.org/10.1016/j.quascirev.2010.06.002

Dowdeswell, J. A., Kenyon, N. H., Elverhøi, A., Laberg, J. S., Hollender, F.-J., Mienert, J., & Siegert, M. J. (1996). Large-scale sedimentation on the glacier-influenced polar north atlantic margins: Long-range side-scan sonar evidence. *Geophysical Research Letters*, *23*(24), 3535–3538. https://doi.org/10.1029/96GL03484

Dowdeswell, J. A., & Ottesen, D. (2016). Current-modified recessional-moraine ridges on the NW spitsbergen shelf. *Geological Society, London, Memoirs*, *46*(1), 255–256. https://doi.org/10.1144/M46.68

Dowdeswell, J. A., Ottesen, D., & Rise, L. (2016). Landforms characteristic of inter-ice stream settings on the norwegian and svalbard continental margins [Publisher: The Geological Society of London]. *Geological Society, London, Memoirs*, *46*(1), 437–444. https://doi.org/10.1144/M46.164

Dowdeswell, J. A., & Todd, B. J. (2016). Mud volcanoes and ice-keel ploughmarks, beaufort sea shelf, arctic canada. *Geological Society, London, Memoirs*, *46*(1), 299–300. https://doi.org/10.1144/M46.102

Dowdeswell, J., Ottesen, D., Evans, J., Cofaigh, C. Ó., & Anderson, J. (2008). Submarine glacial landforms and rates of ice-stream collapse. *Geology*, *36*(10), 819–822. https://doi.org/10.1130/G24808A.1

Dowdeswell, J. A., Ottesen, D., & Rise, L. (2006). Flow switching and large-scale deposition by ice streams draining former ice sheets. *Geology*, *34*(4), 313–316. https://doi.org/10.1130/G22253.1

Dowdeswell, J. A., & Siegert, M. J. (1999). Ice-sheet numerical modeling and marine geophysical measurements of glacier-derived sedimentation on the eurasian arctic continental margins. *GSA Bulletin*, *111*(7), 1080–1097. https://doi.org/10.1130/0016-7606(1999)111<1080:ISNMAM>2.3.CO;2

Dowdeswell, J. A., Villinger, H., Whittington, R. J., & Marienfeld, P. (1993). Iceberg scouring in scoresby sund and on the east greenland continental shelf. *Marine Geology*, *111*(1), 37–53. https://doi.org/10.1016/0025-3227(93)90187-Z

Drachev, S. S. (2011, January 1). Tectonic setting, structure and petroleum geology of the siberian arctic offshore sedimentary basins. In A. M. Spencer, A. F. Embry, D. L. Gautier, A. V. Stoupakova, & K. Sørensen (Eds.), *Arctic petroleum geology* (pp. 369–394, Vol. 35). Geological Society of London. Retrieved March 7, 2024, from https://doi.org/10.1144/M35.25

Duin, E. J. T., Mesdag, C. S., & Kok, P. T. J. (1984). Faulting in madeira abyssal plain sediments. *Marine Geology*, *56*(1), 299–308. https://doi.org/10.1016/0025-3227(84)90021-5

Egiazarov, B. X., Ermakov, A. M., Anikeeva, L. I., Romanovich, B. S., Pol'kin, Y. I., Atlasov, I. P., Demenitskaya, R. M., Garchev, A. F., Karasik, A. M., Kiselev, Y. G., Andreev, S. I., & Kos'ko, M. K. (1977). An explanatory note to a tectonic map of the northern polar area, scale 1:5 000 000. *NIIGA*.

Ehlers, B.-M., & Jokat, W. (2009). Subsidence and crustal roughness of ultra-slow spreading ridges in the northern north atlantic and the arctic ocean. *Geophysical Journal International*, *177*(2), 451–462. https://doi.org/10.1111/j.1365-246X.2009.04078.x

Elverhøi, A., Hooke, R. L., & Solheim, A. (1998). Late cenozoic erosion and sediment yield from the svalbard-barents sea region: Implications for understanding erosion of glacierised basin. *Quaternary Science Reviews*, *17*(1), 209–241. https://doi.org/10.1016/S0277-3791(97)00070-X

Elverhøi, A., Svendsen, J. I., Solheim, A., Andersen, E. S., Milliman, J., Mangerud, J., & Hooke, R. L. (1995). Late quaternary sediment yield from the high arctic svalbard area. *The Journal of Geology*, *103*(1), 1–17. https://doi.org/10.1086/629718

Embry, A. F. (1993). Crockerland — the northwest source area for the sverdrup basin, canadian arctic islands. In T. O. Vorren, E. Bergsager, Ø. A. Dahl-Stamnes, E. Holter, B. Johansen, E. Lie, & T. B. Lund (Eds.), *Arctic geology and petroleum potential* (Norwegian Petroleum Society Special Publication, pp. 205–216, Vol. 2). Elsevier. https://doi.org/10.1016/B978-0-444-88943-0.50018-6

Engels, J. L., Edwards, M. H., Polyak, L., & Johnson, P. D. (2008). Seafloor evidence for ice shelf flow across the alaska–beaufort margin of the arctic ocean. *Earth Surface Processes and Landforms*, *33*(7), 1047–1063. https://doi.org/10.1002/esp.1601

ESRI. (1998). ESRI shapefile technical description. *ESRI White Paper*.

Estrada, S., Koglin, N., Riefstahl, F., Nopper, H., Geissler, W., & Spiegel, C. (2024). Is the yermak plateau a continental fragment from north america? constraints from cretaceous and early eocene magmatic events. *International Journal of Earth Sciences*. https://doi.org/10.1007/s00531-024-02389-8

Evangelatos, J., & Mosher, D. C. (2016). Seismic stratigraphy, structure and morphology of makarov basin and surrounding regions: Tectonic implications. *Marine Geology*, *374*, 1–13. https://doi.org/10.1016/j.margeo.2016.01.013

Feden, R. H., Vogt, P. R., & Fleming, H. S. (1979). Magnetic and bathymetric evidence for the "yermak hot spot" northwest of svalbard in the arctic basin. *Earth and Planetary Science Letters*, *44*(1), 18–38. https://doi.org/10.1016/0012-821X(79)90004-9

Forsyth, D. A., Asudeh, I., Green, A. G., & Jackson, H. R. (1986). Crustal structure of the northern alpha ridge beneath the arctic ocean. *Nature*, *322*(6077), 349–352. https://doi.org/10.1038/322349a0

Forwick, M., & Vorren, T. O. (2010). Stratigraphy and deglaciation of the isfjorden area, spitsbergen. *Norwegian Journal of Geology*, *90*, 163–179.

Fournier, M., Petit, C., Chamot-Rooke, N., Fabbri, O., Huchon, P., Maillot, B., & Lepvrier, C. (2008). Do ridge-ridge-fault triple junctions exist on earth? evidence from the aden-owen-carlsberg junction in the NW indian ocean. *Basin Research*, *20*(4), 575–590. https://doi.org/10.1111/j.1365-2117.2008.00356.x

Franke, D., Hinz, K., & Oncken, O. (2001). The laptev sea rift. *Marine and Petroleum Geology*, *18*(10), 1083–1127. https://doi.org/10.1016/S0264-8172(01)00041-1

Funck, T., Jackson, H. R., & Shimeld, J. (2011). The crustal structure of the alpha ridge at the transition to the canadian polar margin: Results from a seismic refraction experiment. *Journal of Geophysical Research: Solid Earth*, *116*. https://doi.org/10.1029/2011JB008411

Fütterer, D. K. (1992). *ARCTIC 91: Die expedition ARK-VIII/3 mit FS polarstern 1991 (ARCTIC 91: The expedition ARK-VIII/3 of RV polarstern in 1991)* (ISSN: 0176-5027 Num Pages: 267). Bremerhaven, Germany. https://doi.org/10.2312/BzP_0107_1992

Gaina, C., Werner, S. C., Saltus, R., Maus, S., & the CAMP-GM GROUP. (2011). Chapter 3 circum-arctic mapping project: New magnetic and gravity anomaly maps of the arctic. *Geological Society, London, Memoirs*, *35*(1), 39–48. https://doi.org/10.1144/M35.3

García, M., Batchelor, C. L., Dowdeswell, J. A., Hogan, K. A., & Ó Cofaigh, C. (2016). A glacier-influenced turbidite system and associated landform assemblage in the greenland basin and adjacent continental slope. *Geological Society, London, Memoirs*, *46*(1), 461–468. https://doi.org/10.1144/M46.148

García, M., Dowdeswell, J. A., Ercilla, G., & Jakobsson, M. (2012). Recent glacially influenced sedimentary processes on the east greenland continental slope and deep greenland basin. *Quaternary Science Reviews*, *49*, 64–81. https://doi.org/10.1016/j.quascirev.2012.06.016

Garrison, G. R., & Becker, P. (1976). The barrow submarine canyon: A drain for the chukchi sea. *Journal of Geophysical Research (1896-1977)*, *81*(24), 4445–4453. https://doi.org/10.1029/JC081i024p04445

Gasson, E. G. W., DeConto, R. M., Pollard, D., & Clark, C. D. (2018). Numerical simulations of a kilometre-thick arctic ice shelf consistent with ice grounding observations. *Nature Communications*, *9*(1), 1510. https://doi.org/10.1038/s41467-018-03707-w

Gautier, D. L., Bird, K. J., Charpentier, R. R., Grantz, A., Houseknecht, D. W., Klett, T. R., Moore, T. E., Pitman, J. K., Schenk, C. J., Schuenemeyer, J. H., Sørensen, K., Tennyson, M. E., Valin, Z. C., & Wandrey, C. J. (2009). Assessment of undiscovered oil and gas in the arctic. *Science*, *324*(5931), 1175–1179. https://doi.org/10.1126/science.1169467

GEBCO, I. (2024). *Gazetter of undersea features names*. www.gebco.net

Gebhardt, A. C., Jokat, W., Niessen, F., Matthiessen, J., Geissler, W. H., & Schenke, H. W. (2011). Ice sheet grounding and iceberg plow marks on the northern and central yermak plateau revealed by geophysical data. *Quaternary Science Reviews*, *30*(13), 1726–1738. https://doi.org/10.1016/j.quascirev.2011.03.016

Geibert, W., Matthiessen, J., Stimac, I., Wollenburg, J., & Stein, R. (2021). Glacial episodes of a freshwater arctic ocean covered by a thick ice shelf. *Nature*, *590*(7844), 97–102. https://doi.org/10.1038/s41586-021-03186-y

Geissler, W. H., Jokat, W., & Brekke, H. (2011). The yermak plateau in the arctic ocean in the light of reflection seismic data-implication for its tectonic and sedimentary evolution. *Geophysical Journal International*, *187*(3), 1334–1362. https://doi.org/10.1111/j.1365-246X.2011.05197.x

Glebovsky, V. Y., Kaminsky, V. D., Minakov, A. N., Merkur'ev, S. A., Childers, V. A., & Brozena, J. M. (2006). Formation of the eurasia basin in the arctic ocean as inferred from geohistorical analysis of the anomalous magnetic field. *Geotectonics*, *40*(4), 263–281. https://doi.org/10.1134/S0016852106040029

Grantz, A., May, S. D., Taylor, P. T., & Lawver, L. A. (1990). Canada basin. In A. Grantz, L. Johnson, & J. F. Sweeney (Eds.), *The arctic ocean region. the geology of north america* (pp. 379–402, Vol. 50). Geological Society of America.

Grantz, A., Hart, P. E., & Childers, V. A. (2011, January). Geology and tectonic development of the amerasia and canada basins, arctic ocean. In A. M. Spencer, A. F. Embry, D. L. Gautier, A. V. Stoupakova, & K. Sørensen (Eds.), *Arctic petroleum geology* (pp. 771–799, Vol. 35). Geological Society, London, Memoirs. Retrieved March 6, 2024, from https://doi.org/10.1144/M35.50

Haine, T. W. N., Curry, B., Gerdes, R., Hansen, E., Karcher, M., Lee, C., Rudels, B., Spreen, G., de Steur, L., Stewart, K. D., & Woodgate, R. (2015). Arctic freshwater export: Status, mechanisms, and prospects. *Global and Planetary Change*, *125*, 13–35. https://doi.org/10.1016/j.gloplacha.2014.11.013

Hall, J. K. (1990). Chukchi borderland. In A. Grantz, L. Johnson, & J. F. Sweeney (Eds.), *The arctic ocean region. the geology of north america* (pp. 337–350, Vol. 50). Geological Society of America.

Hamann, N. E., Whittaker, R. C., & Stemmerik, L. (2005). Geological development of the northeast greenland shelf. *Geological Society, London, Petroleum Geology Conference Series*, *6*(1), 887–902. https://doi.org/10.1144/0060887

Harrison, J. C., St-Onge, M. R., Petrov, O. V., Strelnikov, S. I., Lopatin, B. G., Wilson, F. H., Tella, S., Paul, D., Lynds, T., Shokalsky, S. P., Hults, C. K., Bergman, S., Jepsen, H. F., & Solli, A. (2011). Geological map of the arctic, map 2159a, scale 1:5 000 000. *Geological Survey of Canada*.

Hays, J. D., Imbrie, J., & Shackleton, N. J. (1976). Variations in the earth's orbit: Pacemaker of the ice ages. *Science*, *194*(4270), 1121–1132. https://doi.org/10.1126/science.194.4270.1121

Hegewald, A., & Jokat, W. (2013). Tectonic and sedimentary structures in the northern chukchi region, arctic ocean. *Journal of Geophysical Research: Solid Earth*, *118*(7), 3285–3296. https://doi.org/10.1002/jgrb.50282

Hein, J. R., Konstantinova, N., Mikesell, M., Mizell, K., Fitzsimmons, J. N., Lam, P. J., Jensen, L. T., Xiang, Y., Gartman, A., Cherkashov, G., Hutchinson, D. R., & Till, C. P. (2017). Arctic deep water ferromanganese-oxide deposits reflect the unique characteristics of the arctic ocean. *Geochemistry, Geophysics, Geosystems*, *18*(11), 3771–3800. https://doi.org/10.1002/2017GC007186

Helwig, J., Kumar, N., & Dinkelman, M. G. (2011, January). Regional seismic interpretation of crustal framework, canadian arctic passive margin, beaufort sea, with comments on petroleum potential. In A. M. Spencer, A. F. Embry, D. L. Gautier, A. V. Stoupakova, & K. Sørensen (Eds.), *Arctic petroleum geology* (pp. 527–543, Vol. 35). Geological Society, London, Memoirs. Retrieved March 6, 2024, from https://doi.org/10.1144/M35.35

Howe, J. A., Shimmield, T. M., Harland, R., & Eyles, N. (2008). Late quaternary contourites and glaciomarine sedimentation in the fram strait. *Sedimentology*, *55*(1), 179–200. https://doi.org/10.1111/j.1365-3091.2007.00897.x

Hughes, T., Denton, G. H., & Grosswald, M. G. (1977). Was there a late-würm arctic ice sheet? *Nature*, *266*(5603), 596–602. https://doi.org/10.1038/266596a0

Hunkins, K. L. (1966). The arctic continental shelf north of alaska. In W. H. Poole (Ed.), *Continental margins and island arcs. geological survey of canada paper, 66-15* (pp. 197–205). Geological Survey of Canada.

(IHO), I. H. O. (2002, October). *Limits of ocean and seas* (S-23, draft, 4th ed.). Monaco.

Imbrie, J., Berger, A., Boyle, E. A., Clemens, S. C., Duffy, A., Howard, W. R., Kukla, G., Kutzbach, J., Martinson, D. G., McIntyre, A., Mix, A. C., Molfino, B., Morley, J. J., Peterson, L. C., Pisias, N. G., Prell, W. L., Raymo, M. E., Shackleton, N. J., & Toggweiler, J. R. (1993). On the structure and origin of major glaciation cycles 2. the 100,000-year cycle. *Paleoceanography*, *8*(6), 699–735. https://doi.org/10.1029/93PA02751

Ingvaldsen, R., Loeng, H., & Asplin, L. (2002). Variability in the atlantic inflow to the barents sea based on a one-year time series from moored current meters. *Continental Shelf Research*, *22*(3), 505–519. https://doi.org/10.1016/S0278-4343(01)00070-X

Ishman, S. E., Polyak, L. V., & Poore, R. Z. (1996). Expanded record of quaternary oceanographic change: Amerasian arctic ocean. *Geology*, *24*(2), 139–142. https://doi.org/10.1130/0091-7613(1996)024<0139:EROQOC>2.3.CO;2

Jackson, H. R., Mudie, P. J., & Blasco, S. M. (1985). *Initial geological report on CESAR: The canadian expedition to study the alpha ridge, arctic ocean*. Canada Geological Survey Paper, 84-22.

Jakobsson, M. (2016). Submarine glacial landform distribution in the central arctic ocean shelf-slope-basin system. *Geological Society, London, Memoirs*, *46*(1), 469–476. https://doi.org/10.1144/M46.179

Jakobsson, M., Grantz, A., Kristoffersen, Y., Macnab, R., MacDonald, R. W., Sakshaug, E., Stein, R., & Jokat, W. (2004). The arctic ocean: Boundary conditions and background information. In R. Stein & R. W. MacDonald (Eds.), *The organic carbon cycle in the arctic ocean* (pp. 1–32). Springer. Retrieved February 20, 2024, from https://doi.org/10.1007/978-3-642-18912-8_1

Jakobsson, M., Gyllencreutz, R., Mayer, L. A., Dowdeswell, J. A., Canals, M., Todd, B. J., Dowdeswell, E. K., Hogan, K. A., & Larter, R. D. (2016). Mapping submarine glacial landforms using acoustic methods. *Geological Society, London, Memoirs*, *46*(1), 17–40. https://doi.org/10.1144/M46.182

Jakobsson, M., & O'Regan, M. (2016). Pockmarks on the mendeleev rise, central arctic ocean. *Geological Society, London, Memoirs*, *46*(1), 297–298. https://doi.org/10.1144/M46.120

Jakobsson, M. (1999). First high-resolution chirp sonar profiles from the central arctic ocean reveal erosion of lomonosov ridge sediments. *Marine Geology*, *158*(1), 111–123. https://doi.org/10.1016/S0025-3227(98)00186-8

Jakobsson, M. (2002). Hypsometry and volume of the arctic ocean and its constituent seas. *Geochemistry, Geophysics, Geosystems*, *3*(5), 1–18. https://doi.org/10.1029/2001GC000302

Jakobsson, M., Andreassen, K., Bjarnadóttir, L. R., Dove, D., Dowdeswell, J. A., England, J. H., Funder, S., Hogan, K., Ingólfsson, Ó., Jennings, A., Krog Larsen, N., Kirchner, N., Landvik, J. Y., Mayer, L., Mikkelsen, N., Möller, P., Niessen, F., Nilsson, J., O'Regan, M., . . . Stein, R. (2014). Arctic ocean glacial history. *Quaternary Science Reviews*, *92*, 40–67. https://doi.org/10.1016/j.quascirev.2013.07.033

Jakobsson, M., Backman, J., Anderson, L., & Björk, G. (2007). A hull mounted multibeam sonar and subbottom profiler on the icebreaker oden.

Jakobsson, M., Backman, J., Rudels, B., Nycander, J., Frank, M., Mayer, L., Jokat, W., Sangiorgi, F., O'Regan, M., Brinkhuis, H., King, J., & Moran, K. (2007). The early miocene onset of a ventilated circulation regime in the arctic ocean. *Nature*, *447*(7147), 986–990. https://doi.org/10.1038/nature05924

Jakobsson, M., & Cherkis, N. (2001). Improvement to the international bathymetric chart of the arctic ocean (IBCAO): Updating the data base and the grid model. *Fall Meeting, American Geophysical Union (AGU)*, *84, Issue 47*. https://scholars.unh.edu/ccom/722

Jakobsson, M., Cherkis, N., Woodward, J., Macnab, R., & Coakley, B. (2000). New grid of arctic bathymetry aids scientists and mapmakers. *Eos, Transactions American Geophysical Union*, *81*(9), 89–96. https://doi.org/10.1029/00EO00059

Jakobsson, M., & Doñate, V. (2023). *Seabed properties and geohazards across the arctic ocean*. Department of Geological Sciences, Stockholm University. Stockholm.

Jakobsson, M., Grantz, A., Kristoffersen, Y., & Macnab, R. (2003). Physiographic provinces of the arctic ocean seafloor. *GSA Bulletin*, *115*(12), 1443–1455. https://doi.org/10.1130/B25216.1

Jakobsson, M., Macnab, R., Mayer, L., Anderson, R., Edwards, M., Hatzky, J., Schenke, H. W., & Johnson, P. (2008). An improved bathymetric portrayal of the arctic ocean: Implications for ocean modeling and geological, geophysical and oceanographic analyses. *Geophysical Research Letters*, *35*(7). https://doi.org/10.1029/2008GL033520

Jakobsson, M., Marcussen, C., & Party, L. S. (2008). *Lomonosov ridge off greenland 2007 (LOMROG) - cruise report* (Special Publication). Geological Survey of Denmark and Greenland. Copenhagen, Denmark.

Jakobsson, M., Mayer, L., Coakley, B., Dowdeswell, J. A., Forbes, S., Fridman, B., Hodnesdal, H., Noormets, R., Pedersen, R., Rebesco, M., Schenke, H. W., Zarayskaya, Y., Accettella, D., Armstrong, A., Anderson, R. M., Bienhoff, P., Camerlenghi, A., Church, I., Edwards, M., . . . Weatherall, P. (2012). The international bathymetric chart of the arctic ocean (IBCAO) version 3.0. *Geophysical Research Letters*, *39*(12). https://doi.org/10.1029/2012GL052219

Jakobsson, M., Mayer, L. A., Bringensparr, C., Castro, C. F., Mohammad, R., Johnson, P., Ketter, T., Accettella, D., Amblas, D., An, L., Arndt, J. E., Canals, M., Casamor, J. L., Chauché, N., Coakley, B., Danielson, S., Demarte, M., Dickson, M.-L., Dorschel, B., . . . Zinglersen, K. B. (2020). The international bathymetric chart of the arctic ocean version 4.0. *Scientific Data*, *7*(1), 176. https://doi.org/10.1038/s41597-020-0520-9

Jakobsson, M., Nilsson, J., O'Regan, M., Backman, J., Löwemark, L., Dowdeswell, J. A., Mayer, L., Polyak, L., Colleoni, F., Anderson, L. G., Björk, G., Darby, D., Eriksson, B., Hanslik, D., Hell, B., Marcussen, C., Sellén, E., & Wallin, Å. (2010). An arctic ocean ice shelf during MIS 6 constrained by new geophysical and geological data. *Quaternary Science Reviews*, *29*(25), 3505–3517. https://doi.org/10.1016/j.quascirev.2010.03.015

Jakobsson, M., Nilsson, J., Anderson, L., Backman, J., Björk, G., Cronin, T. M., Kirchner, N., Koshurnikov, A., Mayer, L., Noormets, R., O'Regan, M., Stranne, C., Ananiev, R., Barrientos Macho, N., Cherniykh, D., Coxall, H., Eriksson, B., Flodén, T., Gemery, L., . . . Semiletov, I. (2016). Evidence for an ice shelf covering the central arctic ocean during the penultimate glaciation. *Nature Communications*, *7*(1), 10365. https://doi.org/10.1038/ncomms10365

Jakobsson, M., Polyak, L., Edwards, M., Kleman, J., & Coakley, B. (2008). Glacial geomorphology of the central arctic ocean: The chukchi borderland and the lomonosov ridge. *Earth Surface Processes and Landforms*, *33*(4), 526–545. https://doi.org/10.1002/esp.1667

Jessen, S. P., Rasmussen, T. L., Nielsen, T., & Solheim, A. (2010). A new late weichselian and holocene marine chronology for the western svalbard slope 30,000–0 cal years BP. *Quaternary Science Reviews*, *29*(9), 1301–1312. https://doi.org/10.1016/j.quascirev.2010.02.020

Joe, Y. J., Polyak, L., Schreck, M., Niessen, F., Yoon, S. H., Kong, G. S., & Nam, S.-I. (2020). Late quaternary depositional and glacial history of the arliss plateau off the east siberian margin in the western arctic ocean. *Quaternary Science Reviews*, *228*, 106099. https://doi.org/10.1016/j.quascirev.2019.106099

Johnson, G. L. (1969). Morphology of the eurasian arctic basin. *Polar Record*, *14*(92), 619–628. https://doi.org/10.1017/S0032247400064901

Jokat, W., Geissler, W., & Voss, M. (2008). Basement structure of the north-western yermak plateau. *Geophysical Research Letters*, *35*(5). https://doi.org/10.1029/2007GL032892

Jokat, W., Uenzelmann-Neben, G., Kristoffersen, Y., & Rasmussen, T. M. (1992). Lomonosov ridge—a double-sided continental margin. *Geology*, *20*(10), 887–890. https://doi.org/10.1130/0091-7613(1992)020<0887:LRADSC>2.3.CO;2

Jokat, W., Weigelt, E., Kristoffersen, Y., Rasmussen, T., & Schone, T. (1995). New insight into the evolution of the lomonosov ridge and the eurasian basin. *Geophysical Journal International*, *122*(2), 378–392.

Jokat, W. (2005). The sedimentary structure of the lomonosov ridge between 88°n and 80°n. *Geophysical Journal International*, *163*(2), 698–726. https://doi.org/10.1111/j.1365-246X.2005.02786.x

Joughin, I., Rignot, E., Rosanova, C. E., Lucchitta, B. K., & Bohlander, J. (2003). Timing of recent accelerations of pine island glacier, antarctica. *Geophysical Research Letters*, *30*(13). https://doi.org/10.1029/2003GL017609

Kashubin, S. N., Petrov, O. V., Poselov, V. A., Shokalsky, S. P., Milshtein, E. D., & Litvinova, T. P. (2021). Deep structures of the circumpolar arctic. In O. V. Petrov & M. Smelror (Eds.), *Tectonics of the arctic* (pp. 29–61). Springer International Publishing. Retrieved March 7, 2024, from https://doi.org/10.1007/978-3-030-46862-0_2

Kim, S., Polyak, L., Joe, Y. J., Niessen, F., Kim, H. J., Choi, Y., Kang, S.-G., Hong, J. K., Nam, S.-I., & Jin, Y. K. (2021). Seismostratigraphic and geomorphic evidence for the glacial history of the northwestern chukchi margin, arctic ocean. *Journal of Geophysical Research: Earth Surface*, *126*(4), e2020JF006030. https://doi.org/10.1029/2020JF006030

Kimball, S., Mattis, P., & Team, G. D. (2021). *GIMP* (Version 2.10.28). https://inkscape.org/

Klemperer, S., Miller, E., Grantz, A., & Scholl, D. (2002, January 1). Crustal structure of the bering and chukchi shelves: Deep seismic reflection profiles across the north american continent between alaska and russia. In E. L. Miller, A. Grantz, & S. Klemperer (Eds.), *Tectonic evolution of the bering shelf–chukchi sea—arctic margin and adjacent landmasses* (pp. 1–24). Geological Society of America. https://doi.org/10.1130/0-8137-2360-4.1

Kongsberg. (2019, May 27). *KM SBP* (Version 1.8.0).

Kravchishina, M. D., Lein, A. Y., Savvichev, A. S., Reykhard, L. E., Dara, O. M., & Flint, M. V. (2017). Authigenic mg-calcite at a cold methane seep site in the laptev sea. *Oceanology*, *57*(1), 174–191. https://doi.org/10.1134/S0001437017010064

Kristoffersen, Y., Coakley, B., Jokat, W., Edwards, M., Brekke, H., & Gjengedal, J. (2004). Seabed erosion on the lomonosov ridge, central arctic ocean: A tale of deep draft icebergs in the eurasia basin and the influence of atlantic water inflow on iceberg motion? *Paleoceanography*, *19*(3). https://doi.org/10.1029/2003PA000985

Kristoffersen, Y., Ohta, Y., & Hall, J. K. (2020). On the the origin of the yermak plateau north of svalbard, arctic ocean. *100*(1), 1–33. https://doi.org/https://dx.doi.org/10.17850/njg100-1-5

Kutschale, H. (1966). Arctic ocean geophysical studies: The southern half of the siberian basin. *Geophysics*, *21*, 683–709.

Kwok, R. (2018). Arctic sea ice thickness, volume, and multiyear ice coverage: Losses and coupled variability (1958–2018). *Environmental Research Letters*, *13*(10), 105005. https://doi.org/10.1088/1748-9326/aae3ec

Laberg, J. S., & Dowdeswell, J. A. (2016). Glacigenic debris-flows on the bear island trough-mouth fan, barents sea margin. *Geological Society, London, Memoirs*, *46*(1), 367–368. https://doi.org/10.1144/M46.77

Laberg, J. S., & Vorren, T. O. (1995). Late weichselian submarine debris flow deposits on the bear island trough mouth fan. *Marine Geology*, *127*(1), 45–72. https://doi.org/10.1016/0025-3227(95)00055-4

Laberg, J. S., & Vorren, T. O. (1996). The glacier-fed fan at the mouth of storfjorden trough, western barents sea: A comparative study. *Geologische Rundschau*, *85*(2), 338–349. https://doi.org/10.1007/BF02422239

Laberg, J. S., & Vorren, T. O. (2000). The trænadjupet slide, offshore norway — morphology, evacuation and triggering mechanisms. *Marine Geology*, *171*(1), 95–114. https://doi.org/10.1016/S0025-3227(00)00112-2

Laberg, J. S., Forwick, M., & Husum, K. (2017). New geophysical evidence for a revised maximum position of part of the NE sector of the greenland ice sheet during the last glacial maximum. *arktos*, *3*(1), 3. https://doi.org/10.1007/s41063-017-0029-4

Läderach, C., Schlindwein, V., Schenke, H.-W., & Jokat, W. (2011). Seismicity and active tectonic processes in the ultra-slow spreading lena trough, arctic ocean. *Geophysical Journal International*, *184*(3), 1354–1370. https://doi.org/10.1111/j.1365-246X.2010.04926.x

Lawver, L. A., & Müller, R. D. (1994). Iceland hotspot track. *Geology*, *22*(4), 311–314. https://doi.org/10.1130/0091-7613(1994)022<0311:IHT>2.3.CO;2

Laxon, S., & McAdoo, D. (1994). Arctic ocean gravity field derived from ERS-1 satellite altimetry. *Science*, *265*(5172), 621–624. https://doi.org/10.1126/science.265.5172.621

Lebedeva-Ivanova, N. N., Zamansky, Y. Y., Langinen, A. Y., & Sergeyev, M. B. (2006). Seismic model of the earth's crust along the "east-siberian continental margin–podvodnikov basin–arlis rise" geotraverse (arctic ocean). In R. A. Scott & D. K. Thurston (Eds.), *Proceedings of the fourth international conference on arctic margins, OCS study MMS 2006-003* (pp. 132–135). US Department of the Interior.

Leblond, P. H. (1980). On the surface circulation in some channels of the canadian arctic archipelago. *Arctic*, *33*(1), 189–197. Retrieved May 10, 2024, from https://www.jstor.org/stable/40509282

Lehmann, C., Jokat, W., & Coakley, B. (2022). Glacial sediments on the outer chukchi shelf and chukchi borderland in seismic reflection data. *Marine Geophysical Research*, *43*(3), 33. https://doi.org/10.1007/s11001-022-09497-7

Lein, A. Y. (2004). Authigenic carbonate formation in the ocean. *Lithology and Mineral Resources*, *39*(1), 1–30. https://doi.org/10.1023/B:LIMI.0000010767.52720.8f

López-Quirós, A., Junna, T., Davies, J., Andresen, K. J., Nielsen, T., Haghipour, N., Wacker, L., Olsen Alstrup, A. K., Munk, O. L., Rasmussen, T. L., Pearce, C., & Seidenkrantz, M.-S. (2024). Retreat patterns and dynamics of the former norske trough ice stream (NE greenland): An integrated geomorphological and sedimentological approach. *Quaternary Science Reviews*, *325*, 108477. https://doi.org/10.1016/j.quascirev.2023.108477

Löwemark, L., O'Regan, M., Hanebuth, T. J. J., & Jakobsson, M. (2012). Late quaternary spatial and temporal variability in arctic deep-sea bioturbation and its relation to mn cycles. *Palaeogeography, Palaeoclimatology, Palaeoecology*, *365-366*, 192–208. https://doi.org/10.1016/j.palaeo.2012.09.028

Lucchi, R. G., Camerlenghi, A., Rebesco, M., Colmenero-Hidalgo, E., Sierro, F. J., Sagnotti, L., Urgeles, R., Melis, R., Morigi, C., Bárcena, M. .-., Giorgetti, G., Villa, G., Persico, D., Flores, J. .-., Rigual-Hernández, A. S., Pedrosa, M. T., Macri, P., & Caburlotto, A. (2013). Postglacial sedimentary processes on the storfjorden and kveithola trough mouth fans: Significance of extreme glacimarine sedimentation. *Global and Planetary Change*, *111*, 309–326. https://doi.org/10.1016/j.gloplacha.2013.10.008

MacAyeal, D. R. (1993). Binge/purge oscillations of the laurentide ice sheet as a cause of the north atlantic's heinrich events. *Paleoceanography*, *8*(6), 775–784. https://doi.org/10.1029/93PA02200

Macinnis, J. B., & Weber, J. R. (1980). LOREX expedition. *Canadian Geographic*, *100*(6), 18–31.

Manley, T. O., Bourke, R. H., & Hunkins, K. L. (1992). Near-surface circulation over the yermak plateau in northern fram strait. *Journal of Marine Systems*, *3*(1), 107–125. https://doi.org/10.1016/0924-7963(92)90033-5

März, C., Stratmann, A., Matthiessen, J., Meinhardt, A. .-., Eckert, S., Schnetger, B., Vogt, C., Stein, R., & Brumsack, H. .-. (2011). Manganese-rich brown layers in arctic ocean sediments: Composition, formation mechanisms, and diagenetic overprint. *Geochimica et Cosmochimica Acta*, *75*(23), 7668–7687. https://doi.org/10.1016/j.gca.2011.09.046

Mayer, L. (1981). Erosional troughs in deep-sea carbonates and their relationship to basement structure. *Marine Geology*, *39*(1), 59–80. https://doi.org/10.1016/0025-3227(81)90028-1

Melles, M., & Kuhn, G. (1993). Sub-bottom profiling and sedimentological studies in the southern weddell sea, antarctica: Evidence for large-scale erosional/depositional processes. *Deep Sea Research Part I: Oceanographic Research Papers*, *40*(4), 739–760. https://doi.org/10.1016/0967-0637(93)90069-F

Menard, H. W., & Smith, S. M. (1966). Hypsometry of ocean basin provinces. *Journal of Geophysical Research (1896-1977)*, *71*(18), 4305–4325. https://doi.org/10.1029/JZ071i018p04305

Mercer, J. H. (1970). A former ice sheet in the arctic ocean? *Palaeogeography, Palaeoclimatology, Palaeoecology*, *8*(1), 19–27. https://doi.org/10.1016/0031-0182(70)90076-3

Mienert, J. (2004). COSTA—continental slope stability: Major aims and topics. *Marine Geology*, *213*(1), 1–7. https://doi.org/10.1016/j.margeo.2004.10.025

Misiuk, B., & Brown, C. J. (2024). Benthic habitat mapping: A review of three decades of mapping biological patterns on the seafloor. *Estuarine, Coastal and Shelf Science*, *296*, 108599. https://doi.org/10.1016/j.ecss.2023.108599

Mohrig, D., & Marr, J. G. (2003). Constraining the efficiency of turbidity current generation from submarine debris flows and slides using laboratory experiments. *Marine and Petroleum Geology*, *20*(6), 883–899. https://doi.org/10.1016/j.marpetgeo.2003.03.002

Moore, R., Davis, G., & Dabson, O. (2018). Applied geomorphology and geohazard assessment for deepwater development. In A. Micallef, S. Krastel, & A. Savini (Eds.), *Submarine geomorphology* (pp. 459–479). Springer International Publishing. Retrieved July 6, 2024, from https://doi.org/10.1007/978-3-319-57852-1_23

Moran, K., Backman, J., Brinkhuis, H., Clemens, S. C., Cronin, T., Dickens, G. R., Eynaud, F., Gattacceca, J., Jakobsson, M., Jordan, R. W., Kaminski, M., King, J., Koc, N., Krylov, A., Martinez, N., Matthiessen, J., McInroy, D., Moore, T. C., Onodera, J., . . . Kristoffersen, Y. (2006). The cenozoic palaeoenvironment of the arctic ocean. *Nature*, *441*(7093), 601–605. https://doi.org/10.1038/nature04800

Mosher, D. C., Courtney, R. C., Jakobsson, M., Gebhardt, C., & Mayer, L. (2015). Mapping the surficial geology of the arctic ocean: A layer for the IBCAO. https://doi.org/10.4043/25561-MS

Mosher, D. C., Shimeld, J., Hutchinson, D., Chian, D., Lebedova-Ivanova, N., & Jackson, R. (2012). Canada basin revealed. https://doi.org/10.4043/23797-MS

Mosher, D. C., Shimeld, J. W., Travaglini, P., & Eert, J. (2018, November 19). *2014 canadian expedition to the north pole, arctic ocean, expedition report* (No. 8493). Geological Survey of Canada. Retrieved November 4, 2024, from https://doi.org/10.4095/313021

Mosher, D. C., Moran, K., & Hiscott, R. N. (1994). Late quaternary sediment, sediment mass flow processes and slope stability on the scotian slope, canada. *Sedimentology*, *41*(5), 1039–1061. https://doi.org/10.1111/j.1365-3091.1994.tb01439.x

Mosola, A. B., & Anderson, J. B. (2006). Expansion and rapid retreat of the west antarctic ice sheet in eastern ross sea: Possible consequence of over-extended ice streams? *Quaternary Science Reviews*, *25*(17), 2177–2196. https://doi.org/10.1016/j.quascirev.2005.12.013

Mudelsee, M., & Raymo, M. E. (2005). Slow dynamics of the northern hemisphere glaciation. *Paleoceanography*, *20*(4). https://doi.org/10.1029/2005PA001153

Münchow, A., Melling, H., & Falkner, K. K. (2006). An observational estimate of volume and freshwater flux leaving the arctic ocean through nares strait. *Journal of Physical Oceanography*, *36*(11), 2025–2041. https://doi.org/10.1175/JPO2962.1

Nansen, F. (1902). Oceanography of the north polar basin. In *The norwegian north polar expedition 1893-1896 scientific results*.

Niessen, F., Hong, J. K., Hegewald, A., Matthiessen, J., Stein, R., Kim, H., Kim, S., Jensen, L., Jokat, W., Nam, S.-I., & Kang, S.-H. (2013). Repeated pleistocene glaciation of the east siberian continental margin. *Nature Geoscience*, *6*(10), 842–846. https://doi.org/10.1038/ngeo1904

Nilsson, J., Jakobsson, M., Borstad, C., Kirchner, N., Björk, G., Pierrehumbert, R. T., & Stranne, C. (2017). Ice-shelf damming in the glacial arctic ocean: Dynamical regimes of a basin-covering kilometre-thick ice shelf. *The Cryosphere*, *11*(4), 1745–1765. https://doi.org/10.5194/tc-11-1745-2017

Nordahl, B., Harrison, C. J., Jarna, A., & Solli, A. (2016). Metal and mineral deposits of the arctic, scale 1:10m. *Geological Survey of Norway*.

Nørgaard-Pedersen, N., Mikkelsen, N., & Kristoffersen, Y. (2007). Arctic ocean record of last two glacial-interglacial cycles off north greenland/ellesmere island — implications for glacial history. *Marine Geology*, *244*(1), 93–108. https://doi.org/10.1016/j.margeo.2007.06.008

Nørgaard-Pedersen, N., Spielhagen, R. F., Thiede, J., & Kassens, H. (1998). Central arctic surface ocean environment during the past 80,000 years. *Paleoceanography*, *13*(2), 193–204. https://doi.org/10.1029/97PA03409

Nøst, O., & Isachsen, P. (2003). The large-scale time-mean ocean circulation in the nordic seas and arctic ocean estimated from simplified dynamics. *Journal of Marine Research*, *61*(2). https://elischolar.library.yale.edu/journal_of_marine_research/7

Nürnberg, D., Wollenburg, I., Dethleff, D., Eicken, H., Kassens, H., Letzig, T., Reimnitz, E., & Thiede, J. (1994). Sediments in arctic sea ice: Implications for entrainment, transport and release. *Marine Geology*, *119*(3), 185–214. https://doi.org/10.1016/0025-3227(94)90181-3

of Shipping, A. B. (2016). *Guidance notes on subsea pipeline route determination*. American Bureau of Shipping. Houston.

Olsen, I. L., Rydningen, T. A., Forwick, M., Laberg, J. S., & Husum, K. (2020). Last glacial ice sheet dynamics offshore NE greenland – a case study from store koldewey trough. *The Cryosphere*, *14*(12), 4475–4494. https://doi.org/10.5194/tc-14-4475-2020

O'Regan, M., Backman, J., Barrientos, N., Cronin, T. M., Gemery, L., Kirchner, N., Mayer, L. A., Nilsson, J., Noormets, R., Pearce, C., Semiletov, I., Stranne, C., & Jakobsson, M. (2017). The de long trough: A newly discovered glacial trough on the east siberian continental margin. *Climate of the Past*, *13*(9), 1269–1284. https://doi.org/10.5194/cp-13-1269-2017

O'Regan, M., Jakobsson, M., & Kirchner, N. (2010). Glacial geological implications of overconsolidated sediments on the lomonosov ridge and yermak plateau. *Quaternary Science Reviews*, *29*(25), 3532–3544. https://doi.org/10.1016/j.quascirev.2010.09.009

O'Regan, M., King, J., Backman, J., Jakobsson, M., Pälike, H., Moran, K., Heil, C., Sakamoto, T., Cronin, T. M., & Jordan, R. W. (2008). Constraints on the pleistocene chronology of sediments from the lomonosov ridge. *Paleoceanography*, *23*(1). https://doi.org/10.1029/2007PA001551

Ottesen, D., & Dowdeswell, J. A. (2009). An inter–ice-stream glaciated margin: Submarine landforms and a geomorphic model based on marine-geophysical data from svalbard. *GSA Bulletin*, *121*(11), 1647–1665. https://doi.org/10.1130/B26467.1

Ottesen, D., Dowdeswell, J. A., Landvik, J. Y., & Mienert, J. (2007). Dynamics of the late weichselian ice sheet on svalbard inferred from high-resolution sea-floor morphology. *Boreas*, *36*(3), 286–306. https://doi.org/10.1111/j.1502-3885.2007.tb01251.x

Parsons, J. D., Friedrichs, C. T., Traykovski, P. A., Mohrig, D., Imran, J., Syvitski, J. P. M., Parker, G., Puig, P., Buttles, J. L., & García, M. H. (2007). The mechanics of marine sediment gravity flows. In *Continental margin sedimentation* (pp. 275–337). John Wiley & Sons, Ltd. Retrieved April 28, 2024, from https://onlinelibrary.wiley.com/doi/abs/10.1002/9781444304398.ch6

Pease, V., Drachev, S., Stephenson, R., & Zhang, X. (2014). Arctic lithosphere — a review. *Tectonophysics*, *628*, 1–25. https://doi.org/10.1016/j.tecto.2014.05.033

Pedrosa, M. T., Camerlenghi, A., De Mol, B., Urgeles, R., Rebesco, M., & Lucchi, R. G. (2011). Seabed morphology and shallow sedimentary structure of the storfjorden and kveithola trough-mouth fans (north west barents sea). *Marine Geology*, *286*(1), 65–81. https://doi.org/10.1016/j.margeo.2011.05.009

Petrov, O. V., Kashubin, S. N., Shokalsky, S. P., Sokolov, S. D., Petrov, E. O., & Tuchkova, M. I. (2021). Tectonic model and evolution of the arctic. In O. V. Petrov & M. Smelror (Eds.), *Tectonics of the arctic* (pp. 187–208). Springer International Publishing. Retrieved March 7, 2024, from https://doi.org/10.1007/978-3-030-46862-0_8

Petrov, O. V., Pubellier, M., Shokalsky, S. P., Morozov, A. F., Kazmin, Y. B., Kashubin, S. N., Vernikovsky, V. A., Smelror, M., Brekke, H., Kaminsky, V. D., & Pospelov, I. I. (2021). New tectonic map of the arctic. In O. V. Petrov & M. Smelror (Eds.), *Tectonics of the arctic* (pp. 1–27). Springer International Publishing. Retrieved March 7, 2024, from https://doi.org/10.1007/978-3-030-46862-0_1

Petrov, O. V., Shokalsky, S. P., Kashubin, S. N., Morozov, A. F., Sobolev, N. N., Pospelov, I. I., Box, S., Brekke, H., Ernst, R., Faleide, Y., Gaedicke, C., Gaina, C., Gernigol, L., Glumov, I. F., Grantz, A., Grikurov, G. E., Guarnieri, P., Harrison, J. C., Kaminsky, V. D., . . . Vernikovsky, V. A. (2019). Tectonic map of the arctic, scale 1:10 000 000.

Petrov, O. V., & Smelror, M. (2007). Uniting the arctic. *GeoExrpo*, *4*(4), 46.

Petrov, O. V., Smelror, M., & Morozov, A. F. (2016). *International project: Atlas of geological maps of the circumpolar arctic*. VSEGEI Publishing House.

Petrov, O., & Smelror, M. (2015). Uniting the arctic frontiers – international cooperation on circum-arctic geological and geophysical maps. *Polar Record*, *51*(5), 530–535. https://doi.org/10.1017/S0032247414000667

Phillips, R. L., & Grantz, A. (2001). Regional variations in provenance and abundance of ice-rafted clasts in arctic ocean sediments: Implications for the configuration of late quaternary oceanic and atmospheric circulation in the arctic. *Marine Geology*, *172*(1), 91–115. https://doi.org/10.1016/S0025-3227(00)00101-8

Piper, D. J., & Normark, W. R. (2009). Processes that initiate turbidity currents and their influence on turbidites: A marine geology perspective. *Journal of Sedimentary Research*, *79*(6), 347–362. https://doi.org/10.2110/jsr.2009.046

Plaza-Faverola, A., Bünz, S., Johnson, J. E., Chand, S., Knies, J., Mienert, J., & Franek, P. (2015). Role of tectonic stress in seepage evolution along the gas hydrate-charged vestnesa ridge, fram strait. *Geophysical Research Letters*, *42*(3), 733–742. https://doi.org/10.1002/2014GL062474

Poirier, A., & Hillaire-Marcel, C. (2009). Os-isotope insights into major environmental changes of the arctic ocean during the cenozoic. *Geophysical Research Letters*, *36*(11). https://doi.org/10.1029/2009GL037422

Polyak, L., Curry, W. B., Darby, D. A., Bischof, J., & Cronin, T. M. (2004). Contrasting glacial/interglacial regimes in the western arctic ocean as exemplified by a sedimentary record from the mendeleev ridge. *Palaeogeography, Palaeoclimatology, Palaeoecology*, *203*(1), 73–93. https://doi.org/10.1016/S0031-0182(03)00661-8

Polyak, L., Bischof, J., Ortiz, J. D., Darby, D. A., Channell, J. E. T., Xuan, C., Kaufman, D. S., Løvlie, R., Schneider, D. A., Eberl, D. D., Adler, R. E., & Council, E. A. (2009). Late quaternary stratigraphy and sedimentation patterns in the western arctic ocean. *Global and Planetary Change*, *68*(1), 5–17. https://doi.org/10.1016/j.gloplacha.2009.03.014

Polyak, L., Edwards, M. H., Coakley, B. J., & Jakobsson, M. (2001). Ice shelves in the pleistocene arctic ocean inferred from glaciogenic deep-sea bedforms. *Nature*, *410*(6827), 453–457. https://doi.org/10.1038/35068536

Polyak, L., & Jakobsson, M. (2011). Quaternary sedimentation in the arctic ocean: RECENT ADVANCES AND FURTHER CHALLENGES. *Oceanography*, *24*(3), 52–64. Retrieved April 28, 2024, from https://www.jstor.org/stable/24861298

Powell, R. D., & Molnia, B. F. (1989). Glacimarine sedimentary processes, facies and morphology of the south-southeast alaska shelf and fjords. *Marine Geology*, *85*(2), 359–390. Retrieved April 9, 2024, from https://pubs.usgs.gov/publication/70015388

Powell, R., & Domack, G. W. (2002, January 1). Modern glaciomarine environments. In J. Menzies (Ed.), *Modern and past glacial environments* (pp. 361–389). Butterworth-Heinemann. Retrieved April 28, 2024, from https://www.sciencedirect.com/science/article/pii/B9780750642262500155

Powell, R. D. (1990). Glacimarine processes at grounding-line fans and their growth to ice-contact deltas. *Geological Society, London, Special Publications*, *53*(1), 53–73. https://doi.org/10.1144/GSL.SP.1990.053.01.03

Powell, R. D., & Alley, R. B. (1997). Grounding-line systems: Processes, glaciological inferences and the stratigraphic record. In *Geology and seismic stratigraphy of the antarctic margin, 2* (pp. 169–187). American Geophysical Union (AGU). Retrieved April 28, 2024, from https://onlinelibrary.wiley.com/doi/abs/10.1029/AR071p0169

Pratson, L. F., Imran, J., Parker, G., Syvitski, J. P. M., & Hutton, E. (2000, January 1). Debris flows vs. turbidity currents: A modeling comparison of their dynamics and deposits. In A. H. Bouma & C. G. Stone (Eds.), *Fine-grained turbidite systems* (p. 0, Vol. 72). American Association of Petroleum Geologists. Retrieved April 28, 2024, from https://doi.org/10.1306/M72703C6

Raymo, M. E. (1994). The initiation of northern hemisphere glaciation. *Annu. Rev. Earth Planet. Sci*, *22*, 353–383.

Razmjooei, M. J., Henderiks, J., Coxall, H. K., Baumann, K.-H., Vermassen, F., Jakobsson, M., Niessen, F., & O'Regan, M. (2023). Revision of the quaternary calcareous nannofossil biochronology of arctic ocean sediments. *Quaternary Science Reviews*, *321*, 108382. https://doi.org/10.1016/j.quascirev.2023.108382

Rebesco, M. (2005, January 1). Contourites. In R. C. Selley, L. R. M. Cocks, & I. R. Plimer (Eds.), *Encyclopedia of geology* (pp. 513–527). Elsevier. Retrieved April 28, 2024, from https://www.sciencedirect.com/science/article/pii/B0123693969004974

Rebesco, M., Camerlenghi, A., & Van Loon, A. J. (2008, January 1). Contourite research: A field in full development. In M. Rebesco & A. Camerlenghi (Eds.), *Developments in sedimentology* (pp. 1–10, Vol. 60). Elsevier. Retrieved April 28, 2024, from https://www.sciencedirect.com/science/article/pii/S0070457108100012

Rebesco, M., Hernández-Molina, F. J., Van Rooij, D., & Wåhlin, A. (2014). Contourites and associated sediments controlled by deep-water circulation processes: State-of-the-art and future considerations. *Marine Geology*, *352*, 111–154. https://doi.org/10.1016/j.margeo.2014.03.011

Rebesco, M., Liu, Y., Camerlenghi, A., Winsborrow, M., Laberg, J. S., Caburlotto, A., Diviacco, P., Accettella, D., Sauli, C., Wardell, N., & Tomini, I. (2011). Deglaciation of the western margin of the barents sea ice sheet — a swath bathymetric and sub-bottom seismic study from the kveithola trough. *Marine Geology*, *279*(1), 141–147. https://doi.org/10.1016/j.margeo.2010.10.018

Rignot, E., Mouginot, J., & Scheuchl, B. (2011). Ice flow of the antarctic ice sheet. *Science*, *333*(6048), 1427–1430. https://doi.org/10.1126/science.1208336

Rignot, E., & Kanagaratnam, P. (2006). Changes in the velocity structure of the greenland ice sheet. *Science*, *311*(5763), 986–990. https://doi.org/10.1126/science.1121381

Ruddiman, W. F., Raymo, M., & McIntyre, A. (1986). Matuyama 41,000-year cycles: North atlantic ocean and northern hemisphere ice sheets. *Earth and Planetary Science Letters*, *80*(1), 117–129. https://doi.org/10.1016/0012-821X(86)90024-5

Rudels, B. (2012). Arctic ocean circulation and variability – advection and external forcing encounter constraints and local processes. *Ocean Science*, *8*(2), 261–286. https://doi.org/10.5194/os-8-261-2012

Rudels, B. (1987). *On the mass balance of the polar ocean, with special emphasis on the fram strait*. Norsk Polarinstitutt Skrifter 188. Retrieved May 10, 2024, from https://brage.npolar.no/npolar-xmlui/handle/11250/173528

Rudels, B. (2019, January 1). Arctic ocean circulation. In J. K. Cochran, H. J. Bokuniewicz, & P. L. Yager (Eds.), *Encyclopedia of ocean sciences (third edition)* (pp. 262–277). Academic Press. Retrieved April 16, 2024, from https://www.sciencedirect.com/science/article/pii/B9780124095489112096

Rudels, B., & Carmack, E. (2022). Arctic ocean water mass structure and circulation. *Oceanography*, *35*(3), 52–65. https://doi.org/https://doi.org/10.5670/oceanog.2022.116

Sangiorgi, F., Brumsack, H.-J., Willard, D. A., Schouten, S., Stickley, C. E., O'Regan, M., Reichart, G.-J., Sinninghe Damsté, J. S., & Brinkhuis, H. (2008). A 26 million year gap in the central arctic record at the greenhouse-icehouse transition: Looking for clues. *Paleoceanography*, *23*(1). https://doi.org/10.1029/2007PA001477

Schauer, U., Loeng, H., Rudels, B., Ozhigin, V. K., & Dieck, W. (2002). Atlantic water flow through the barents and kara seas. *Deep Sea Research Part I: Oceanographic Research Papers*, *49*(12), 2281–2298. https://doi.org/10.1016/S0967-0637(02)00125-5

Schlager, U., Jokat, W., Weigelt, E., & Gebhardt, A. C. (2022). Eastern lomonosov ridge: Constraints for a variable ice mass thickness during former glaciations. *Geomorphology*, *413*, 108328. https://doi.org/10.1016/j.geomorph.2022.108328

Schock, S. G., LeBlanc, L. R., & Mayer, L. A. (1989). Chirp subbottom profiler for quantitative sediment analysis. *GEOPHYSICS*, *54*(4), 445–450. https://doi.org/10.1190/1.1442670

Shackleton, N. J., Backman, J., Zimmerman, H., Kent, D. V., Hall, M. A., Roberts, D. G., Schnitker, D., Baldauf, J. G., Desprairies, A., Homrighausen, R., Huddlestun, P., Keene, J. B., Kaltenback, A. J., Krumsiek, K. a. O., Morton, A. C., Murray, J. W., & Westberg-Smith, J. (1984). Oxygen isotope calibration of the onset of ice-rafting and history of glaciation in the north atlantic region. *Nature*, *307*(5952), 620–623. https://doi.org/10.1038/307620a0

Shackleton, N. J. (2000). The 100,000-year ice-age cycle identified and found to lag temperature, carbon dioxide, and orbital eccentricity. *Science*, *289*(5486), 1897–1902. https://doi.org/10.1126/science.289.5486.1897

Shatsky, N. S., & Muratov, M. V. (1963). Tectonic map of the arctic, scale 1:10 000 000.

Shimeld, J. W., Chian, D., Jackson, H. R., Hutchinson, D., Mosher, D. C., Wade, J. A., & Chapman, C. B. (2011). Evidence for an important tectonostratigraphic seismic marker across canada basin and southern alpha ridge of the arctic ocean [Publisher: Natural Resources Canada]. *Geological Survey of Canada, open file*, *6822*. https://doi.org/https://doi.org/10.4095/289234

Ship, S., Anderson, J., & Domack, E. (1999). Late pleistocene–holocene retreat of the west antarctic ice-sheet system in the ross sea: Part 1—geophysical results. *GSA Bulletin*, *111*(10), 1486–1516. https://doi.org/10.1130/0016-7606(1999)111<1486:LPHROT>2.3.CO;2

Smith, L. M., Miller, G. H., Otto-Bliesner, B., & Shin, S.-I. (2003). Sensitivity of the northern hemisphere climate system to extreme changes in holocene arctic sea ice. *Quaternary Science Reviews*, *22*(5), 645–658. https://doi.org/10.1016/S0277-3791(02)00166-X

Song, T., Hillaire-Marcel, C., de Vernal, A., & Liu, Y. (2024). A resilient ice cover over the southernmost mendeleev ridge during the late quaternary. *Boreas*, *53*(1), 106–123. https://doi.org/10.1111/bor.12632

Sorokin, M. Y., Zamansky, Y. Y., Langinen, A. Y., Jackson, H. R., & Macnab, R. (1999). Crustal structure of the makarov basin, arctic ocean determined by seismic refraction. *Earth and Planetary Science Letters*, *168*(1), 187–199. https://doi.org/10.1016/S0012-821X(99)00049-7

Spielhagen, R. F., Baumann, K.-H., Erlenkeuser, H., Nowaczyk, N. R., Nørgaard-Pedersen, N., Vogt, C., & Weiel, D. (2004). Arctic ocean deep-sea record of northern eurasian ice sheet history. *Quaternary Science Reviews*, *23*(11), 1455–1483. https://doi.org/10.1016/j.quascirev.2003.12.015

Spielhagen, R. F., Scholten, J. C., Bauch, H. A., & Eisenhauer, A. (2022). No freshwater-filled glacial arctic ocean. *Nature*, *602*(7895), E1–E3. https://doi.org/10.1038/s41586-021-04089-8

Steele, M., Morison, J., Ermold, W., Rigor, I., Ortmeyer, M., & Shimada, K. (2004). Circulation of summer pacific halocline water in the arctic ocean. *Journal of Geophysical Research: Oceans*, *109*. https://doi.org/10.1029/2003JC002009

Stein, R., Matthiessen, J., & Niessen, F. (2010). Re-coring at ice island t3 site of key core FL-224 (nautilus basin, amerasian arctic): Sediment characteristics and stratigraphic framework. *Polarforschung*, *79*(2), 81–96. https://doi.org/10.2312/polarforschung.79.2.81

Stein, R., Matthiessen, J., Niessen, F., Krylov, A., Nam, S., & Bazhenova, E. (2010). Towards a better (litho-) stratigraphy and reconstruction of quaternary paleoenvironment in the amerasian basin (arctic ocean). *Polarforschung*, *79*(2), 97–121. Retrieved April 28, 2024, from https://epic.awi.de/id/eprint/22435/

Stein, R., Boucsein, B., & Meyer, H. (2006). Anoxia and high primary production in the paleogene central arctic ocean: First detailed records from lomonosov ridge. *Geophysical Research Letters*, *33*(18). https://doi.org/10.1029/2006GL026776

Stephenson, R. A., Coflin, K. C., Lane, L. S., & Dietrich, J. R. (1994). Crustal structure and tectonics of the southeastern beaufort sea continental margin. *Tectonics*, *13*(2), 389–400. https://doi.org/10.1029/93TC02251

Stokes, C. R., & Clark, C. D. (2001). Palaeo-ice streams. *Quaternary Science Reviews*, *20*(13), 1437–1457. https://doi.org/10.1016/S0277-3791(01)00003-8

Stokes, C. R., & Clark, C. D. (2002a). Are long subglacial bedforms indicative of fast ice flow? *Boreas*, *31*(3), 239–249. https://doi.org/10.1111/j.1502-3885.2002.tb01070.x

Stokes, C. R., & Clark, C. D. (2002b). Ice stream shear margin moraines. *Earth Surface Processes and Landforms*, *27*(5), 547–558. https://doi.org/10.1002/esp.326

Stow, D. A. V., & Faugères, J. .-. (2008, January 1). Contourite facies and faces model. In M. Rebesco & A. Camerlenghi (Eds.), *Developments in sedimentology* (pp. 223–256, Vol. 60). Elsevier. Retrieved April 28, 2024, from https://www.sciencedirect.com/science/article/pii/S0070457108100139

Stow, D. A. V., Hunter, S., Wilkinson, D., & Hernández-Molina, F. J. (2008, January 1). The nature of contourite deposition. In M. Rebesco & A. Camerlenghi (Eds.), *Developments in sedimentology* (pp. 143–156, Vol. 60). Elsevier. Retrieved April 28, 2024, from https://www.sciencedirect.com/science/article/pii/S0070457108100097

Stow, D. A. V., & Piper, D. J. W. (1984). Deep-water fine-grained sediments: Facies models. *Geological Society, London, Special Publications*, *15*(1), 611–646. https://doi.org/10.1144/GSL.SP.1984.015.01.38

Stow, D. A. V., Faugères, J.-C., Howe, J. A., Pudsey, C. J., & Viana, A. R. (2002). Bottom currents, contourites and deep-sea sediment drifts: Current state-of-the-art. *Geological Society, London, Memoirs*, *22*(1), 7–20. https://doi.org/10.1144/GSL.MEM.2002.022.01.02

Sundvor, E., & Eldholm, O. (1979). The western and northern margin off svalbard. *Tectonophysics*, *59*(1), 239–250. https://doi.org/10.1016/0040-1951(79)90048-9

Taylor, P. T., Kovacs, L. C., Vogt, P. R., & Johnson, G. L. (1981). Detailed aeromagnetic investigation of the arctic basin: 2. *Journal of Geophysical Research: Solid Earth*, *86*, 6323–6333. https://doi.org/10.1029/JB086iB07p06323

Thiede, J., Pfirman, S., Schenke, H.-W., & Reil, W. (1990). Bathymetry of molloy deep: Fram strait between svalbard and greenland. *Marine Geophysical Researches*, *12*(3), 197–214. https://doi.org/10.1007/BF02266713

Thomson, J., Fan, Y., Stammerjohn, S., Stopa, J., Rogers, W. E., Girard-Ardhuin, F., Ardhuin, F., Shen, H., Perrie, W., Shen, H., Ackley, S., Babanin, A., Liu, Q., Guest, P., Maksym, T., Wadhams, P., Fairall, C., Persson, O., Doble, M., . . . Bidlot, J.-R. (2016). Emerging trends in the sea state of the beaufort and chukchi seas. *Ocean Modelling*, *105*, 1–12. https://doi.org/10.1016/j.ocemod.2016.02.009

Thomson, W. (1888). Polar ice-caps and their influence in changing sea levels. *Transactions of the Geological Society of Glasgow*, *8*(2), 322–340. https://doi.org/10.1144/transglas.8.2.322

Thorsnes, T., Brunstad, H., Lågstad, P., & Chand, S. (2016). Trawl marks, iceberg ploughmarks and possible whale-feeding marks, barents sea. *Geological Society, London, Memoirs*, *46*(1), 293–294. https://doi.org/10.1144/M46.101

Timmermans, M.-L., & Marshall, J. (2020). Understanding arctic ocean circulation: A review of ocean dynamics in a changing climate. *Journal of Geophysical Research: Oceans*, *125*(4), e2018JC014378. https://doi.org/10.1029/2018JC014378

van der Krogt, J. (2018). *Acoustic facies mapping of the lomonosov ridge and adjacent basins, in the arctic ocean* [Thesis for Master]. Utrecht University.

Vanneste, M., Mienert, J., & Bünz, S. (2006). The hinlopen slide: A giant, submarine slope failure on the northern svalbard margin, arctic ocean. *Earth and Planetary Science Letters*, *245*(1), 373–388. https://doi.org/10.1016/j.epsl.2006.02.045

Vogt, C., Knies, J., Spielhagen, R. F., & Stein, R. (2001). Detailed mineralogical evidence for two nearly identical glacial/deglacial cycles and atlantic water advection to the arctic ocean during the last 90,000 years. *Global and Planetary Change*, *31*(1), 23–44. https://doi.org/10.1016/S0921-8181(01)00111-4

Vogt, P. R., Taylor, P. T., Kovacs, L. C., & Johnson, G. L. (1979). Detailed aeromagnetic investigation of the arctic basin. *Journal of Geophysical Research: Solid Earth*, *84*, 1071–1089. https://doi.org/10.1029/JB084iB03p01071

Vogt, P. R. (1997). Hummock fields in the norway basin and eastern iceland plateau: Rayleigh-taylor instabilities? *Geology*, *25*(6), 531–534. https://doi.org/10.1130/0091-7613(1997)025<0531:HFITNB>2.3.CO;2

Vogt, P. R., Crane, K., & Sundvor, E. (1994). Deep pleistocene iceberg plowmarks on the yermak plateau: Sidescan and 3.5 kHz evidence for thick calving ice fronts and a possible marine ice sheet in the arctic ocean. *Geology*, *22*(5), 403–406. https://doi.org/10.1130/0091-7613(1994)022<0403:DPIPOT>2.3.CO;2

Vorren, T. O., Hald, M., Edvardsen, M., & Lind-Hansen, O.-W. (1983). Glaciogenic sediments and sedimentary environments on continental shelves: General principles with a case study from the norwegian shelf. In J. Ehlers (Ed.), *Glacial deposits in north-west europe*.

Vorren, T. O., Lebesbye, E., Andreassen, K., & Larsen, K. .-. (1989). Glacigenic sediments on a passive continental margin as exemplified by the barents sea. *Marine Geology*, *85*(2), 251–272. https://doi.org/10.1016/0025-3227(89)90156-4

Vorren, T. O., & Laberg, J. S. (1997). Trough mouth fans — palaeoclimate and ice-sheet monitors. *Quaternary Science Reviews*, *16*(8), 865–881. https://doi.org/10.1016/S0277-3791(97)00003-6

Vorren, T. O., Laberg, J. S., Blaume, F., Dowdeswell, J. A., Kenyon, N. H., Mienert, J., Rumohr, J., & Werner, F. (1998). The norwegian-greenland sea continental margins: Morphology and late quaternary sedimentary processes and environment. *Quaternary Science Reviews*, *17*(1), 273–302. https://doi.org/10.1016/S0277-3791(97)00072-3

Wahsner, M., Müller, C., Stein, R., Ivanov, G., Levitan, M., Shelekhova, E., & Tarasov, G. (1999). Clay-mineral distribution in surface sediments of the eurasian arctic ocean and continental margin as indicator for source areas and transport pathways — a synthesis. *Boreas*, *28*(1), 215–233. https://doi.org/10.1111/j.1502-3885.1999.tb00216.x

Wang, X. L., Feng, Y., Swail, V. R., & Cox, A. (2015). Historical changes in the beaufort–chukchi–bering seas surface winds and waves, 1971–2013. *Journal of Climate*, *28*(19), 7457–7469. https://doi.org/10.1175/JCLI-D-15-0190.1

Weber, J. R. (1979). The lomonosov ridge experiment: “lorex 79”. *Eos, Transactions American Geophysical Union*, *60*(42), 715–721. https://doi.org/10.1029/EO060i042p00715

Weber, J. R. (1980). Exploring the arctic seafloor. *GEOS*, *60*(42), 715–721.

Weber, J. R. (1983). Maps of the arctic basin sea floor: A history of bathymetry and its interpretation. *ARCTIC*, *36*(2), 121–142. https://doi.org/10.14430/arctic2257

Weber, J. R. (1989). Physiography and bathymetry of the arctic ocean seafloor. In Y. Herman (Ed.), *The arctic seas: Climatology, oceanography, geology, and biology* (pp. 797–828). Springer US. Retrieved February 20, 2024, from https://doi.org/10.1007/978-1-4613-0677-1_29

Weigelt, E., Jokat, W., & Franke, D. (2014). Seismostratigraphy of the siberian sector of the arctic ocean and adjacent laptev sea shelf. *Journal of Geophysical Research: Solid Earth*, *119*(7), 5275–5289. https://doi.org/10.1002/2013JB010727

Winkelmann, D., Geissler, W., Schneider, J., & Stein, R. (2008). Dynamics and timing of the hinlopen/yermak megaslide north of spitsbergen, arctic ocean. *Marine Geology*, *250*(1), 34–50. https://doi.org/10.1016/j.margeo.2007.11.013

Wolf, L. W., McCaleb, R. C., Stone, D. B., Brocher, T. M., Fujita, K., & Klemperer, S. L. (2002, May 1). Crustal structure across the bering strait, alaska: Onshore recordings of a marine seismic survey. In E. L. Miller, A. Grantz, & S. L. Klemperer (Eds.), *Tectonic evo-*

*lution of the bering shelf-chukchi sea-artic margin and adjacent landmasses* (pp. 25–37, Vol. 360). Geological Society of America. Retrieved March 6, 2024, from https://doi.org/10.1130/0-8137-2360-4.25

Woodgate, R. A., Fahrbach, E., & Rohardt, G. (1999). Structure and transports of the east greenland current at 75°n from moored current meters. *Journal of Geophysical Research: Oceans*, *104*, 18059–18072. https://doi.org/10.1029/1999JC900146

Woodgate, R. A., Weingartner, T., & Lindsay, R. (2010). The 2007 bering strait oceanic heat flux and anomalous arctic sea-ice retreat. *Geophysical Research Letters*, *37*(1). https://doi.org/10.1029/2009GL041621

Woodworth-Lynas, C. M. T., Josenhans, H. W., Barrie, J. V., Lewis, C. F. M., & Parrott, D. R. (1991). The physical processes of seabed disturbance during iceberg grounding and scouring. *Continental Shelf Research*, *11*(8), 939–961. https://doi.org/10.1016/0278-4343(91)90086-L

Yamamoto, M., & Polyak, L. (2009). Changes in terrestrial organic matter input to the mendeleev ridge, western arctic ocean, during the late quaternary. *Global and Planetary Change*, *68*(1), 30–37. https://doi.org/10.1016/j.gloplacha.2009.03.012

Yuan-Hui Li, Bischoff, J., & Mathieu, G. (1969). The migration of manganese in the arctic basin sediment. *Earth and Planetary Science Letters*, *7*(3), 265–270. https://doi.org/10.1016/0012-821X(69)90063-6

Yurco, L. N., Ortiz, J. D., Polyak, L., Darby, D. A., & Crawford, K. A. (2010). Clay mineral cycles identified by diffuse spectral reflectance in quaternary sediments from the northwind ridge: Implications for glacial–interglacial sedimentation patterns in the arctic ocean. *Polar Research*, *29*(2), 176–197. https://doi.org/10.1111/j.1751-8369.2010.00160.x

Zachos, J., Pagani, M., Sloan, L., Thomas, E., & Billups, K. (2001). Trends, rhythms, and aberrations in global climate 65 ma to present. *Science*, *292*(5517), 686–693. https://doi.org/10.1126/science.1059412

Zarkhidze, V. S., Fulton, R. J., Mudie, P. J., Piper, D. J. W., Musatov, E. E., Naryshkin, G. D., & Yashin, D. S. (1991). Circumpolar map of quaternary deposits of the arctic, map 1818a, scale 1:6 000 000. *Geological Survey of Canada*. https://doi.org/10.4095/133242

Zhao, F., Minshull, T. A., Crocker, A. J., Dowdeswell, J. A., Wu, S., & Soryal, S. M. (2017). Pleistocene iceberg dynamics on the west svalbard margin: Evidence from bathymetric and sub-bottom profiler data. *Quaternary Science Reviews*, *161*, 30–44. https://doi.org/10.1016/j.quascirev.2017.01.019

# Appendix I. Legend of the facies types idenified in sub-bottom profiles

1a
1a above 7e
1a above 8a
1a over 1a
1a over 6a
1a truncating 8a
2a
2b
3a
3b
4a
4a above 8a
4a over 3a
4a over 5a
4a truncating 8a
4b
4b above 8a
4b over 3a
4b over 5a
4b over 5a interbedded with 8a
4b over 5a over 8a
4b over 8a
4b truncating 8a
5a
5a interbedded with 7a
5a interbedded with 7e
5a interbedded with 8a
5a over 7a
5a over 7e
5a over 7e over 3a
5a over 8a
5a over 8a over 3a
5a over 8a with hyperbolae
5a over 9a
5a truncating 8a
5a truncating 8a over 3a
6a
6a over 1a
6a over 1a interbedded with 8a
6a over 1a truncating 8a
6a over 3a
6a over 7d
7a
7a interbedded with 5a
7a over 5a
7a with small anomalies
7b
7c
7d
7e
7e interbedded with 5a
7e over 1a
7e over 1a truncating 8a
7e over 3a
7e over 5a
7f
8a
8a interbedded with 5a
8a interbedded with 5a truncating 8a
8a over 1a
8a over 1a truncating 8a
8a over 3a
8a over 5a
8a truncating 8a
8a with hyperbolae
8a with hyperbolae interbedded with 5a
8a with small anomalies
8b
9a
9a interbedded with 5a

# Appendix II. Depressions in eastern Greenland-spitsbergen Sill

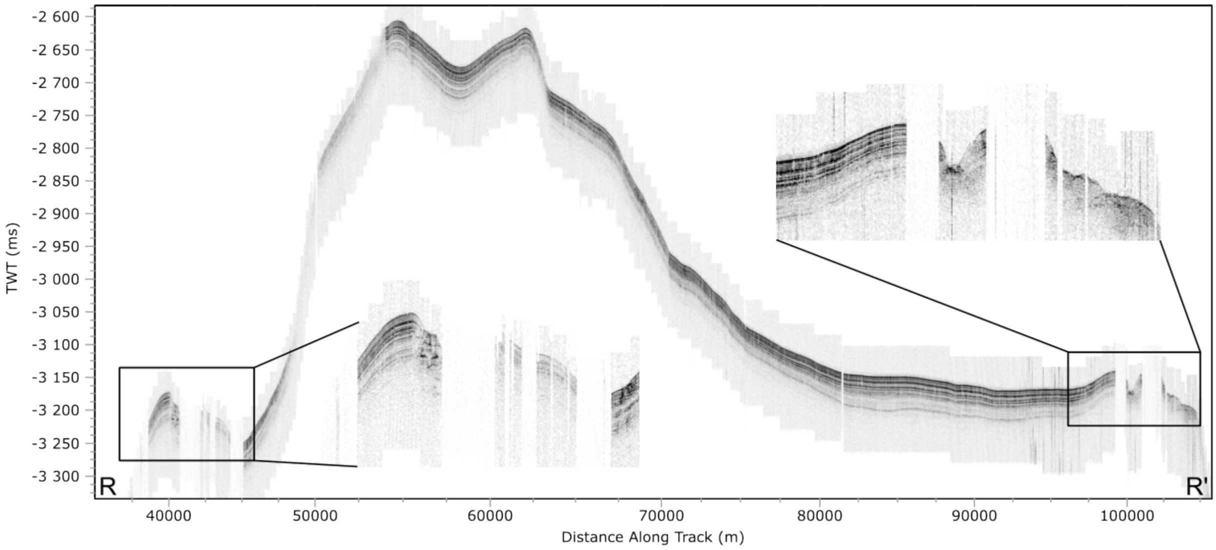


***Location of the profile between R and R' shown in Fig. 17 of the main thesis**